Theoretical and Experimental Analysis and Optimization of Thermal Conduction in Electrochemical and Latent Heat Energy Storage Systems

by

Amirhossein Mostafavi

DISSERTATION

Submitted in partial fulfillment of the requirements

For the degree of Doctor of Philosophy at

The University of Texas at Arlington

August 2021

Arlington, Texas

Supervising Committee:

    Dr. Ankur Jain (Committee Chairperson)

    Dr. Miguel Amaya

    Dr. Hyejin Moon

    Dr. Amir Ameri

    Dr. Sunand Santhanagopalan

This dissertation is dedicated to

my loving parents, lovely sister, and dear brother

for their endless support through all the stages of my life

ACKNOWLEDGEMENTS

I would like to express my deepest appreciation to my advisor, Dr. Ankur Jain for giving me the opportunity to continue my research in his research group. I extend my gratitude for his invaluable support and guidance during my PhD study. This dissertation would have not been possible without his advice and mentorship.

I would like to thank my committee members for all their guidance and instructions. Their constructive suggestions helped me to improve the quality of my dissertation.

I would like to thank my friends, lab mates and colleagues at Microscale Thermophysics Laboratory (MTL) who helped me along this journey.

My gratitude extends to MAE department at the University of Texas at Arlington for all their support.

August 2021

ABSTRACT

Theoretical and Experimental Analysis and Optimization of Thermal Conduction in

Electrochemical and Latent Heat Energy Storage Systems

Amirhossein Mostafavi, Ph.D.

The University of Texas at Arlington, 2021

Supervising Professor: Dr. Ankur Jain

Phase change materials (PCMs) are used commonly for energy storage purposes. Thermal energy can be stored in a PCM with a variety of configurations such as PCM slabs, cartesian and cylindrical finned systems. Heat transfer in PCM storage systems can be from a heat transfer fluid (HTF) or a heat source at constant temperature to adjacent PCM. The rate of heat transfer is limited by thermal properties. Fin insertion can improve the heat transfer inside the PCM. Chapters 2 and 3 derive and solve the governing energy equations to determine the transient temperature distribution in the PCM due to the presence of a fin in both Cartesian and cylindrical finned PCM systems. Results show existence of an optimal fin size which maximizes heat stored in the system.

In addition, the analytical method is extended to determine heat transfer and melting front propagation in PCM slab systems due to convective heat transfer of flow past the slabs, which is a nonlinear and transient problem. It is important to treat the PCM-fluid flow heat transfer problem as a conjugate problem with convective heat transfer in the fluid and phase change heat transfer in the PCM. Heat transfer coefficient at the PCM-flow interface is a function of space and time where the heat transfer from a plate to flow past over a plate is due to either heat flux or temperature on the plate. Chapters 4 and 5 present an approach based on integral method to determine convective

heat transfer from a plate into a fluid flow, where the boundary condition of heat flux or temperature on the plate is a known general function of time and space.

Chapter 6 solves the conjugate problem of PCM-flow problem by implementing an iterative approach to determine transient convective heat transfer and temperature distribution on the fluid-PCM interface. The integral method showed in chapter 5 is used to solve the flow sub-problem. An approximate solution based on perturbation method solves the PCM sub-problem. An iterative approach integrates and solves these two subproblems. The effect of thermal properties of heat transfer fluid and PCM is investigated. This study improves the fundamental understanding of heat transfer in PCM storage systems and provides practical guidelines for design of such systems.

Electrochemical energy storage in Li-ion cells is another key technology in energy storage purposes with multiple applications such as electric vehicles and consumer electronics. Li-ion cells are very sensitive to temperature. Chapter 7 investigates dual-purpose thermal management of a Li-ion cell using solid-state thermoelectric elements. Both cooling and heating of a Li-ion cell are demonstrated, with good agreement between experimental data and numerical simulation results which makes thermoelectric coolers an effective approach for thermal management of Li-ion cells at aggressive operating conditions.

It is expected that the theoretical and experimental works presented in this dissertation will help in understanding heat transfer, design optimization and improving the performance of phase change energy and electrochemical storage systems.

Table of Contents

VIII

Chapter 1

1-1. Introduction

A number of technologies have been used for energy storage in harvesting renewable energies [1]. The intermittent nature of renewable energies can be addressed by energy storage technologies. Energy storage technologies not only improve the reliability of renewable energies, but also decrease the mismatch between supply and demand [2]. The capability of utilizing excess energy and releasing that energy later critical for addressing the transient nature of renewable energy. Thermal energy storage in phase change material and electrochemical energy storage in Li-ion cells are two common technologies which have been investigated for this purpose [3].

Theoretical modeling and understanding of heat transfer in energy storage systems is critical to enhance the performance, efficiency and safety of such systems. Latent heat energy storage in phase change material and electrochemical energy storage in Li-ion cells are two commonly used techniques in energy storage technologies. A concise introduction to each of thermal energy storage and electrochemical energy storage in phase change materials (PCM) and Li-ion cells respectively is presented next and a comprehensive introduction is presented in the beginning of each chapter.

1-1-1. Thermal energy storage in phase change materials

Among the various available technologies for energy storage, phase change based energy storage offers several key advantages. In this technology, heat is transferred from a hot source into the solid working material, resulting in phase change to a liquid. Due to the significantly large latent heat compared to specific heat capacity, phase change offers much greater energy storage

capability compared to sensible heat based technologies [4]. Flat plate PCM bed [5] and finned-PCM [6] storage system are two common configurations of latent heat energy storage systems.

Some key challenges in phase change energy storage include the low thermal conductivity of typical phase change materials (PCMs) that inhibit heat transfer into the working material [7], which lowers the rate of energy storage. Most PCMs have rather low thermal conductivity [8], and significant work has been reported on improving thermal conductivity of these materials. In addition to such material improvements, work has also been reported on geometrical changes to increase the rate of heat transfer into the PCM . Specifically, the insertion of fins into PCMs has been investigated by several papers [9,10]. Similar to the use of fins for enhancing rate of heat transfer between a solid base and a fluid, this may result in enhanced heat transfer due to the increased surface area due to the fin.

In flat plate PCM systems, a heat transfer fluid (HTF) flow between two adjacent PCM slabs. These systems have simple construction and high ratio of surface area to volume. The challenge in thermal analysis of PCM slab systems is transient nature of heat transfer process within a PCM and fluid flow with a moving melting front [11].

1-1-2. Electrochemical energy storage

Electrochemical energy storage in Li-ion cells offers multiple advantages, such as high energy density, high discharge rate, etc. Li-ion cells have applications in electric vehicles and consumer electronics [12,13]. Li-ion cells are sensitive to temperature. Thermal runaway and poor performance are outcomes of operating at relatively elevated and low temperatures respectively. Heat generated in a Li-ion cell during charge or discharge processes leads to significant temperature rise. If the temperature exceeds a certain limit, a series of cascading exothermic reactions occur that result in ever-increasing cell temperature, eventually leading to fire and

explosion. Manufacturers often specify a maximum allowable temperature in the range of 60-70°C to avoid thermal runaway and safety issues [14]. On the other hand, Operation of Li-ion cells at low temperature is not also desirable, as it leads to poor performance and lifetime [15]. This is a particularly important for Li-ion cells in an electric vehicle operating in cold climates. Consequently, a dual-purpose thermal management system is particularly important for the safety and performance of Li-ion cells.

A number of different thermal management strategies have been investigated separately for Li-ion cell cooling and heating including air and liquid cooling, heat pipes, phase change cooling and thermoelectric cooling. Air cooling is typically simple but may not be effective in aggressive conditions. Compared to air cooling, liquid cooling systems remove more heat, but are more complicated. Phase change and heat pipe-based cooling systems are passive in nature [16-19]. Heating up a cell with joule heating has been also proposed [20]. Most thermal management strategies investigated in literature, do not simultaneously address both cooling and heating requirements of a Li-ion cell.

Chapters two and three present an analytical solution for temperature distribution in a PCM with presence of fin in Cartesian and cylindrical systems respectively. In comparison to the extensive literature on experimental investigation of fin based enhancement in phase change materials, relatively lesser work has been reported on theoretical heat transfer modeling of this problem. A comprehensive analytical heat transfer model that completely accounts for sensible and phase change energy in fin based systems is presented. The governing energy equation for heat transfer from a hot wall into a PCM in the presence of fin extending into the PCM is derived. The expression for total heat absorbed by the PCM shows existence of an optimum fin size

resulting in highest total heat stored in the PCM. Dependence of the optimum fin size on thermal conductivity of fin is also addressed.

Convective heat transfer between a flat plate and fluid flow is discussed in chapters four and five. With respect to extensive literature on external convective heat transfer, two particular problems that have not been discussed much in the literature is that of a flat plate with plate boundary condition of heat flux or temperature varying in both space and in time. A solution of the problem of general heat flux or temperature on the plate is desirable for many practical applications such as the problem of fluid flow over a bed of phase change material.

Chapters six investigates convective heat transfer due to fluid flow over one or more flat PCM beds. Despite its simplicity, heat transfer modeling of this geometry is not straight-forward. On PCM side, the phase change process occurring in the PCM bed is non-linear in nature. On the other side, fluid flow and convective heat transfer over the bed is also non-linear. In general, the convective heat transfer between the bed and fluid is a function of both space and time. The convective heat transfer model developed in chapter five is used to handle the PCM-fluid heat transfer problem as a conjugate problem, with heat transfer at the PCM flow interface.

Chapter seven shows experimental and numerical analysis of dual-purpose thermal management of a Li-ion cell using thermoelectric elements. Effective cooling of the cell at aggressive discharge rates, as well as quick heating of the cell in a low temperature ambient, are demonstrated by simply reversing the polarity of thermoelectric current. Experimental data are found to be in very good agreement with numerical simulations. The results indicates the capability of thermoelectric elements to address two critical thermal management challenges in Li-ion cells simultaneously.

1.1 References

[1] Aneke, M., & Wang, M. Energy storage technologies and real life applications–A state of the art review. Applied Energy, (2016) 179, 350-377.

[2] Kumaresan V, et al. Role of PCM based nanofluids for energy efficient cool thermal storage system. Int J Refrig (2013) ;36(6):1641–7.

[3] Díaz-González, F., et al. A review of energy storage technologies for wind power applications. Renewable and sustainable energy reviews, (2012) 16(4), 2154-2171.

[4] Sharma, V. Tyagi, C. Chen, D. Buddhi, Review on thermal energy storage with phase change materials and applications, Renewable and Sustainable Energy Reviews. 13 (2009) 318–345.

[5] X.Q. Suna, Y.H. Chua, M.A. Medina, et al., Experimental investigations on the thermal behavior of phase change material (PCM) in ventilated slabs, Appl. Therm. Eng. 148 (2019) 1359–1369.

[6] A.H. Mosaffa, F. Talati, H. Basirat Tabrizi, M.A. Rosen, Analytical modeling of PCM solidification in a shell and tube finned thermal storage for air conditioning systems, Energy Build. 49 (2012) 356–361.

[7] Lin, Y., Jia, Y., Alva, G., & Fang, G. Review on thermal conductivity enhancement, thermal properties and applications of phase change materials in thermal energy storage. Renewable and sustainable energy reviews, 82 (2018), 2730-2742.

[8] Singh, R., Sadeghi, S., & Shabani, B. (2019). Thermal conductivity enhancement of phase change materials for low-temperature thermal energy storage applications. Energies, 12(1) (2019), 75.

[9] Suraparaju, S. K., & Natarajan, S. K., Experimental investigation of single-basin solar still using solid staggered fins inserted in paraffin wax PCM bed for enhancing productivity. Environmental Science and Pollution Research, 28(16) (2021)., 20330-20343.

[10] Ping, P., Peng, R., Kong, D., Chen, G., & Wen, J. (2018). Investigation on thermal management performance of PCM-fin structure for Li-ion battery module in high-temperature environment. Energy conversion and management, 176, 131-146.

[11] Ding, C., Niu, Z., Li, B., Hong, D., Zhang, Z., & Yu, M. (2020). Analytical modeling and thermal performance analysis of a flat plate latent heat storage unit. Applied Thermal Engineering, 179 (2020), 115722.

[12] Shah, K., Balsara, N., Banerjee, S., Chintapalli, M., Cocco, A. P., Chiu, W. K. S., & Jain, A. (2017). State of the art and future research needs for multiscale analysis of Li-ion cells. Journal of Electrochemical Energy Conversion and Storage, 14(2) (2017).

[13] Scrosati, B., & Garche, J. Lithium batteries: Status, prospects and future. Journal of power sources, 195(9) (2010), 2419-2430.

[14] Shah, K., & Jain, A. (2019). Prediction of thermal runaway and thermal management requirements in cylindrical Li-ion cells in realistic scenarios. International Journal of Energy Research, 43(5), 1827-1838.

[15] Zhang, S. S., K. Xu, and T. R. Jow. "The low temperature performance of Li-ion batteries." *Journal of Power Sources* 115.1 (2003): 137-140.

[16] Chen, Dafen, et al. "Comparison of different cooling methods for lithium ion battery cells." *Applied Thermal Engineering* 94 (2016): 846-854.

[17] Anthony, Dean, et al. "Improved thermal performance of a Li-ion cell through heat pipe insertion." *Journal of The Electrochemical Society* 164.6 (2017): A961.

[18] Parhizi, M., & Jain, A. (2019). Analytical modeling and optimization of phase change thermal management of a Li-ion battery pack. *Applied Thermal Engineering*, *148*, 229-237.

[19] Siddique, Abu Raihan Mohammad, Shohel Mahmud, and Bill Van Heyst. "A comprehensive review on a passive (phase change materials) and an active (thermoelectric cooler) battery thermal management system and their limitations." *Journal of Power Sources* 401 (2018): 224-237.

[20] Yang, Xiao-Guang, Teng Liu, and Chao-Yang Wang. "Innovative heating of large-size automotive Li-ion cells." *Journal of power sources* 342 (2017): 598-604.

Chapter 2

Theoretical modeling and optimization of fin-based enhancement of heat transfer into a phase change material

2-1. Introduction

Phase change based energy storage plays a key role in several engineering applications [1–3]. Due to the significantly large latent heat compared to specific heat capacity, phase change offers much greater energy storage capability compared to sensible heat based technologies [4]. A key challenge in phase change energy storage, however, is that thermal impedance offered by the melted phase results in a reduction in the rate of heat transfer to the phase change propagation front.

Due to this self-limiting nature of the phase change propagation process, several approaches for enhancement in phase change based energy storage have been investigated, including the insertion of fins into the PCM [5–7]. Fins offer potential improvement in rate of energy stored by enhancing available surface area for heat transfer into the PCM. A key goal of research in this field has been to optimize fin shape and size for enhanced rate of energy storage. Towards this, both experimental and theoretical/numerical research has been reported.

On the experiments side, two-dimensional melting in a PCM with convection in the liquid has been experimentally investigated in both vertical and horizontal configurations of a finned tube storage unit [8,9]. Melt fraction has been shown to be a function of both Stefan and Fourier numbers, with conduction being the dominant heat transfer mode at the beginning of melting [8,10]. Presence of a fin has been shown to result in improved performance of a PCM-based heat sink [11]. Melting fraction and fin effectiveness have been experimentally correlated for horizontal fins in a rectangular enclosure [12]. Dimensionless correlations for fin effectiveness in melting and solidification processes have been developed [13]. The impact of geometry on the importance of convective effects has been investigated [14]. Comparison of experimental data and numerical

model prediction for different configurations of a photovoltaic-PCM system with internal fins has been presented [15].

Significant research on theoretical and numerical modeling of fin-based heat transfer into a PCM is also available. The PCM melting process within vertical fins attached to a horizontal constant temperature plate has been studied numerically to study the effect of fin geometrical parameters on the melting process. Dimensional analysis has been carried out to generalize the results for determining melt fraction [7]. Semi-analytical and numerical modelings of melting and solidification processes in the presence of a fin have been presented [16-18]. The fraction of solidified PCM and fin temperature distribution in a PCM heat sink with plate fins has been calculated using a simplified analytical model for constant heat flux boundary condition [19]. Numerical methods have been used to optimize fin geometry for maximizing phase change based heat sink performance [20], to determine the critical size of a composite heat sink [21] and to minimize the length of a finned storage system to meet the criteria for the critical operation time in electronic devices [22]. Experimental and numerical investigation of a PCM based heat sink with straight fins has been presented [23]. This work showed that fin geometry affects heat sink performance, and an optimal fin thickness results in maximum rate of heat removal [23]. Numerical optimization of the number and size of fins with constant heat flux boundary condition has also been presented [24]. Solidification time has been approximated using an approximate analytical method for two different finned storage systems [25]. An analytical solution has been compared with a numerical method to estimate the solid-liquid inter-face in a finned PCM storage system [19].

Figure 1 shows a schematic of a simplified Cartesian phase change based energy storage, wherein the PCM absorbs heat from two hot walls maintained at a constant temperature. A fin

protruding between the walls into the PCM results in enhanced available surface area for heat transfer into the fin. Note that if infinite time is available for heat transfer from the wall into the PCM, then the entire PCM will melt and reach the wall temperature. In such a case, the total amount of energy that can be stored is known in advance, and the presence of the fin is actually counterproductive, since it reduces PCM volume. However, in many practical applications, only a finite amount of time is available for effecting the heat transfer process, in which case, the presence of the fin may be beneficial, depending on the balance between two key heat transfer effects. On one hand, the presence of a fin reduces PCM volume available and the area of direct contact between the PCM and the hot wall. In Figure 1, for example, the fin of width 2w results in only the remainder 2(W-w) width of the hot wall being available for direct heat transfer into the PCM. This results in reduced heat transfer from the wall to the PCM. On the other hand, however, thermal conduction occurs from the hot wall into the fin, followed by heat transfer from the fin surface into the PCM. This is a transient process, because of the time involved in thermal diffusion into the fin. Initially, the fin temperature is not very high, due to which, it does not enhance heat transfer into the PCM. As time passes and the fin heats up, it increasingly contributes towards heat transfer into the PCM. Due to these two directly conflicting effects of the fin and the transient nature of this problem, it is possible that for a given, finite time available, an optimal fin size may exist that results in enhanced energy storage despite the reduced PCM volume due to inclusion of the fin. A theoretical heat transfer model for this problem is very desirable for studying such transient effects. Some work in this direction has been reported by Lamberg and Sirén, who presented semi-analytical and numerical solutions for melting and solidification processes in the presence of a fin [16–18]. Through simplifying assumptions of quasi-steady conditions and no sensible heat storage, governing equations for the fin temperature and phase change front location were derived. An

10

expression for the fin temperature was obtained by assuming the phase change front location to be constant. While this approach resulted in a solution for the fin temperature, some of these assumptions may not be accurate, and it may be helpful to account for effects neglected in these papers. Further, these papers do not address the conflicting effects of the fin on energy absorbed in the PCM as outlined above, and the consequent optimization problem of maximizing heat transfer into the PCM for a given total time as a function of fin size and thermal properties. A comprehensive theoretical heat transfer model is needed to optimize the use of fins for enhancing heat transfer in PCMs and exploring optimal fin size.
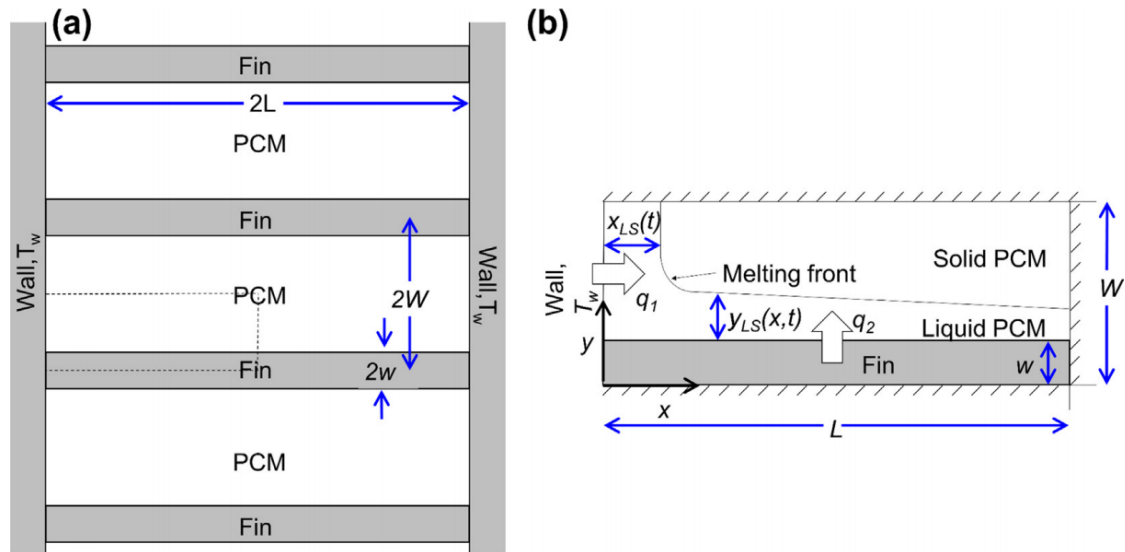
Figure 1. (a) Schematic of a Cartesian phase change energy storage problem with periodic fins for enhancing energy storage in the PCM; (b) Schematic of the unit cell in this heat transfer problem.

This paper derives the governing energy equation for heat transfer from a hot wall into a PCM in the presence of fins extending into the PCM. The equation accounts for transient thermal diffusion into the fin and the resulting transient heat transfer into the PCM. Both latent and sensible heat storage in the fin are accounted for. Based on a semi-analytical solution of the equation, an expression for the total heat absorbed by the PCM for a given total time is derived. This is used to

examine the dependence of total heat absorbed on the fin size, showing that, for a given total time, the total heat absorbed is highest at a specific fin size. This optimal fin size is itself shown to be a function of fin thermal conductivity, as well as the total time available. These results provide useful insights into the nature of enhanced heat absorption into a PCM due to a fin, and help in optimizing the fin design in order to maximize heat absorption into the PCM.

2-2. Theoretical model

Consider a wall maintained at a constant temperature T_w, from which, thermal energy is absorbed by a surrounding PCM. In order to enhance heat transfer into the PCM, fins of width $2w$ and length $2L$ are provided periodically with a fin-to-fin pitch of $2W$, as shown in Figure 1(a). Thermal conductivity of fin and PCM are k_f and k_p respectively. Similar nomenclature is followed for the volumetric specific heat c. The latent heat of phase change of the PCM is taken to be L_p. All properties are assumed to be independent of temperature. The PCM and fin are both assumed to be initially at the PCM melting temperature T_m. Note that if infinite time is available for heat transfer, then the entire PCM will eventually reach the wall temperature, so that the total heat absorbed is proportional to PCM mass, and therefore, the presence of the fin may actually reduce the amount of energy storage by reducing PCM available within the fixed total volume. However, in several applications, only a finite time is available for energy storage, in which case, transient heat transfer in the fin may enhance the total energy absorbed within the finite available time. Even accounting for the reduced PCM mass, this may result in overall increase in energy absorbed, compared to the case without fin.

The interest here is in determining the transient temperature distributions $T_f(x,t)$ and $T_p(x,y,t)$ in the fin and PCM respectively, and therefore, in determining the total amount of heat absorbed

by the PCM, $q_{total}(t)$ for a given finite total time. The fin provides additional surface for the PCM to absorb heat from. However, presence of the fin also reduces the area of direct contact between the PCM and the hot wall, which is the primary energy source in this problem. Accounting for these competing factors is, therefore, critical for accurate determination of $q_{total}(t)$.

The analysis of this problem can be simplified by considering a symmetry unit cell that repeats itself in the geometry, as marked in Figure 1(a) and shown in detail in Figure 1(b). The total heat absorbed by the PCM up to time t, $q_{total}(t)$, comprises two distinct components - $q_1(t)$, the heat absorbed by the PCM directly from the width (W-w) of the wall, and $q_2(t)$, the heat absorbed by the PCM from the length L of the fin, as shown in Figure 1(b). Thermal diffusion from the wall into the fin slowly raises the fin temperature, which in turn increases the heat absorbed by the PCM. Thus, $q_2(t)$ is expected to be small initially and slowly rise with time. In general, $q_2(t)$ will depend on the properties of both fin and PCM as well as geometrical parameters such as fin size w. On the other hand, $q_1(t)$ depends only on the properties of the PCM and the temperature difference (T_w-T_m). The region close to the origin of the coordinate axis shown in Figure 1(a) experiences heat absorption from both directions. Neglecting this small region, two separate, independent melting fronts can be assumed for ease of analysis in the rest of the PCM. The melting fronts originating from the wall and fin propagate in the x and y directions, respectively, and are responsible for $q_1(t)$ and $q_2(t)$, respectively. Such an assumption of two independent melting fronts is commonly made to simplify two-dimensional phase change problems [16-18], and is reasonable when the aspect ratio of the unit cell is much larger than one. Further, natural convection in the liquid phase is neglected here, which may be a reasonable assumption for a wide, horizontal PCM layer [7].

Separate expressions for $q_1(t)$ and $q_2(t)$ are now derived. For generality, the results are derived in nondimensional form. The nondimensionalization scheme is described in the Nomenclature section. Nondimensional temperature is denoted as θ, whereas several other nondimensional quantities are denoted with an overbar.

2-2-1. Wall-to-PCM heat transfer

Until the time that the phase change front originating from the wall reaches the other end of the domain, the PCM may be considered to be semi-infinite. Under this assumption, the problem of heat transfer from the wall directly into the PCM is the classical Stefan problem with T_w as the constant temperature boundary condition. Therefore, the location of the phase change front and temperature distribution in the melted PCM are given by [26]

$$\bar{x}_{LS}(\bar{t}) = 2\lambda\sqrt{\bar{t}} \tag{1}$$

$$\theta_P(\bar{x}, \bar{t}) = 1 - \frac{\text{erf}\left(\dfrac{\bar{x}}{2\sqrt{\bar{t}}}\right)}{\text{erf}(\lambda)} \tag{2}$$

where λ is the root of:

$$\lambda\,\text{erf}(\lambda)e^{\lambda^2} = \frac{Ste}{\sqrt{\pi}} \tag{3}$$

Consequently, the total heat absorbed by the PCM directly from the wall, $\bar{q}_1(\bar{t})$ per unit depth of the wall in the normal direction is given by

$$\bar{q}_1(\bar{t}) = 2(1 - \frac{w}{W})\frac{\sqrt{\bar{t}}}{\sqrt{\pi}\,\text{erf}(\lambda)} \tag{4}$$

Note that equation (4) accounts for the reduced area of contact between the PCM and the wall due to presence of the fin. Therefore, the larger the fin size w/W, the lower is the value of $\bar{q}_1(\bar{t})$.

14

2-2-2. Wall-to-fin-to-PCM heat transfer

The problem of determining $\bar{q}_2(\bar{t})$, the total heat absorbed by the PCM from the fin is considerably more complicated due to the coupling between thermal conduction into the fin and heat transfer from fin into the PCM. This necessitates determining the fin temperature distribution $\theta_f(\bar{x}, \bar{t})$ first, followed by the PCM temperature distribution $\theta_p(\bar{x}, \bar{y}, \bar{t})$, and then $\bar{q}_2(\bar{t})$.

Temperature within the fin is assumed to vary spatially only in the x direction, and not in the y direction. This assumption of one-dimensional heat transfer in the fin is reasonable as long as the fin width is small compared to fin length. In order to determine the fin temperature distribution, the governing energy conservation equation in the fin is derived. To do so, energy balance of an infinitesimal fin element of length dx is considered, as shown in Figure 2. Similar to the classical energy analysis of a fin in a fluid without phase change [27], the components of energy balance to be considered include thermal conduction into and out of the element, increase in thermal energy stored in the element and heat loss from the element into the PCM. As shown in Figure 2, a balance between these terms, along with Fourier's law can be used to derive the following governing equation for the fin temperature

$$\frac{\bar{c}_f}{\bar{k}_f} \frac{\partial \theta_f}{\partial \bar{t}} = \frac{\partial^2 \theta_f}{\partial \bar{x}^2} - \bar{S} \tag{5}$$

where $\bar{S}$ is the heat generation term due to heat transfer to the PCM. The final step is to express $\bar{S}$ in the form of the fin temperature, in order to write equation (5) as a differential equation in θ_f. In traditional fin analysis in a fluid without phase change [27], this can be done simply using the convective heat transfer coefficient. In the present analysis, however, this term is much more challenging to write in terms of θ_f due to phase change occurring in the PCM. Unlike the wall-to-PCM $\bar{q}_1(\bar{t})$ problem, in this case, temperature of the fin element changes over time, and therefore,

this is a time-dependent boundary condition problem, unlike the wall-to-PCM problem which can be easily modeled as a classical Stefan problem with constant temperature boundary condition. In order to determine the PCM temperature distribution, and therefore heat flux into the PCM due to the time-varying fin temperature that acts as the base temperature for this phase change problem, this must be treated as a one-dimensional melting problem with time-dependent temperature boundary condition given by the fin temperature. A solution for this problem using perturbation method is available [28,29]. In this method, the temperature distribution in the PCM is written in a power series form, using the Stefan number, and the independent variable is transformed from $\bar{t}$ to $\bar{y}$, the phase change front location. Finally, utilizing the energy conservation equation at the phase change interface, the carrying out a term-by-term comparison for various powers of *Ste*, an expression for the temperature distribution can be derived. The final result is [28,29]

$$\theta_p(\bar{x}, \bar{y}, \bar{t}) = \theta_0(\bar{x}, \bar{y}, \bar{t}) + Ste\,\theta_1(\bar{x}, \bar{y}, \bar{t}) + Ste^2\theta_2(\bar{x}, \bar{y}, \bar{t}) \tag{6}$$

where the components θ_0, θ_1 and θ_2 may be expressed in terms of the corresponding fin temperature at the location x as follows

$$\theta_0(\bar{x}, \bar{y}, \bar{t}) = \theta_f\left(1 - \frac{\bar{y}}{\bar{y}_{LS}}\right) \tag{7}$$

$$\theta_1(\bar{x}, \bar{y}, \bar{t}) = \frac{1}{6}\theta_f\left(\frac{\bar{y}}{\bar{y}_{LS}}\right)\left(\frac{\bar{y}}{\bar{y}_{LS}} - 1\right)\left[\theta_f\left(\frac{\bar{y}}{\bar{y}_{LS}} + 1\right) - \frac{\theta_f{}'}{\bar{y}_{LS}'}\bar{y}_{LS}\left(\frac{\bar{y}}{\bar{y}_{LS}} - 2\right)\right] \tag{8}$$

$$\theta_2(\bar{x}, \bar{y}, \bar{t}) = -\frac{1}{360}\theta_f\left(\frac{\bar{y}}{\bar{y}_{LS}}\right)\left(\frac{\bar{y}}{\bar{y}_{LS}} - 1\right)\left[\theta_f{}^2\left(\frac{\bar{y}}{\bar{y}_{LS}} + 1\right)\left(9\left(\frac{\bar{y}}{\bar{y}_{LS}}\right)^2 + 19\right)\right.$$

$$\left. + 10\left(\frac{\theta_f{}'}{\bar{y}_{LS}'}\right)^2\bar{y}_{LS}^2\left(\frac{\bar{y}}{\bar{y}_{LS}} + 4\right) + 5\theta_f\frac{\theta_f{}'}{\bar{y}_{LS}'}\bar{y}_{LS}\left(3\left(\frac{\bar{y}}{\bar{y}_{LS}}\right)^2 + 5\left(\frac{\bar{y}}{\bar{y}_{LS}}\right)\right.\right. \tag{9}$$

$$\left.\left. + 17\right)\right]$$

where θ_f is the fin temperature distribution. As a result, an expression for $\bar{S}$ can be written as

$$\bar{S} = \frac{1}{\bar{k}_f \frac{w}{W}} \left[\frac{\theta_f}{\bar{y}_{LS}} + Ste \frac{\theta_f \left(\theta_f + 2\frac{\theta_f{}'}{\bar{y}_{LS}'} \bar{y}_{LS} \right)}{6\bar{y}_{LS}} - (Ste)^2 \frac{\theta_f \left(40 \left(\frac{\theta_f{}'}{\bar{y}_{LS}'} \right)^2 \bar{y}_{LS}^2 + 85\theta_f \frac{\theta_f{}'}{\bar{y}_{LS}'} \bar{y}_{LS} + 19\theta_f{}^2 \right)}{360\bar{y}_{LS}} \right] \tag{10}$$

where the location of the melting front originating from the fin, $\bar{y}_{LS}$ is given by [28,29]

$$\bar{y}_{LS}(\bar{x}, \bar{t}) = \left[2Ste \int_0^{\bar{t}} \theta_f(\bar{x}, \bar{\tau}) \left(1 - \frac{Ste}{3} \theta_f(\bar{x}, \bar{\tau}) \right. \right.$$

$$\left. \left. + \frac{7}{45} Ste^2 \theta_f(\bar{x}, \bar{\tau})^2 \right) d\bar{\tau} \right]^{\frac{1}{2}} \tag{11}$$

Note the primes in equations (8)-(10) refer to time derivatives.
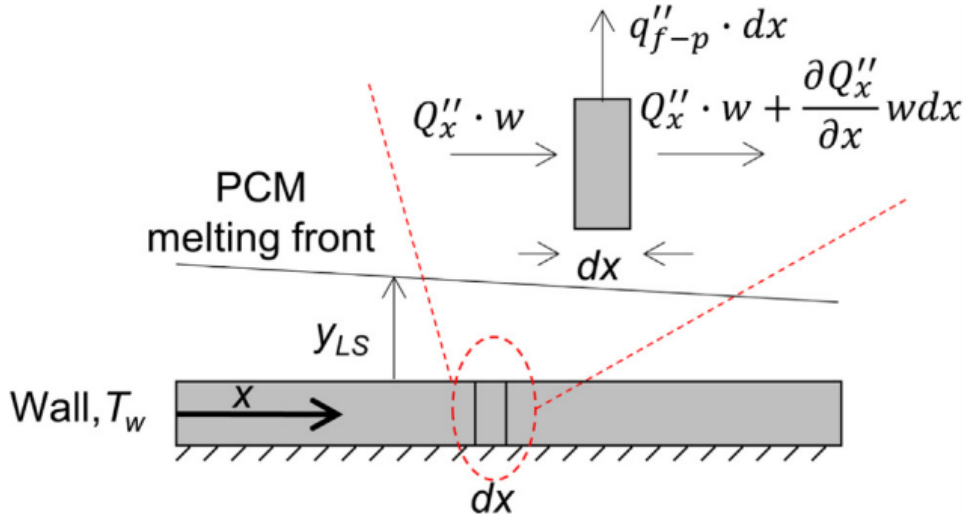
Figure 2. Schematic of an infinitesimal fin element of width dx for deriving a governing energy conservation equation for the fin temperature distribution.

Note that the perturbation method solution utilized above is valid only for small values of *Ste*, which is usually the case for most practical phase change processes [28,29], and only until the phase change front reaches the other boundary.

Equations (10)-(11) express heat loss from a fin location at any given time in terms of the prior fin temperature history at that location and thermal properties of the PCM.

By combining equations (5) and (10), a complicated partial differential equation for the fin temperature distribution can be derived to be

$$\frac{\bar{c}_f}{\bar{k}_f}\frac{\partial \theta_f}{\partial \bar{t}} = \frac{\partial^2 \theta_f}{\partial \bar{x}^2} - \frac{1}{\bar{k}_f \frac{w}{W}}\left[\frac{\theta_f}{\bar{y}_{LS}} + Ste\frac{\theta_f\left(\theta_f + 2\frac{\theta_f'}{\bar{y}_{LS}'}\bar{y}_{LS}\right)}{6\bar{y}_{LS}} - (Ste)^2\frac{\theta_f\left(40\left(\frac{\theta_f'}{\bar{y}_{LS}'}\right)^2\bar{y}_{LS}^2 + 85\theta_f\frac{\theta_f'}{\bar{y}_{LS}'}\bar{y}_{LS} + 19\theta_f^2\right)}{360\bar{y}_{LS}} \right] \tag{12}$$

Note that the negative heat generation term in equation (12) involves the phase change front $\bar{y}_{LS}$, which itself is given by an integral of the fin temperature distribution over time (equation (11)). This makes equation (12) considerably complicated to solve explicitly.

Boundary conditions and initial conditions must be specified in order to complete the fin temperature problem. While at $\bar{x}$=0, the fin temperature must equal the wall temperature, an adiabatic boundary condition applies at $\bar{x}=\bar{L}$ as a result of symmetry in the problem. Finally, the initial fin temperature is equal to the PCM melting temperature. These are given mathematically by the following:

$$\theta_f(0, \bar{t}) = 1 \tag{13}$$

$$\left(\frac{\partial \theta_f}{\partial \bar{x}}\right)_{\bar{x}=\bar{L}} = 0 \tag{14}$$

18

$$\theta_f(\bar{x}, 0) = 0 \tag{15}$$

Equation (12) captures the effect of the PCM in the form of a negative heat generation term, similar to classical fin analysis without phase change [27]. This term involves an integral of the temperature distribution over time, which while more complicated than past work [16-18] is more accurate, as it correctly accounts for the propagation of the phase change front over time.

Once a solution for equation (12) is determined, the PCM temperature distribution can be obtained from equation (6). Heat transfer in the x direction within the PCM is neglected, which is reasonable in the absence of flow within the PCM. Finally, an expression for $\bar{q}_2(\bar{t})$, the total heat flux into the PCM at the fin base can be derived using equation (10) as

$$\bar{q}_2(\bar{t}) = \int_0^{\bar{t}} \int_0^{\bar{L}} \left[\frac{\theta_f}{\bar{y}_{LS}} + Ste \frac{\theta_f\left(\theta_f + 2\frac{\theta_f'}{\bar{y}_{LS}'}\bar{y}_{LS}\right)}{6\bar{y}_{LS}} - (Ste)^2 \frac{\theta_f\left(40\left(\frac{\theta_f'}{\bar{y}_{LS}'}\right)^2 \bar{y}_{LS}^2 + 85\theta_f\frac{\theta_f'}{\bar{y}_{LS}'}\bar{y}_{LS} + 19\theta_f^{\,2}\right)}{360\bar{y}_{LS}} \right] d\bar{x}d\bar{t} \tag{16}$$

This approach for calculating the total heat absorbed by the PCM from the fin requires a solution for the fin temperature distribution governed by equations (12)-(15). Equation (12) for the fin temperature is a generalization of a previously presented treatment [16] in which sensible heat storage was neglected and the phase change front was assumed to be constant in the fin equation. In contrast, equation (12) correctly accounts for transient changes in the phase change front, as well as the effect of transient changes in the fin temperature on the phase change front.

While a completely analytical solution for equation (12) is quite unlikely due to its considerable complexity, this equation provides an explicit expression for the derivative of fin temperature with time. As a result, a numerical time-stepping method is used for solving equation

(12). An implicit approach is used to ensure stability of the computations. The fin length is divided into 401 nodes. A non-dimensional timestep of 3.34×10^{-5} is used after ensuring that further shorter time steps did not significantly change the results. At each time step, a set of coupled linear algebraic equations in the unknown temperatures at the nodes are set up and solved using matrix inversion. The resulting temperature distribution is used to repeat this process at the next timestep and therefore march forward in time.

One practical challenge is that at $\bar{t}=0$, θ_f and $\bar{y}_{LS}$ are both zero, and therefore, the negative heat generation term in equation (12) can not be computed. This singularity makes it difficult to initiate the time-stepping process. In order to overcome this difficulty, an approximation is made for an initial time period $0<\bar{t}<\bar{t}^*$, during which, heat transfer from the fin into the PCM is neglected in equation (12). As a result, during this period, temperature distribution in the fin is approximated to be governed only by diffusion from the hot wall. Under this approximation, the temperature distribution during this period can be easily derived using the method of separation of variables [26] as

$$\theta_f(\bar{x}, \bar{t}) = 1 - 2 \sum_{n=1}^{\infty} \frac{1 - \cos(\beta_n)}{\beta_n} \sin(\beta_n \bar{x}) \, e^{-\beta_n^2 \bar{t}} \tag{17}$$

Where

$$\beta_n = (2n - 1)\frac{\pi}{2} \tag{18}$$

for $n=1,2,3\ldots$

Equations (17) along with the phase change front location at $\bar{t}=\bar{t}^*$ calculated using the fin temperature can be used in equation (12) in order to calculate $\frac{\partial \theta_f}{\partial \bar{t}}$ at $\bar{t}=\bar{t}^*$, and therefore, carry out

time-stepping for the fin temperature distribution starting at $\bar{t}=\bar{t}^*$. In order to minimize the error introduced by ignoring heat transfer from fin to PCM up to $\bar{t}=\bar{t}^*$ in this approach, the value of $\bar{t}^*$ must be chosen to be small compared to the total time period. The effect of $\bar{t}^*$ on the accuracy of the solution is examined later.

Considering both components of heat absorbed, an expression for the total heat absorbed by the PCM in a certain time t can be written as

$$\bar{q}_{total}(\bar{t}) = \bar{q}_1(\bar{t}) + \bar{q}_2(\bar{t})$$

$$= 2\left(1 - \frac{w}{W}\right)\frac{\sqrt{\bar{t}}}{\sqrt{\pi}\,\mathrm{erf}(\lambda)}$$

$$+ \int_0^{\bar{t}}\int_0^{\bar{L}}\left[\begin{array}{c} \dfrac{\theta_f}{\bar{y}_{LS}} + Ste\,\dfrac{\theta_f\left(\theta_f + 2\dfrac{\theta_f{}'}{\bar{y}_{LS}'}\bar{y}_{LS}\right)}{6\bar{y}_{LS}} - \\[4mm] (Ste)^2\,\dfrac{\theta_f\left(40\left(\dfrac{\theta_f{}'}{\bar{y}_{LS}'}\right)^2\bar{y}_{LS}^2 + 85\theta_f\dfrac{\theta_f{}'}{\bar{y}_{LS}'}\bar{y}_{LS} + 19\theta_f{}^2\right)}{360\bar{y}_{LS}} \end{array}\right]d\bar{x}d\bar{t} \tag{19}$$

Equation (19) shows that $\bar{q}_{total}$ has a non-monotonic dependence of w/W. As the value of w/W increases, $\bar{q}_2(\bar{t})$, the heat absorbed from the fin increases due to better thermal conduction into the fin, leading to higher fin temperature and therefore greater heat transfer into the PCM. However, as the value of w/W increases, the heat absorbed directly from the wall, $\bar{q}_1(\bar{t})$, decreases. While the relationship between w/W and $\bar{q}_1(\bar{t})$ is quite explicit, as shown in equation (4), the dependence of $\bar{q}_2(\bar{t})$ on w/W is more complicated because the solution for the differential equation for $\theta_f(\bar{x},\bar{t})$, and hence the PCM temperature distribution is not straightforward.

2-2-3. Alternate derivation of fin temperature equation

The expression for the source term in in equation (10) is derived by applying Fourier's law at the fin-PCM interface on the PCM temperature distribution given by the perturbation method solution. An alternate expression for the source term can be written by adding up latent and sensible heat storage rates in the PCM as follows:

$$\bar{S} = \frac{1}{\bar{k}_f \frac{w}{W}} \left[\frac{1}{Ste} \frac{\partial \bar{y}_{LS}}{\partial \bar{t}} + \int_0^{\bar{y}_{LS}} \frac{\partial \theta_f}{\partial \bar{t}} d\bar{y} \right] \tag{20}$$

Note that a similar analysis of this problem in the past [16] had neglected the sensible component for heat transfer from fin into the PCM.

By combining equations (20) and (5), an alternate form of the governing equation for the fin temperature distribution can be derived to be

$$\frac{\bar{c}_f}{\bar{k}_f} \frac{\partial \theta_f}{\partial \bar{t}} = \frac{\partial^2 \theta_f}{\partial \bar{x}^2} - \frac{1}{\bar{k}_f \frac{w}{W}} \left[\frac{1}{Ste} \frac{\partial \bar{y}_{LS}}{\partial \bar{t}} + \int_0^{\bar{y}_{LS}} \frac{\partial \theta_f}{\partial \bar{t}} d\bar{y} \right] \tag{21}$$

Equations (21) and (12) are expected to result in the same fin temperature distribution since the heat loss into the PCM can be equivalently computed by either applying Fourier's law at the fin-PCM interface, or by adding up sensible and latent heat storage in the PCM. Equation (21) is more complicated than equation (12) to solve, due to which, equation (12) is used in this work for understanding and optimizing heat transfer in the PCM in presence of a fin.

2-3. Results and discussion

2-3-1. Model validation

Validation of the analytical model presented in section 2 is carried out by comparison with finite-element simulations. For this purpose, an octadecane paraffin wax PCM with an aluminum fin, similar to figure 1(b) in considered. Thermal conductivity, heat capacity, density and latent heat of the PCM are taken to be 0.15 W/mK, 2300 J/kgK, 780 kg/m^3 and 244000 J/kg, respectively, corresponding to the properties of octadecane [30]. Standard values are used for thermal properties of the aluminum fin. Temperature fields in the fin and PCM are computed using the enthalpy method and the finite element technique. Grid independence is ensured by verifying minimal change in predicted temperature beyond 399600 nodes in the PCM and 44400 nodes in the fin. The PCM is defined as a homogenous binary mixture of solid and liquid phases that is initially all solid. Wall temperature is taken to be 20 K higher than the PCM melting point. The phase change process is simulated using the enthalpy method [26] which defines the phase change material as a binary mixture of liquid and solid. Thermal properties of each phase and a reference enthalpy of fusion is defined.

Figure 3(a) shows a comparison of fin temperature distribution determined from the analytical model presented in section 2 with finite-element simulation results at multiple times. The analytical model is found to be in good agreement with finite-element simulations at each of the plotted times. Figure 3(b) plots the location of the phase change front along the fin at multiple times. Similar to Figure 3(a), good agreement is obtained between the analytical model and finite-element simulations. Note that these calculations use a value of $\bar{t}^* = 3.34 \times 10^{-5}$, which represents only 0.05% of the total time. The small value of $\bar{t}^*$ minimizes the error associated with the approximation needed at early time.

Further, Figure 4 presents colormaps of temperature distribution in the PCM and fin at multiple times predicted by the finite-element simulations. Heat diffusion into the fin, as well as heat transfer into the PCM through two distinct mechanisms – direct conduction from wall on the left, and conduction through the fin on the bottom – are all clearly seen in these plots. Two nearly independent phase change fronts originating from the PCM-wall and PCM-fin interfaces are seen. These plots show that at each time, the melting fronts from the left and bottom do not interact significantly with each other, except for a small region close to $\bar{x}=0$ where melting occurs from both left and bottom. This justifies a key assumption in the analytical model presented in section 2.
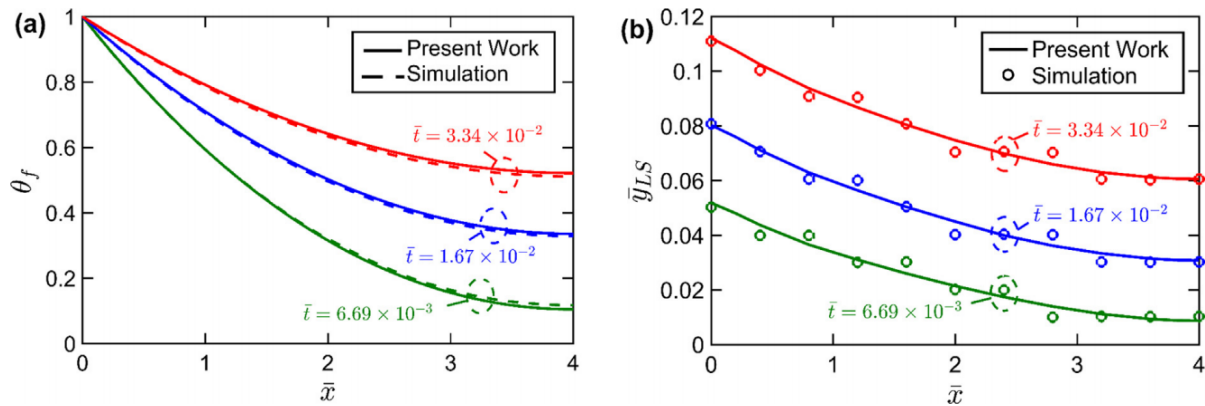
Figure 3. Validation of results by comparison between theoretical model and finite-element simulations. (a) Temperature distribution in the fin at multiple times; (b) location of the phase change front across the fin at multiple times. In these plots, w/W=0.1, $\bar{L}$=4, Ste=0.19, $\bar{k}_f$=1580 and $\bar{c}_f$=1.36. Properties of octadecane and Aluminum are assumed for PCM and fin respectively.
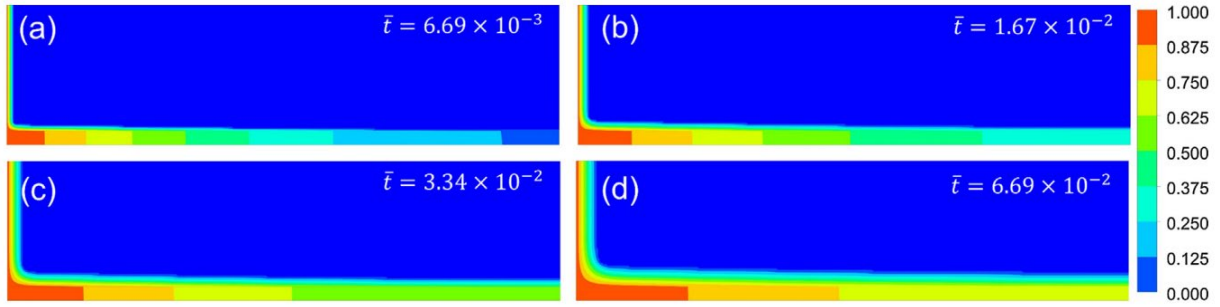
Figure 4. Temperature map determined from finite-element simulations for the problem considered in figure 3. Location of the fin is emphasized with dark lines.

2-3-2. Optimal value of *w/W*

Figures 5(a)-(f) plot the two components of heat transfer into the PCM as well as total heat transferred up to $\bar{t} = 6.69 \times 10^{-2}$ determined from equations (4), (16) and (19) as functions of the relative fin size *w/W* for multiple values of fin thermal conductivity $\bar{k}_f$. Other thermophysical properties are held constant. For comparison, the total non-dimensional heat absorbed in a baseline case with no fin is 0.895.

These plots clearly show that the larger the fin thermal conductivity, the higher is the heat absorbed. However, for a fixed fin thermal conductivity, each of these Figures show the existence of an optimal value of *w/W* that maximizes total heat absorbed. As *w/W* increases, the reduced thermal resistance of the fin results in greater heat transfer into the fin, higher fin temperature and therefore, $\bar{q}_2$ increases with *w/W*. However, an increase in *w/W* is also seen to result in a reduction in $\bar{q}_1$, because a larger value of *w/W* results in a greater area of the wall being occupied by the fin, and therefore reduces the area of contact directly between the wall and the PCM. While $\bar{q}_1$ reduces linearly with *w/W*, the increase in $\bar{q}_2$ with *w/W* is sharp initially, and then linear. The total heat absorbed from the wall and fin, given by the sum of $\bar{q}_1$ and $\bar{q}_2$, plotted in Figures 5(a)-(f) has a

non-monotonic dependence on *w/W*. with a peak occurring at a reasonably low value of *w/W*. This means that even a very small fin width provides sufficient thermal conductance into the fin to positively impact the total heat flow into the PCM. Beyond this peak value, further increasing the fin size is not beneficial because at the peak, thermal resistance of the fin is already quite low and does not reduce meaningfully by increasing *w/W* further. When this state is reached, further increase in *w/W* reduces $\bar{q}_1$ without contributing much towards increasing $\bar{q}_2$. This is further illustrated in Figure 6 which plots fin temperature distribution at $\bar{t} = 6.69 \times 10^{-2}$ for different values of *w/W*, with $\bar{k}_f$=1333. Figure 6 shows sharp increase in fin temperature distribution with increasing *w/W* when *w/W* is small. However, this effect saturates when *w/W* is somewhat large because at that point, further increasing *w/W* does not significantly reduce thermal resistance of the fin, which is already quite low. This illustrates the importance of carefully choosing the fin size relative to the wall in order to balance the two conflicting considerations in maximizing overall heat transfer into the PCM.
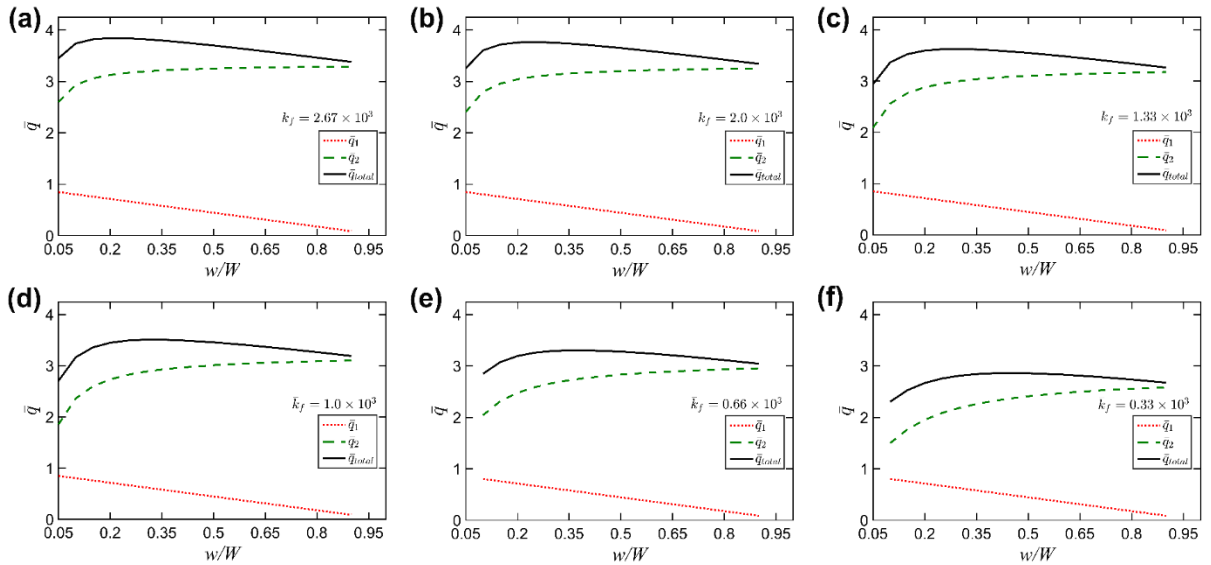
Figure 5. Total heat absorbed by the PCM up to $\bar{t} = 6.69 \times 10^{-2}$, including the wall and fin components. (a)-(f) present plots for six different fin thermal conductivities. In these plots, $\bar{L}$=4, Ste=0.19 and $\bar{c}_f$=1.36

Thermal conductivity of the fin plays a key role is determining the optimal value of w/W.

Figure 7(a) plots the total heat absorbed as a function of w/W for multiple values of $\bar{k}_f$. These

curves clearly show a distinct shift in the location of the maxima as $\bar{k}_f$ reduces. Figure 7(b) plots

the optimal value of w/W corresponding to the peak as a function of $\bar{k}_f$. This plot shows that the

higher the value of $\bar{k}_f$, the lower is the value of w/W at which the peak of energy stored occurs.

This is because thermal resistance of a high thermal conductivity fin saturates at a lower fin size,

whereas thermal resistance of a low thermal conductivity fin can continue to improve as the fin

size increases. The dependence of peak energy storage performance on thermal conductivity

illustrated in Figures 7(a) and 7(b) is important to account for in practical fin design because if the

fin size is greater than the optimal value for the thermal conductivity of the fin, then the fin is

counter-productive and actually impedes flow of heat into the PCM.
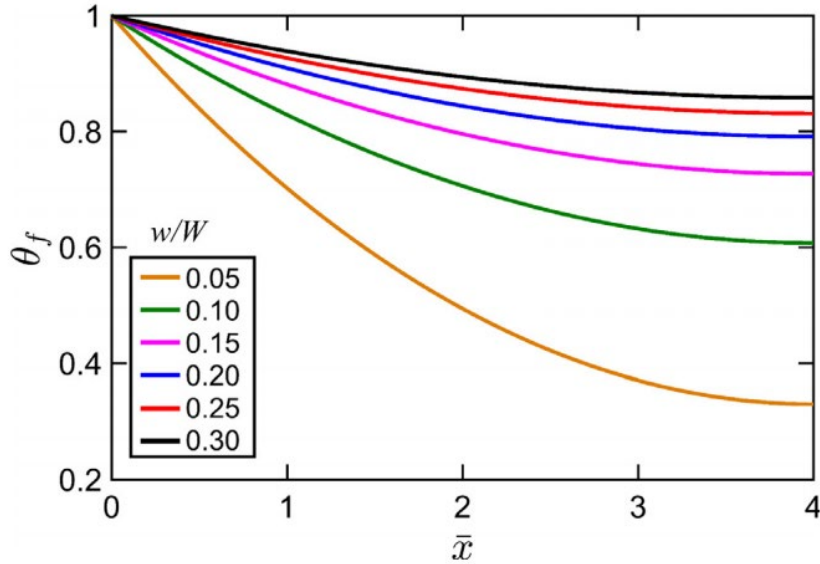
Figure 6. Fin temperature distribution at $\bar{t} = 6.69 \times 10^{-2}$ for multiple values of w/W. In this plot, $\bar{k}_f$=1333, $\bar{L}$=4, Ste=0.19 and $\bar{c}_f$=1.36.
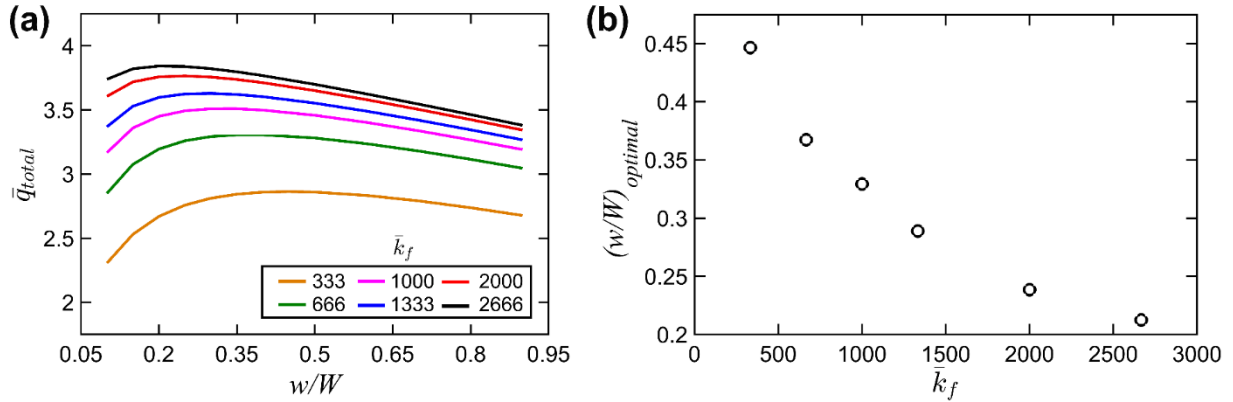
Figure 7.(a) Plot of $\bar{q}_{total}$ at $\bar{t} = 6.69 \times 10^{-2}$ as a function of w/W for different values of thermal conductivity. (b) Optimal value of w/W as a function of fin thermal conductivity. In these plots, $\bar{L}$=4, Ste=0.19 and $\bar{c}_f$=1.36.

2-3-3. Effect of time available for heat transfer

The total time available for heat transfer into the PCM plays a key role in determining the impact of the fin. In principle, if infinite time is available, then the PCM will eventually reach the wall temperature, and therefore, the presence of the fin is un-necessary and actually counter-productive, since it reduces PCM volume. However, when only a short time is available, the fin may contribute towards increasing overall energy storage by offering an alternate path for heat transfer into the PCM. The dependence of the optimal fin size on available time is investigated. Figure 8 plots the optimal value of w/W that results in the highest possible total energy stored as a function of the total time available for heat transfer. Figure 8 shows that as time increases, the optimal fin becomes thinner and thinner. This occurs because at larger times, the role of the fin in increasing surface area and promoting indirect heat transfer into the PCM diminishes, and the negative impact of reduced PCM volume and reduced area of wall-PCM contact becomes more and more important. Figure 8 illustrates the important role of available time on the optimal design of the fin for promoting heat transfer into the PCM.
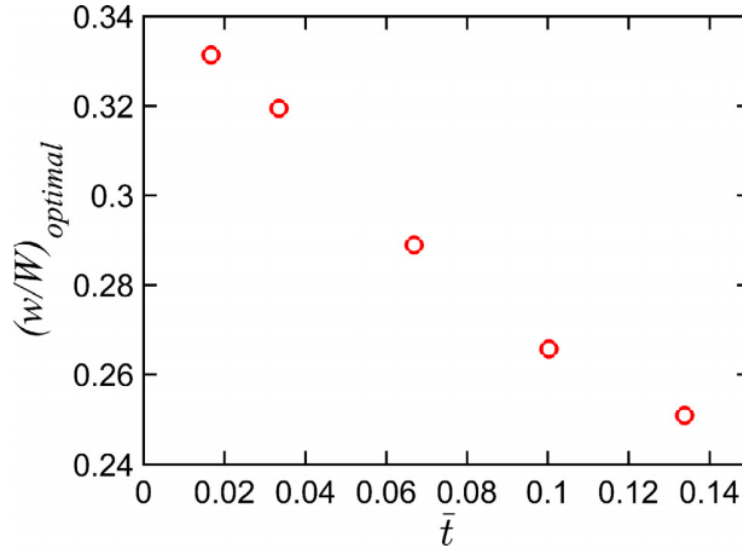
Figure 8. Effect of total time available for heat transfer on the optimal fin thickness that maximizes total amount of heat stored. In this plot, $\bar{L}$=4, Ste=0.19, $\bar{c}_f$=1.36 and $\bar{k}_f$=1333.

2-3-4. Impact of thermal properties

Figure 9 examines the effect of material thermal properties on energy storage performance. Total heat absorbed by a fin with w/W=0.2 up to $\bar{t} = 6.69 \times 10^{-2}$ is plotted as a function of $\bar{k}_f$ in Figure 9 for octadecane PCM. The two components of total heat absorbed – $\bar{q}_1$ and $\bar{q}_2$ – are also plotted for comparison. Figure 9 shows that while $\bar{q}_1$ remains unchanged with increasing $\bar{k}_f$ because fin thermal conductivity does not affect heat absorbed directly from the wall, $\bar{q}_2$ increases with $\bar{k}_f$ because of the increased thermal diffusion into the fin and therefore enhanced heat transfer into the PCM. On the overall, the total energy absorbed by the PCM increases with increasing k_f.
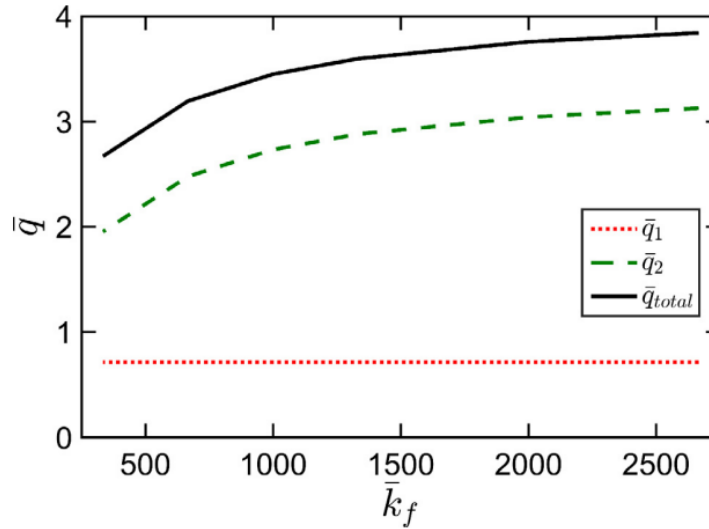
Figure 9. Effect of fin thermal conductivity on heat absorbed from the wall and fin, as well as total heat absorbed up to $\bar{t} = 6.69 \times 10^{-2}$. In this plot, $\bar{L}$=4, Ste=0.19, $\bar{c}_f$=1.36 and w/W=0.2.

2-3-5. Impact of sensible heat storage

Figure 10 examines the importance of accounting for latent and sensible heat storage in the PCM on the results of the analytical model. In the alternate derivation of the fin temperature equation, the heat loss term, equation (20), has explicit terms for the contributions of latent and sensible heat storage mechanisms. Using the resulting equation (21) for determining the fin temperature distribution, Figure 10 plots fin temperature distribution at multiple times without and with sensible heat storage accounted for. Plots are presented in Figures 10(a) and 10(b) for two different values of the wall temperature relative to the melting temperature. For a relatively small value of Ste=0.19, the error involved in neglecting sensible heat storage is found to be reasonably small. However, for a larger value of Ste=0.94, the error is much more significant. Figure 10 shows that this error also grows as time increases.
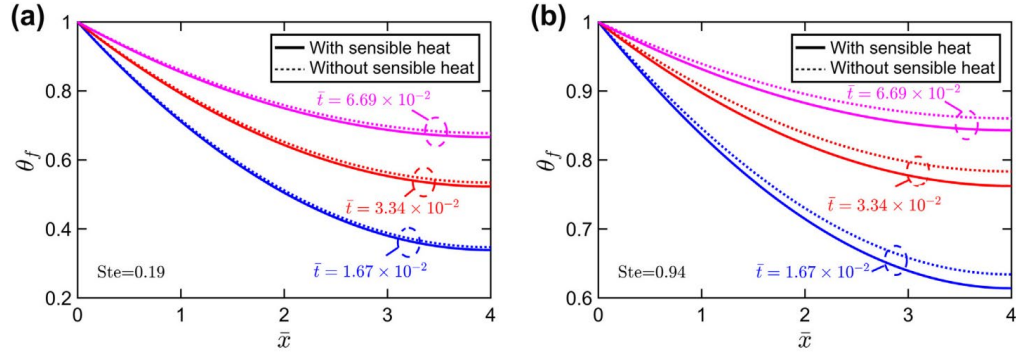
Figure 10. Effect of accounting for sensible heat storage. (a) and (b) plot fin temperature distribution at different times for two different values of Ste. In these plots, $\bar{L}=4$, $\bar{k}_f=1580$, $\bar{c}_f=1.36$ and $w/W=0.1$

2-3-6. Effect of $\bar{t}^*$

Determining the fin temperature distribution from equation (12) requires an approximation to handle the singularity at $\bar{t}=0$, wherein heat transfer into the fin is assumed to occur without heat loss to the PCM for a short initial time, up to $\bar{t}=\bar{t}^*$. Clearly, the larger the value of $\bar{t}^*$, the greater is the error incurred due to neglecting the heat loss into PCM. Figure 11 plots temperature distribution in the fin at the final time $\bar{t}=1.67\times10^{-2}$ for multiple values of $\bar{t}^*$. For comparison, a plot based on a finite-element simulation that does not incur this error is also presented. Figure 11 clearly shows significant error when $\bar{t}^*$ is large. This error reduces rapidly as $\bar{t}^*$ reduces. In this specific case, a value of $\bar{t}^*=3.34\times10^{-5}$ results in reasonable agreement between the analytical model and finite-element simulation. Note that the need to utilize an initial period that neglects heat loss into the PCM results from the singularity in equation (12) that makes it impossible to initiate time-stepping at $\bar{t}=0$ to compute the fin temperature distribution as a function of time.
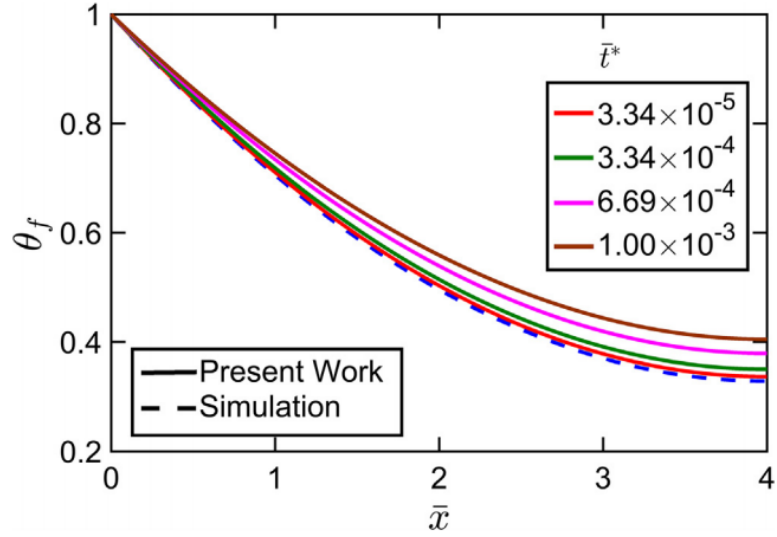
Figure 11. Effect of the value of $\bar{t}^*$ on the accuracy of fin temperature distribution computed from equation (12) for a total time of $\bar{t} = 1.67 \times 10^{-2}$. Result from a finite element simulation is also shown for comparison. In this plot, $\bar{L}$=4, $\bar{k}_f$=1580, $\bar{c}_f$=1.36 and w/W=0.1

2-4. Conclusions

It is important to complement experimental research on enhancement of phase change energy storage through extended surfaces with theoretical modeling of heat transfer in such systems. The transient and non-linear nature of heat transfer in such processes results in complicated governing equations for the temperature distribution. The equations derived in this work correctly account for several phenomena that were unaccounted for in past papers, including sensible heat storage in the newly formed phase and transient variation in phase change front location. Consequently, this work establishes the existence of an optimal fin size that maximizes the benefit of the fin on heat transfer into the PCM.

From a theoretical perspective, this work generalizes the well-known, linear differential equation for steady-state temperature distribution for a fin in a single phase fluid to a significantly

more complicated non-linear differential equation for a fin in a phase change material. From a practical perspective, the fin temperature distribution and the consequent computation of heat absorbed by the PCM are critical insights, and offer guidelines for the optimal design of phase change energy storage systems that occur in several engineering applications. Specifically, the optimal fin size for maximum heat transfer into the PCM, and the dependence of this optimal fin size on thermal properties and the available time window are both important and practical guidelines.

The present work neglects the effect of natural convection in the liquid phase, which, while not important for the geometry considered here, may be significant in other scenarios, for example, in a long, vertical PCM layer [7]. The effect of temperature-dependence of thermal properties, while neglected here, may also be important to account for in scenarios with relatively large temperature change.

2-5. Nomenclature

c volumetric heat capacity (J/m^{3}K)

C_p specific heat capacity (J/kg K)

$\bar{c}_f$ non-dimensional fin volumetric heat capacity, $\bar{c}_f = \frac{c_f}{c_p}$

k thermal conductivity (W/mK)

$\bar{k}_f$ non-dimensional fin thermal conductivity, $\bar{k}_f = \frac{k_f}{k_p}$

L fin length (m)

$\bar{L}$ non-dimensional fin length, $\bar{L} = \frac{L}{W}$

L_p latent heat of fusion (J/kg)

q heat absorbed per unit depth (J/m)

$\bar{q}$ non-dimensional heat absorbed, $\bar{q} = \dfrac{q}{(T_w - T_m)c_p W^2}$

q''_{f-p} heat flux from fin into PCM (W/m^2)

Q'' thermal conduction heat flux (W/m^2)

$\bar{S}$ non-dimensional source term, $\bar{S} = \dfrac{q''_{f-p}W}{w/W(T_w - T_m)k_f}$

Ste Stefan number, $Ste = \dfrac{c_p(T_W - T_m)}{L_p}$

t time (s)

$\bar{t}$ non-dimensional time, $\bar{t} = \dfrac{\alpha_p t}{W^2}$

T temperature (K)

T_m phase change temperature (K)

T_w wall temperature (K)

w fin width (m)

W width of the domain (m)

x,y spatial coordinates (m)

$\bar{x}, \bar{y}$ non-dimensional spatial coordinates, $\bar{x} = \dfrac{x}{W}, \bar{y} = \dfrac{y}{W}$

x_{LS} location of phase change front originating from fin (m)

$\bar{x}_{LS}$ non-dimensional location of phase change front originating from fin, $\bar{x}_{LS} = \dfrac{x_{LS}}{W}$

y_{LS} location of phase change front originating from fin (m)

$\bar{y}_{LS}$ non-dimensional location of phase change front originating from fin, $\bar{y}_{LS} = \dfrac{y_{LS}}{W}$

Greek symbols

α thermal diffusivity (m^2/s)

β non-dimensional eigenvalues

θ non-dimensional temperature, $\theta = \frac{T-T_m}{T_W-T_m}$

λ non-dimensional eigenvalues

Subscripts and superscripts

f fin

p phase change material

*   initial approximation

2-6. References

[1] H. Zhang, J. Baeyens, J. Degrève, G. Cacères, Concentrated solar power plants: Review and design methodology, Renewable and Sustainable Energy Reviews. 22 (2013) 466–481. doi:10.1016/j.rser.2013.01.032.

[2] K. Bhagat, S.K. Saha, Numerical analysis of latent heat thermal energy storage using encapsulated phase change material for solar thermal power plant, Renewable Energy. 95 (2016) 323–336. doi:10.1016/j.renene.2016.04.018.

[3] M. Kenisarin, K. Mahkamov, Solar energy storage using phase change materials☆, Renewable and Sustainable Energy Reviews. 11 (2007) 1913–1965. doi:10.1016/j.rser.2006.05.005.

[4] A. Sharma, V. Tyagi, C. Chen, D. Buddhi, Review on thermal energy storage with phase change materials and applications, Renewable and Sustainable Energy Reviews. 13 (2009) 318–345. doi:10.1016/j.rser.2007.10.005.

[5] J. Eftekhar, A. Haji-Sheikh, D.Y.S. Lou, Heat Transfer Enhancement in a Paraffin Wax Thermal Storage System, Journal of Solar Energy Engineering. 106 (1984) 299. doi:10.1115/1.3267599.

[6] W.R. Humphries, E.I. Griggs, A design handbook for phase change thermal control and energy storage devices, National Aeronautics and Space Administration, Scientific and Technical Information Office, Washington, 1977. NASA Technical Paper 1074.

[7] V. Shatikian, G. Ziskind, R. Letan, Numerical investigation of a PCM-based heat sink with internal fins, International Journal of Heat and Mass Transfer. 48 (2005) 3689–3706. doi:10.1016/j.ijheatmasstransfer.2004.10.042.

[8] T. Rozenfeld, Y. Kozak, R. Hayat, G. Ziskind, Close-contact melting in a horizontal cylindrical enclosure with longitudinal plate fins: Demonstration, modeling and application to thermal storage, International Journal of Heat and Mass Transfer. 86 (2015) 465–477. doi:10.1016/j.ijheatmasstransfer.2015.02.064.

[9] Y. Kozak, T. Rozenfeld, G. Ziskind, Close-contact melting in vertical annular enclosures with a non-isothermal base: Theoretical modeling and application to thermal storage, International Journal of Heat and Mass Transfer. 72 (2014) 114–127. doi:10.1016/j.ijheatmasstransfer.2013.12.058.

[10] H. Shmueli, G. Ziskind, R. Letan, Melting in a vertical cylindrical tube: Numerical investigation and comparison with experiments, International Journal of Heat and Mass Transfer. 53 (2010) 4082–4091. doi:10.1016/j.ijheatmasstransfer.2010.05.028.

[11] L.-W. Fan, Y.-Q. Xiao, Y. Zeng, X. Fang, X. Wang, X. Xu, et al., Effects of melting temperature and the presence of internal fins on the performance of a phase change material (PCM)-based heat sink, International Journal of Thermal Sciences. 70 (2013) 114–126. doi:10.1016/j.ijthermalsci.2013.03.015.

[12] B. Kamkari, H. Shokouhmand, Experimental investigation of phase change material melting in rectangular enclosures with horizontal partial fins, International Journal of Heat and Mass Transfer. 78 (2014) 839–851. doi:10.1016/j.ijheatmasstransfer.2014.07.056.

[13] U. Stritih, An experimental study of enhanced heat transfer in rectangular PCM thermal storage, International Journal of Heat and Mass Transfer. 47 (2004) 2841–2847. doi:10.1016/j.ijheatmasstransfer.2004.02.001.

[14] A. Abhat, S. Aboul-Enein, N.A. Malatidis, Heat-of-Fusion Storage Systems for Solar Heating Applications, Thermal Storage of Solar Energy. (1981) 157–171. doi:10.1007/978-94-009-8302-1_17.

[15] M. Huang, P. Eames, B. Norton, Thermal regulation of building-integrated photovoltaics using phase change materials, International Journal of Heat and Mass Transfer. 47 (2004) 2715–2733. doi:10.1016/j.ijheatmasstransfer.2003.11.015.

[16] P. Lamberg, K. Sirén, Approximate analytical model for solidification in a finite PCM storage with internal fins, Applied Mathematical Modelling. 27 (2003) 491–513. doi:10.1016/s0307-904x(03)00080-5.

[17] P. Lamberg, Approximate analytical model for two-phase solidification problem in a finned phase-change material storage, Applied Energy. 77 (2004) 131–152. doi:10.1016/s0306-2619(03)00106-5.

[18] P. Lamberg, K. Sirén, Analytical model for melting in a semi-infinite PCM storage with an internal fin, Heat and Mass Transfer. 39 (2003) 167–176. doi:10.1007/s00231-002-0291-1.

[19] F. Talati, A.H. Mosaffa, M.A. Rosen, Analytical approximation for solidification processes in PCM storage with internal fins: imposed heat flux, Heat and Mass Transfer. 47 (2010) 369–376. doi:10.1007/s00231-010-0729-9.

[20] J. Leland, G. Recktenwald, Optimization of a phase change heat sink for extreme environments, Ninteenth Annual IEEE Semiconductor Thermal Measurement and Management Symposium, 2003. (n.d.). doi:10.1109/stherm.2003.1194384.

[21] R. Akhilesh, A. Narasimhan, C. Balaji, Method to improve geometry for heat transfer enhancement in PCM composite heat sinks, International Journal of Heat and Mass Transfer. 48 (2005) 2759–2770. doi:10.1016/j.ijheatmasstransfer.2005.01.032

[22] P.P. Levin, A. Shitzer, G. Hetsroni, Numerical optimization of a PCM-based heat sink with internal fins, International Journal of Heat and Mass Transfer. 61 (2013) 638–645. doi:10.1016/j.ijheatmasstransfer.2013.01.056.

[23] A. Nagose, A. Somani, A. Shrot, A. Narasimhan, Genetic Algorithm Based Optimization of PCM Based Heat Sinks and Effect of Heat Sink Parameters on Operational Time, Journal of Heat Transfer. 130 (2008) 011401.

[24] P.H. Biwole, D. Groulx, F. Souayfane, T. Chiu, Influence of fin size and distribution on solid-liquid phase change in a rectangular enclosure, International Journal of Thermal Sciences. 124 (2018) 433–446. doi:10.1115/1.2780182.

[25] T. Bauer, Approximate analytical solutions for the solidification of PCMs in fin geometries using effective thermophysical properties, International Journal of Heat and Mass Transfer. 54 (2011) 4923–4930. doi:10.1016/j.ijheatmasstransfer.2011.07.004.

[26] D.W. Hahn, M.N. Özişik, Heat Conduction, (2012) Third ed., John Wiley & Sons, Hoboken, New Jersey.

[27] T.L. Bergman, D.P. Dewit, A.S. Lavine, F.P. Incropera, Fundamentals of heat and mass trasnfer, (2011) John Wiley & Sons, New Jersey.

[28] J. Caldwell, Y. Kwan, On the perturbation method for the Stefan problem with time-dependent boundary conditions, International Journal of Heat and Mass Transfer. 46 (2003) 1497–1501. doi:10.1016/s0017-9310(02)00415-5.

[29] G. Lock, J. Gunderson, D. Quon, J. Donnelly, A study of one-dimensional ice formation with particular reference to periodic growth and decay, International Journal of Heat and Mass Transfer. 12 (1969) 1343–1352. doi:10.1016/0017-9310(69)90021-0.

[30] N.R. Jankowski, F.P. Mccluskey, A review of phase change materials for vehicle component thermal buffering, Applied Energy. 113 (2014) 1525–1561. doi:10.1016/j.apenergy.2013.08.026.

Chapter 3

Semi-analytical thermal modeling of transverse and longitudinal fins in a cylindrical phase change energy storage system

3-1. Introduction

Renewable energy technologies such as solar energy have been widely investigated in the past to meet the world's energy demand with minimal environmental impact. The unsteady and intermittent nature of renewable energy, however, remains a key challenge. Thermal energy storage (TES) systems can play a vital role in alleviating these challenges by storing and releasing excess renewable energy during periods of availability and demand respectively [1,2].

Thermal energy can be stored using a variety of mechanisms, such as sensible heat [3], latent heat [4] and thermochemical energy [5]. Amongst these, latent heat storage offers advantages of compactness and capability of storing high amount of energy associated with the liquid-to-solid transition of the phase change material (PCM). However, due to the thermal resistance offered by the newly formed phase, the rate of energy storage tends to slow down over time [6]. As a result, enhancing the rate and magnitude of latent energy storage has attracted considerable research [7,8]. A large body of literature exists on possible enhancement mechanisms. Two broad classes of such mechanisms include enhancement of PCM thermal properties through dispersion of nano/micro-particles [9,10] and enhancement of heat transfer into the PCM through extended surfaces such as fins and foams [11,12].

For the case of heat transfer between a hot/cold cylinder of radius R_i and a surrounding annular bed of PCM between $r=R_i$ and $r=R_o$, transverse and longitudinal fins have been commonly used for heat transfer enhancement. These are shown schematically in Figures 1(a) and 1(b), respectively. Transverse fins extend throughout circumferentially, with a height w that is lower than the PCM height W in the axial direction. In contrast, longitudinal fins extend through the entire height of the geometry, but are limited to an angle $2\varphi_f$ in the circumferential direction. Both fin types have been investigated extensively through experiments and modeling for enhancement

of heat transfer into the PCM [13-22]. The effect of number of fins on rate of PCM solidification was numerically and experimentally studied in transverse and longitudinal configurations. It was shown that increase in number of fins decreases solidification time [13,14]. A similar study with constant thickness longitudinal fins reported that 4-5 fins offer optimal performance [15]. A numerical study showed overall heat transfer increase with number of fins for a transverse finned storage system [16]. Groulx et al. experimentally investigated melting and solidification in a cylindrical thermal storage system with four longitudinal fins. It was found that solidification process is conduction-dominated throughout, but melting is conduction-dominated only in early stages [17]. The effect of fluid flow rate on melting time in a solar domestic hot water system with longitudinal fins was examined experimentally [18]. The melting time is found to be a strong function of heat transfer fluid flow rate during the charging process, with no effect on the rate of solidification during the discharging process [18]. Measurements have been reported for the effects of heat transfer flow rate and temperature on charging and discharging processes in a finned tube heat exchanger [19]. Ziskind et al. investigated close contact melting (CCM) effects on thermal performance of finned latent heat energy storage enclosures numerically and experimentally. CCM has been reported to improve the melting rate and shorten the melting time by 2.5 times for both transverse and longitudinally finned systems. Similar trend was demonstrated in a helical fined system [20-22]. A numerical study has reported that energy storage increased with decreasing fin pitch and increasing fin length [23]. Another numerical study on energy storage in a transverse finned system showed that the heat storage rate and energy efficiency ratio are largely insensitive to fin geometry when the fin pitch is more than four times the inner radius height and fin length [24]. Using longer and thicker fins improves thermal performance of the system when the fin pitch is small [24]. Effects of length, thickness and number of longitudinal fins on charging and

41

discharging in a triplex tube heat exchanger were investigated numerically by considering pure conduction and natural convection, and the results were validated with experimental results. The effect of length and number of fins on the melting and freezing times was stronger than those of fin thickness [25,26]. An experimental study showed that the effective thermal conductivity of the PCM can be raised by up to three times by using fins in an annular storage system. It is found that fin size fin and pitch are the key parameters that affect thermal conductivity enhancement [27].

The literature survey presented above shows that optimization of a finned geometry for improving the rate of energy storage is of significant interest. As outlined above, multiple papers have investigated this problem through experiments or numerical simulations for specific geometries. However, there remains a distinct lack of generalized theoretical analysis of this problem for transverse and longitudinal fins. While the presence of a fin may offer extended surface area for heat transfer to the PCM, it also displaces PCM volume that could store energy and reduces the area of direct contact between the PCM and the inner wall. This may not be an important consideration – and fins are not needed at all – if infinite time is available for heat transfer because in such a case, all the PCM will melt. However, for a given finite time window available for heat transfer, which is the case for most practical applications, the analysis of trade-offs between these competing effects is essential for understanding how the fin geometry affects the amount of stored energy. Some research exists on theoretical and numerical analysis of heat transfer in fins in Cartesian systems [28-32]. Past work has shown [28] that a certain fin size – the value of which is a function of fin thermal properties – maximizes the thermal benefit of the fin through a careful balance between the two processes described above. However, there is a lack of similar work for cylindrical phase change energy storage systems. For the specific case of transverse and longitudinal fins shown in Figures 1(a) and 1(b), it is of interest to determine how

the fin size relative to PCM, *w/W* and the angle *2φf* respectively, affect energy storage for a given time duration.

This paper presents analysis of heat transfer into an annular PCM bed from an inner heat source in the presence of transverse or longitudinal fins, with focus on understanding the impact of fin geometry and thermal properties on the amount of energy stored. Governing equations for heat transfer into the PCM, both directly from the wall and through the fins are derived. Sensible and latent heat storage in the PCM are both accounted for. Based on a semi-analytical method, expressions for the total stored energy in the PCM for a given finite time as a function of fin geometry and thermal properties are derived for both transverse and longitudinal fins. Dependence of total stored energy in the PCM on fin size is investigated.
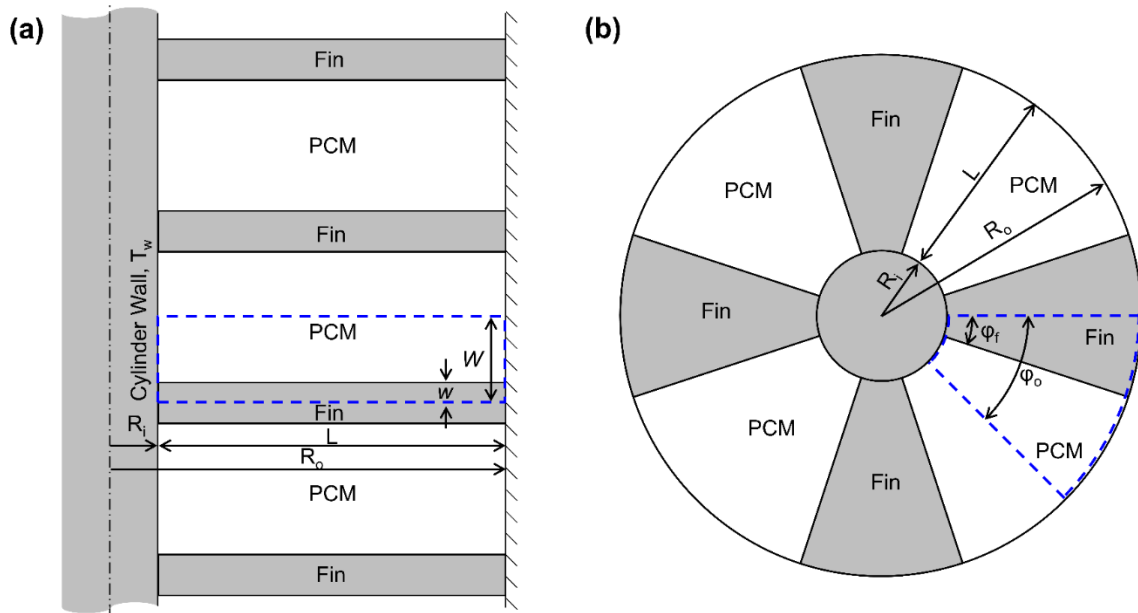
Figure 1. (a) Schematic cross-section view of multiple transverse fins protruding into an annular PCM bed around a cylindrical heat source; (b) Schematic top view of multiple longitudinal fins protruding into an annular PCM bed around a cylindrical heat source. Unit thermal cells based on symmetry are shown within broken lines for each case.

3-2. Theoretical model

This section develops theoretical models for heat transfer from a constant temperature cylinder into a surrounding, annular PCM bed. Specifically, the effect of two types of fins between the inner and outer radii, R_i and R_o respectively, is captured in these models. As shown in Figure 1(a), transverse fins go all around circumferentially, with a thickness w that is lower than the height W of the thermal unit cell. In contrast, as shown in Figure 1(b), longitudinal fins extend through the entire height of the geometry, but not in the circumferential direction. Given a fixed total number of longitudinal fins, the angular width of each fin $2\varphi_f$ is an important design parameter, similar to w for the transverse fins. In general, as w or φ_f increases, in the cases of transverse and longitudinal fins, respectively, the area of direct contact between PCM and wall reduces, which inhibits the total amount of direct heat transfer to the PCM in a given total time. However, this also results in greater temperature rise in the fin itself, which provides an additional path for heat transfer into the PCM. Therefore, the effect of w or φ_f on overall heat transfer is important to quantify. Note that this is an interesting problem only for a given, finite amount of time available for heat transfer. At infinite time, all of the PCM will melt and reach the wall temperature, and therefore, presence of any fin material is undesirable as it reduces the volume of PCM available and hence the total amount of heat stored.

The next two sub-sections consider geometries with transverse and longitudinal fins, respectively, and derive governing equations for the fin temperature distribution and expressions for the total heat stored in terms of the fin temperature distribution. In each case, the total heat transfer into the PCM is written as the sum of two distinct modes of heat transfer due to two independent, non-overlapping propagation fronts – heat transfer directly from the wall to the PCM, and heat transfer into the PCM indirectly through the fin.

3-2-1. Transverse fin

In this case, transverse fins extending throughout the circumferential direction and between $r=R_i$ to $r=R_o$ in the radial direction are considered. The fin pitch and fin height in the axial direction are taken to be *2W* and *2w*, respectively, so that heat transfer analysis can be simplified by modeling an axisymmetric unit cell, as shown in Figure 2(a). Both fin and PCM are assumed to be at PCM melting temperature T_m initially. Note that k and c denote thermal conductivity and volumetric heat capacity, respectively. Subscripts f and p denote fin and PCM, respectively. L_p represents latent heat of PCM. All properties are assumed to be independent of temperature. Total heat absorbed by the PCM up to time, t, $q(t)$ comprises two distinct components –heat absorbed by the PCM directly from the width *(W-w)* of the heat source, $q_1(t)$, and heat absorbed by the PCM from the fin, $q_2(t)$.

These components are shown in Figure 2(a). The first component, $q_1(t)$, depends only on the cylinder temperature $(T_w\text{-}T_m)$ and PCM properties. On the other hand, the second component, $q_2(t)$, depends additionally on fin properties because it is governed by the extent of thermal diffusion into the fin. $q_1(t)$ and $q_2(t)$ independently initiate and propagate melting fronts in r and z directions, respectively. Neglecting the small region near the origin where these two fronts merge, one may determine $q_1(t)$ and $q_2(t)$ independently. Such a simplifying assumption of independent phase change fronts is commonly made to simplify two-dimensional phase change problems [28,29,33]. Expressions for $q_1(t)$ and $q_2(t)$ are now derived separately.

3-2-1-1. $q_1(t)$ for transverse fin

The $q_1(t)$ component can be determined by solving the problem of phase change propagation into an infinite PCM from a constant temperature cylinder of radius R_i. While similar to the classical Stefan problem in Cartesian coordinates, this problem does not appear to have an exact

analytical solution. Parhizi & Jain [34] have presented a solution for this problem based on perturbation method. Referring to the non-dimensionalization summarized in the Nomenclature section, the location of the solid-liquid interface location, $\bar{r}_{LS}$ as a function of non-dimensional time $\bar{t}$ is given by the following inverse relationship

$$
\begin{aligned}
\bar{t} &= \Bigg[\frac{\left(2\left(\bar{r}_{LS}(\bar{t})\right)^2 \log \bar{r}_{LS}(\bar{t}) + 1\right)}{4} \\
&+ \frac{Ste}{4 \log \bar{r}_{LS}(\bar{t})} \left(\left(\bar{r}_{LS}(\bar{t})\right)^2 \log \bar{r}_{LS}(\bar{t}) + \log \bar{r}_{LS}(\bar{t}) - (\bar{r}_{LS}(\bar{t}))^2 + 1\right) \\
&+ \frac{Ste^2}{128\left(\bar{r}_{LS}(\bar{t})\right)^2 \log \bar{r}_{LS}(\bar{t})} \Big(\left(\bar{r}_{LS}(\bar{t})\right)^4 (8\, (\log \bar{r}_{LS}(\bar{t}))^3 - 20\, (\log \bar{r}_{LS}(\bar{t}))^2 + 21 \log \bar{r}_{LS}(\bar{t}) \\
&- 8) - 16\left(\bar{r}_{LS}(\bar{t})\right)^2 (\log \bar{r}_{LS}(\bar{t}) - 1) - 5 \log \bar{r}_{LS}(\bar{t}) - 8\Big) \Bigg]
\end{aligned}
\tag{1}
$$

Consequently, the total heat absorbed by the PCM directly from the cylinder wall, $q_1(t)$ considering the reduced area of direct contact due to the presence of the fin, as shown in Figure 2(a), is given by differentiating the temperature distribution in the PCM at the interface $r=R_i$ [34]. The final result is

$$\bar{q}_1(\bar{t}) = -2\left(1 - \frac{\bar{w}}{\bar{W}}\right)\int_0^{\bar{t}} \left(\frac{\partial \theta_p}{\partial \bar{r}}\right)_{\bar{r}=\bar{R}_i} d\bar{t}$$

$$= \int_0^{\bar{t}} -2\left(1\right.$$

$$-\frac{\bar{w}}{\bar{W}}\right)\left(\left(\left(\frac{\left(10(\bar{r}_{LS}(\bar{t}))^4 + 8(\bar{r}_{LS}(\bar{t}))^2 - 6\right)}{64(\bar{r}_{LS}(\bar{t}))^4(\log \bar{r}_{LS}(\bar{t}))^4}\right.\right.$$

$$- \frac{\left(5(\bar{r}_{LS}(\bar{t}))^2 - 1\right)^2}{16(\bar{r}_{LS}(\bar{t}))^4(\log \bar{r}_{LS}(\bar{t}))^7}$$

$$- \frac{\left(56(\bar{r}_{LS}(\bar{t}))^4 + 24(\bar{r}_{LS}(\bar{t}))^2 + 44\right)}{128(\bar{r}_{LS}(\bar{t}))^4(\log \bar{r}_{LS}(\bar{t}))^5}$$

$$+ \left.\frac{\left((\bar{r}_{LS}(\bar{t}))^2 - 1\right)\left(71(\bar{r}_{LS}(\bar{t}))^2 + 71\right)}{128(\bar{r}_{LS}(\bar{t}))^4(\log \bar{r}_{LS}(\bar{t}))^6}\right)Ste^2$$

$$+ \left(\frac{\left((\bar{r}_{LS}(\bar{t}))^2 - 1\right)}{4(\bar{r}_{LS}(\bar{t}))^2(\log \bar{r}_{LS}(\bar{t}))^4} - \frac{\left((\bar{r}_{LS}(\bar{t}))^2 + 1\right)}{4(\bar{r}_{LS}(\bar{t}))^2(\log \bar{r}_{LS}(\bar{t}))^3}\right)Ste$$

$$\left.\left.- \frac{1}{\log \bar{r}_{LS}(\bar{t})}\right)d\bar{t}\right.$$

(2)

3-2-1-2. $q_2(t)$ for transverse fin

The second pathway for heat transfer into the PCM is through the fin. Since the fin itself is at the melting temperature initially and only heats up over time due to transient thermal diffusion, this is a more complicated problem than $q_1(t)$. In this case, $q_2(t)$ depends on the fin temperature distribution $\theta_f(\bar{r}, \bar{t})$. In addition to axisymmetry, the fin is also assumed to have no thermal

gradient in the axial direction, which is justified by the thin nature of the fin compared to its length. In such a case, as shown in Figure 2(b), energy balance of an infinitesimal element of the fin with width w and radial size dr is considered. In addition to thermal conduction into and out of this element, heat loss to the PCM occurs from the top surface. Using Fourier's law, energy balance for this element can be used to derive a governing partial differential equation for the fin temperature

$$\frac{\bar{c}_f}{\bar{k}_f}\frac{\partial \theta_f}{\partial \bar{t}} = \frac{1}{\bar{r}}\frac{\partial}{\partial \bar{r}}\left(\bar{r}\frac{\partial \theta_f}{\partial \bar{r}}\right) - \bar{S}_r \tag{3}$$

where $\bar{S}_r$ represents heat loss to the surrounding PCM. $\bar{S}_r$ is related to the gradient of the PCM temperature distribution $\theta_p(\bar{r}, \bar{t})$ at the wall. Therefore, $\theta_p(\bar{r}, \bar{t})$ must be determined in order to proceed. Recognizing that the fin temperature itself changes over time, this is a problem of one-dimensional phase change propagation from a wall with time-dependent wall temperature. A solution for this problem is available based on perturbation method [35,36]. The PCM temperature can be written as a power series involving the Stefan number.

$$\theta_p(\bar{r}, \bar{z}, \bar{t}) = \theta_0(\bar{r}, \bar{z}, \bar{t}) + Ste \cdot \theta_1(\bar{r}, \bar{z}, \bar{t}) + (Ste)^2 \cdot \theta_2(\bar{r}, \bar{z}, \bar{t}) \tag{4}$$

where θ_0, θ_1 and θ_2 can be shown to be functions of the fin temperature distribution as follows

$$\theta_0(\bar{r}, \bar{z}, \bar{t}) = \theta_f\left(1 - \frac{\bar{z}}{\bar{z}_{LS}}\right) \tag{5}$$

$$\theta_1(\bar{r}, \bar{z}, \bar{t}) = \frac{1}{6}\theta_f\left(\frac{\bar{z}}{\bar{z}_{LS}}\right)\left(\frac{\bar{z}}{\bar{z}_{LS}} - 1\right)\left[\theta_f\left(\frac{\bar{z}}{\bar{z}_{LS}} + 1\right) - \frac{\theta_f'}{\bar{z}_{LS}'}\bar{z}_{LS}\left(\frac{\bar{z}}{\bar{z}_{LS}} - 2\right)\right] \tag{6}$$

$$\theta_2(\bar{r},\bar{z},\bar{t}) = -\frac{1}{360}\theta_f\left(\frac{\bar{z}}{\bar{z}_{LS}}\right)\left(\frac{\bar{z}}{\bar{z}_{LS}}-1\right)\left[\theta_f{}^2\left(\frac{\bar{z}}{\bar{z}_{LS}}+1\right)\left(9\left(\frac{\bar{z}}{\bar{z}_{LS}}\right)^2+19\right)\right.$$

$$+ 10\left(\frac{\theta_f{}'}{\bar{z}_{LS}'}\right)^2 \bar{z}_{LS}^2\left(\frac{\bar{z}}{\bar{z}_{LS}}+4\right) + 5\theta_f\frac{\theta_f{}'}{\bar{z}_{LS}'}\bar{z}_{LS}\left(3\left(\frac{\bar{z}}{\bar{z}_{LS}}\right)^2+5\left(\frac{\bar{z}}{\bar{z}_{LS}}\right)\right) \tag{7}$$

$$\left.+ 17\right)\Bigg]$$

As a result, an expression for $\bar{S}_r$ in equation (3) can be written as

$$\bar{S}_r = \frac{1}{\overline{k_f w}}\left[\begin{array}{l}\dfrac{\theta_f}{\bar{z}_{LS}} + Ste\,\dfrac{\theta_f\left(\theta_f + 2\dfrac{\theta_f{}'}{\bar{z}_{LS}'}\bar{z}_{LS}\right)}{6\bar{z}_{LS}} - \\[4mm] (Ste)^2\,\dfrac{\theta_f\left(40\left(\dfrac{\theta_f{}'}{\bar{z}_{LS}'}\right)^2\bar{z}_{LS}^2 + 85\theta_f\dfrac{\theta_f{}'}{\bar{z}_{LS}'}\bar{z}_{LS} + 19\theta_f{}^2\right)}{360\bar{z}_{LS}}\end{array}\right] \tag{8}$$

where the location of the melting front originating from the transverse fin surface, $\bar{z}_{LS}$ is given by [35,36]

$$\bar{z}_{LS}(\bar{r},\bar{t}) = \left[2Ste\int_0^{\bar{t}}\theta_f(\bar{r},\bar{\tau})\left(1-\frac{Ste}{3}\theta_f(\bar{r},\bar{\tau})+\frac{7}{45}(Ste)^2\theta_f(\bar{r},\bar{\tau})^2\right)d\bar{\tau}\right]^{\frac{1}{2}} \tag{9}$$

Note the primes in equations (6)-(8) represent derivatives with respect to time. Equations (8) and (9) determine heat loss from a given radial location on transverse fin surface at any given time in terms of the prior fin temperature history at that location and PCM thermal properties.

A complete partial differential equation in $\theta_f(\bar{r},\bar{t})$ can be derived by combining equations (3) and (8) as

$$\frac{\bar{c}_f}{\bar{k}_f}\frac{\partial \theta_f}{\partial \bar{t}} = \frac{1}{\bar{r}}\frac{\partial}{\partial \bar{r}}\left(\bar{r}\frac{\partial \theta_f}{\partial \bar{r}}\right)$$

$$-\frac{1}{\bar{k}_f\bar{w}}\left[\begin{array}{c}\dfrac{\theta_f}{\bar{z}_{LS}} + Ste\,\dfrac{\theta_f\left(\theta_f + 2\dfrac{\theta_f{}'}{\bar{z}_{LS}'}\bar{z}_{LS}\right)}{6\bar{z}_{LS}} - \\[2em] (Ste)^2\,\dfrac{\theta_f\left(40\left(\dfrac{\theta_f{}'}{\bar{z}_{LS}'}\right)^2\bar{z}_{LS}^2 + 85\theta_f\dfrac{\theta_f{}'}{\bar{z}_{LS}'}\bar{z}_{LS} + 19\theta_f{}^2\right)}{360\bar{z}_{LS}}\end{array}\right] \tag{10}$$

Boundary and initial conditions associated with equation (10) must be defined. The fin temperature equals the cylinder wall temperature at fin base, $\bar{r} = 1$. Adiabatic boundary condition applies at fin tip, $\bar{r} = \frac{R_o}{R_i}$. Finally, the fin temperature $\theta_f(\bar{r}, 0)$ is 0 initially. Equations (11)-(13) express these requirements mathematically:

$$\theta_f(1, \bar{t}) = 1 \tag{11}$$

$$\left(\frac{\partial \theta_f}{\partial \bar{r}}\right)_{\bar{r}=\bar{R}_o} = 0 \tag{12}$$

$$\theta_f(\bar{r}, 0) = 0 \tag{13}$$

Equation (10) contains only the fin temperature and is uncoupled from the PCM temperature. In principle, a solution of equation (10) can be used to determine $\bar{q}_2(\bar{t})$, the total heat flux into the PCM from the fin surface as follows

$$\bar{q}_2(\bar{t}) = \frac{2}{\bar{W}} \int_0^{\bar{t}} \int_{\bar{R}_i}^{\bar{R}_o} \left(\frac{\partial \theta_p}{\partial \bar{z}}\right)_{\bar{z}=0} \bar{r}\, d\bar{r}\, d\bar{t}$$

$$= \frac{2}{\bar{W}} \int_0^{\bar{t}} \int_{\bar{R}_i}^{\bar{R}_o} \left[\frac{\theta_f}{\bar{z}_{LS}} + Ste\, \frac{\theta_f\left(\theta_f + 2\frac{\theta_f{}'}{\bar{z}_{LS}'}\bar{z}_{LS}\right)}{6\bar{z}_{LS}} - (Ste)^2\, \frac{\theta_f\left(40\left(\frac{\theta_f{}'}{\bar{z}_{LS}'}\right)^2 \bar{z}_{LS}^2 + 85\theta_f \frac{\theta_f{}'}{\bar{z}_{LS}'}\bar{z}_{LS} + 19\theta_f{}^2\right)}{360\bar{z}_{LS}} \right] \bar{r}\, d\bar{r}\, d\bar{t} \tag{14}$$

However, it is very challenging to solve equation (10) explicitly due to the complicated, non-linear nature of the source term. A time stepping approach for solving equation (10) is discussed in section 2.3.

Heat transfer analysis of a longitudinal fin is discussed next.
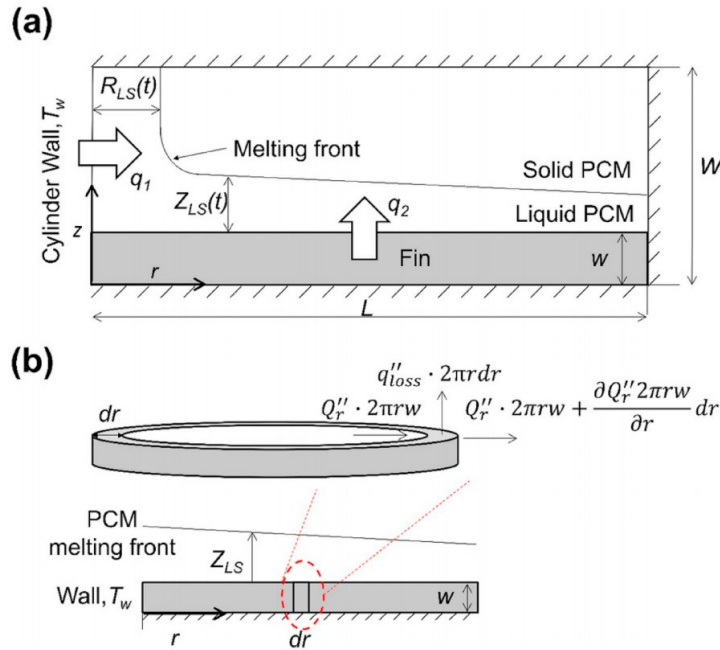
Figure 2. (a) Schematic of two melting fronts within the unit cell for transverse fin thermal analysis; (b) Schematic of an infinitesimal fin element for deriving governing energy conservation equation for temperature distribution in transverse fin

3-2-2. Longitudinal fin

This sub-section considers longitudinal fins that extend through the axial coordinate, but not in the circumferential direction, as shown in the top view in Figure 1(b). The number of fins is assumed to be constant and distributed evenly around the periphery of the cylinder, so that the angle φ_o in Figure 1(b) is fixed. Based on symmetry in the problem, the unit cell in the circumferential direction that can be considered for analysis denoted in Figure 1(b) and shown in detail in Figure 3(a). Similar to the traverse fin analysis, it is assumed that fin temperature distribution is one dimensional, in this case, radial. This is a reasonable assumption when fin width $\varphi_f R_o$ is small compared to the fin length R_o-R_i.

The goal of analysis presented in this section is to determine the effect of fin size φ_f on the total heat absorbed by the PCM in a given time. Similar to the transverse fins considered in section 2.1, there may be a distinct trade-off here between reduced area of direct PCM-cylinder contact and greater thermal conduction into the fin as a result of increasing the fin size. The specific nature of the trade-off, of course, depends on the various non-dimensional parameters that govern the problem, and must be carefully analyzed through modeling.

Similar to the case of transverse fins, the two components of heat transfer into the PCM are evaluated next.

3-2-2-1. $q_1(t)$ for longitudinal fins

Analysis for determining the heat transfer directly from the cylinder to the PCM can be carried out using the one-dimensional Stefan problem with constant wall temperature, similar to the transverse fin case in section 2.1.1, with the only difference being the base area. In this case, $\bar{q}_1(\bar{t})$ is given by:

$$\bar{q}_1(\bar{t}) = \left(\frac{\varphi_f}{\pi} - \frac{1}{N}\right) \int_0^{\bar{t}} \left(\frac{\partial \theta_p}{\partial \bar{r}}\right)_{\bar{r}=\bar{R}_i} d\bar{t}$$

$$= \int_0^{\bar{t}} \left(\frac{\varphi_f}{\pi}\right.$$

$$\left.- \frac{1}{N}\right)\left(\left(\frac{\left(10\left(\bar{r}_{LS}(\bar{t})\right)^4 + 8\left(\bar{r}_{LS}(\bar{t})\right)^2 - 6\right)}{64\left(\bar{r}_{LS}(\bar{t})\right)^4 (\log \bar{r}_{LS}(\bar{t}))^4}\right.$$

$$- \frac{\left(5\left(\bar{r}_{LS}(\bar{t})\right)^2 - 1\right)^2}{16\left(\bar{r}_{LS}(\bar{t})\right)^4 (\log \bar{r}_{LS}(\bar{t}))^7}$$

$$- \frac{\left(56\left(\bar{r}_{LS}(\bar{t})\right)^4 + 24\left(\bar{r}_{LS}(\bar{t})\right)^2 + 44\right)}{128(\bar{r}_{LS}(\bar{t}))^4 (\log \bar{r}_{LS}(\bar{t}))^5} \tag{15}$$

$$\left.+ \frac{\left(\left(\bar{r}_{LS}(\bar{t})\right)^2 - 1\right)\left(71\left(\bar{r}_{LS}(\bar{t})\right)^2 + 71\right)}{128\left(\bar{r}_{LS}(\bar{t})\right)^4 (\log \bar{r}_{LS}(\bar{t}))^6}\right) Ste^2$$

$$+ \left(\frac{\left(\left(\bar{r}_{LS}(\bar{t})\right)^2 - 1\right)}{4\left(\bar{r}_{LS}(\bar{t})\right)^2 (\log \bar{r}_{LS}(\bar{t}))^4} - \frac{\left(\left(\bar{r}_{LS}(\bar{t})\right)^2 + 1\right)}{4\left(\bar{r}_{LS}(\bar{t})\right)^2 (\log \bar{r}_{LS}(\bar{t}))^3}\right) Ste$$

$$\left.- \frac{1}{\log \bar{r}_{LS}(\bar{t})}\right) d\bar{t}$$

Where N is the total number of fins in the circumferential direction. N is assumed to be fixed in this analysis.

3-2-2-2. $q_2(t)$ for longitudinal fins

Analysis for determining the heat transfer into PCM through a longitudinal fin is also similar to the transverse fin case presented in section 2.1.2, but with some key differences. Mainly, the

infinitesimal element to be considered for deriving the partial differential equation for the temperature distribution $\theta_f(\bar{r}, \bar{t})$ is cylindrical instead of Cartesian. Unlike the previous case, this element now subtends in the circumferential direction, as shown in Figure 3(b). Assuming thermal uniformity in the circumferential direction, which is valid as long as $\varphi_f R_o$ is smaller than fin size R_o-R_i, the governing energy conservation equation can be written as

$$\frac{\bar{c}_f}{\bar{k}_f} \frac{\partial \theta_f}{\partial \bar{t}} = \frac{1}{\bar{r}} \frac{\partial}{\partial \bar{r}} (\bar{r} \frac{\partial \theta_f}{\partial \bar{r}}) - \bar{S}_a \tag{16}$$

Where $\bar{S}_a$ accounts for heat loss into the PCM.

Similar to the transverse fin case, $\bar{S}_a$ can be determined by accounting for phase change propagation into the PCM due to time-dependent temperature boundary condition at the fin base. A key difference is the area of contact between the fin element and PCM. Using the temperature solution based on perturbation method, an expression for $\bar{S}_a$ can be derived as

$$\bar{S}_a = \frac{1}{\bar{k}_f \bar{r} \varphi_f} \left[\frac{\theta_f}{\bar{z}_{LS}} + Ste \frac{\theta_f \left(\theta_f + 2\frac{\theta_f'}{\bar{z}_{LS}'} \bar{z}_{LS} \right)}{6\bar{z}_{LS}} - (Ste)^2 \frac{\theta_f \left(40 \left(\frac{\theta_f'}{\bar{z}_{LS}'} \right)^2 \bar{z}_{LS}^2 + 85\theta_f \frac{\theta_f'}{\bar{z}_{LS}'} \bar{z}_{LS} + 19\theta_f^2 \right)}{360\bar{z}_{LS}} \right] \tag{17}$$

This assumes that melting front location $\bar{z}_{LS}$, derived by equation (9) for transverse fins can also be used for longitudinal fins in the circumferential direction. This is a reasonable assumption as long as the fin angle φ_f is small

Combining equations (16) and (17), a partial differential equation for the fin temperature distribution may be derived as

$$\frac{\bar{c}_f}{\bar{k}_f}\frac{\partial \theta_f}{\partial \bar{t}} = \frac{1}{\bar{r}}\frac{\partial}{\partial \bar{r}}\left(\bar{r}\frac{\partial \theta_f}{\partial \bar{r}}\right)$$

$$-\frac{1}{\bar{k}_f \bar{r}\varphi_f}\left[\begin{array}{c} \dfrac{\theta_f}{\bar{z}_{LS}} + Ste\dfrac{\theta_f\left(\theta_f + 2\dfrac{\theta_f{}'}{\bar{z}'_{LS}}\bar{z}_{LS}\right)}{6\bar{z}_{LS}} - \\[4ex] (Ste)^2 \dfrac{\theta_f\left(40\left(\dfrac{\theta_f{}'}{\bar{z}'_{LS}}\right)^2 \bar{z}_{LS}^2 + 85\theta_f\dfrac{\theta_f{}'}{\bar{z}'_{LS}}\bar{z}_{LS} + 19\theta_f{}^2\right)}{360\bar{z}_{LS}} \end{array}\right] \qquad (18)$$

Following the determination of the fin temperature distribution from equation (18), the heat loss into the PCM, $q_2(t)$ can be written as

$$\bar{q}_2(\bar{t}) = \frac{1}{\pi}\int_0^{\bar{t}}\int_{\bar{R}_i}^{\bar{R}_o}\left(\frac{\partial \theta_p}{\partial \bar{z}}\right)_{\bar{z}=0} d\bar{r}d\bar{t}$$

$$= \frac{1}{\pi}\int_0^{\bar{t}}\int_{\bar{R}_i}^{\bar{R}_o}\left[\begin{array}{c} \dfrac{\theta_f}{\bar{z}_{LS}} + Ste\dfrac{\theta_f\left(\theta_f + 2\dfrac{\theta_f{}'}{\bar{z}'_{LS}}\bar{z}_{LS}\right)}{6\bar{z}_{LS}} - \\[4ex] (Ste)^2 \dfrac{\theta_f\left(40\left(\dfrac{\theta_f{}'}{\bar{z}'_{LS}}\right)^2 \bar{z}_{LS}^2 + 85\theta_f\dfrac{\theta_f{}'}{\bar{z}'_{LS}}\bar{z}_{LS} + 19\theta_f{}^2\right)}{360\bar{z}_{LS}} \end{array}\right] d\bar{r}d\bar{t} \qquad (19)$$

This completes the derivation of the two components of heat transfer into the PCM for the longitudinal fin.

Calculation of total heat transfer into the PCM requires determination of the fin temperature distribution by solving the governing energy equation, which in both cases discussed above, are complicated partial differential equations. Since an analytical solution for these equations is

unlikely, a timestepping approach for evaluating the temperature distribution is discussed in the next section.
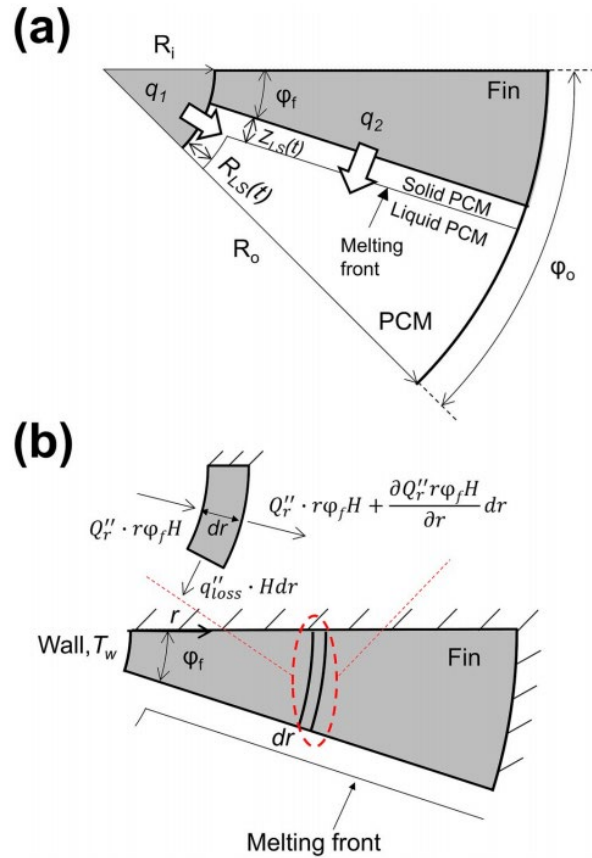
Figure 3. (a) Schematic of two melting fronts within the unit cell for transverse fin thermal analysis; (b) Schematic of an infinitesimal fin element for deriving governing energy conservation equation for temperature distribution in transverse fin

3-2-3. Timestepping approach for determining fin temperature distribution

While difficult to solve exactly equations (10) and (18) are quite amenable to numerical computation based timestepping. A key challenge, similar to Cartesian fins [28], is the singularity at $\bar{t}=0$ in the source terms, which results in difficulties in the initial timestepping. An approximation is made in order to overcome this challenge. Heat transfer into the fin from $\bar{t}=0$ up to a small time $\bar{t}^*$ is assumed to occur without heat loss into the PCM. This may be a reasonable

approximation for small values of $\bar{t}^*$, up to which, the propagation of phase change front, and hence the area of contact between the fin and PCM is small. This is a helpful approximation because neglecting heat loss to the PCM in equations (10) and (18) reduces these to standard thermal conduction problems, which can be solved to provide temperature distribution in the fin at $\bar{t}=\bar{t}^*$. Following this, the timestepping approach, including the effect of heat loss to the PCM can be carried out, because there is no singularity in the governing equation for $\bar{t}>0$. The value of $\bar{t}^*$ clearly needs to be chosen to be small enough to minimize the error involved in neglecting heat transfer to the PCM up to $\bar{t}=\bar{t}^*$.

Based on the assumption of neglecting heat transfer into the PCM, analytical expressions for fin temperature distribution at $\bar{t}=\bar{t}^*$ can be determined by using the method of separation of variables. For both transverse and longitudinal fins, the result is

$$\theta_f^*(\bar{r},\bar{t}^*) = 1 - 2\sum_{n=1}^{\infty} \exp\left(-\frac{\beta_n^2}{\bar{R}_o^2}\bar{t}^*\right) \frac{Y_1(\beta_n)J_0\left(\beta_n\frac{\bar{r}}{\bar{R}_o}\right) - J_1(\beta_n)Y_0\left(\beta_n\frac{\bar{r}}{\bar{R}_o}\right)}{C_n} \qquad (20)$$

where

$$C_n = \beta_n\left[\left(Y_0(\beta_n)J_0\left(\frac{\beta_n}{\bar{R}_o}\right) - J_0(\beta_n)Y_0\left(\frac{\beta_n}{\bar{R}_o}\right)\right) \right.$$
$$\left. -\frac{1}{\bar{R}_o}\left(Y_1(\beta_n)J_1\left(\frac{\beta_n}{\bar{R}_o}\right) - J_1(\beta_n)Y_1\left(\frac{\beta_n}{\bar{R}_o}\right)\right)\right] \qquad (21)$$

and β_n are roots of the transcendental equation

$$Y_1(x)J_0\left(\frac{x}{\bar{R}_o}\right) - J_1(x)Y_0\left(\frac{x}{\bar{R}_o}\right) = 0 \qquad (22)$$

3-3. Results and discussion

3-3-1. Model validation

Comparison with finite element simulation is first carried out in ANSYS-CFX to validate the analytical models presented in section 2. In this case, the system presented in Figure 2(a) is considered with aluminum transverse fin and octadecane PCM. Melting point, density, heat capacity, thermal conductivity and latent heat of the PCM are taken to be 28 °C, 780 kg/m^3, 2300 J/kgK, 0.15 W/mK and 244000 J/kg, respectively, corresponding to properties of octadecane, a commonly used PCM [37]. Standard thermal properties are assumed for aluminum. Temperature of the inner wall is maintained at 20 K above the phase change temperature of the PCM.

The finite-element simulation determines the fin and PCM temperature distributions as well as the phase change propagation using the enthalpy method, where the PCM is defined as a homogenous binary mixture of solid and liquid phases. The PCM is assumed to initially be completely solid. The quadrilateral/triangular mesh in the simulation is swept in circumferential and axial directions for transverse and longitudinal fin configurations respectively. Grid independence analysis is carried out to show that variation in predicted temperature is negligible beyond 232128 and 696384 nodes in the fin and PCM, respectively.

Figure 4(a) shows a comparison of predicted fin temperature distribution between the model presented in section 2.1 and the finite element simulation at multiples times. In addition, comparison of the phase change interface location computed with analytical model and the finite element simulation is shown in figure 4(b). There is good agreement between the analytical model and finite element simulation for both temperature distribution and phase change interface. The worst-case deviation between the analytical model and finite-element simulation is 1.2% and 3.5% for data shown in Figures 4(a) and 4(b), respectively. Note that in this case, a small value of $\bar{t}^* =$

2.09×10^{-4}, equivalent to 0.05% of the total time is used. A small value of $\bar{t}^*$ is needed to minimize error due to the initial approximation.
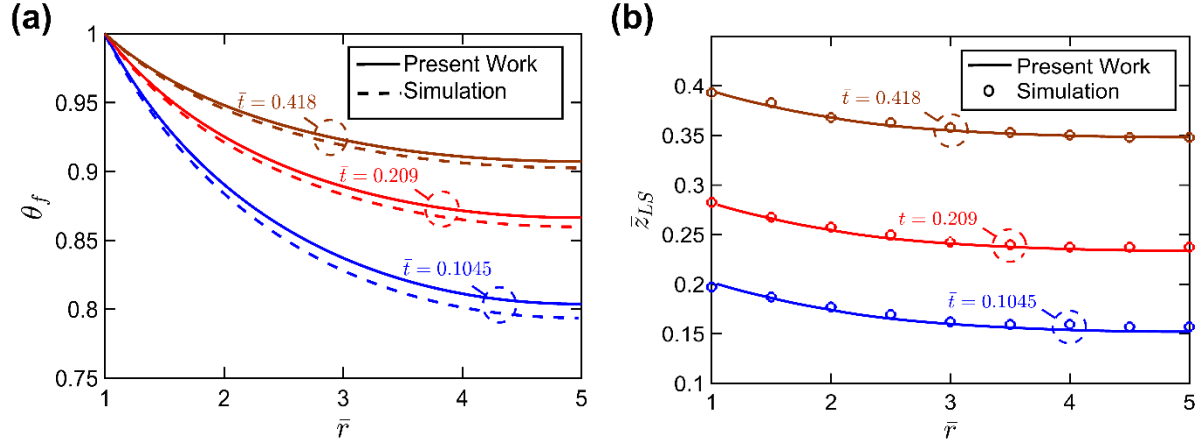
Figure 4. Validation of theoretical models by comparison with finite-element simulations: (a) Temperature distribution and (b) phase change front location at multiple times for a transverse fin with $\bar{W}$=2, $\bar{w}$=0.5, $\bar{L}$=4, Ste=0.19, $\bar{k}_f$=1580, $\bar{c}_f$=1.36.

In addition, the analytical model presented in this work is also compared with experimental data reported by Sasaguchi, *et al.* [38]. Figure 5 plots non-dimensional heat flux as a function of time and compares the analytical model and past experimental data for solidification of n-Eicosane contained in an annular region around a cold inner cylinder wall with four longitudinal fins. Figure 5 carries out this comparison for two different wall temperatures for which Sasguchi, et al. [38] reported measurements. Thermal properties of the PCM and fin are taken from the past work [38]. Non-dimensionalization is carried out similar to other results in the present work. Figure 5 good agreement between the present analytical model and the past experimental work for both cases, thereby providing additional validation of the present work. Please note that the present work ignores convective heat transfer effects and assumes constant thermal properties, which may contribute to the small disagreement between modeling and measurements. Further, the fins used

by Sasaguchi, *et al.* appear to have constant width, whereas the fins in the present work are longitudinal, which may also be a source of disagreement between the two.
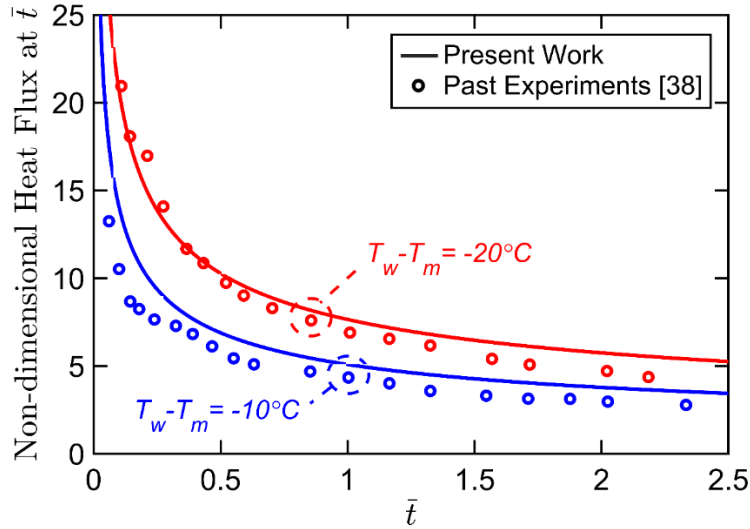
Figure 5. Validation of the analytical model by comparison of predicted heat flux as a function of time with past experimental measurements [38] for solidification of n-Eicosane with four fins around a cold, 45 mm diameter cylinder for two different wall temperatures.

3-3-2. Effect of fin size on heat stored

Total heat transfer into the PCM in a transverse finned system, $\bar{q}_t$, along with its two components $\bar{q}_1$ and $\bar{q}_2$ are shown in Figures 6(a)-(f) as a function of $\overline{w}/\overline{W}$ for six different values of fin thermal conductivity $\bar{k}_f$. The total time is $\bar{t} = 0.418$. $\bar{q}_1$ and $\bar{q}_2$ are calculated by equations (2) and (14), respectively. For comparison, the total heat stored in the absence of fins is 4.98 in non-dimensional form. Figure 6 shows that as $\overline{w}/\overline{W}$ increases, heat transfer from fin surface into the PCM, $\bar{q}_2$, improves due to greater thermal diffusion into the fin. As a result, $\bar{q}_2$ increases sharply with $\frac{\overline{w}}{\overline{W}}$ for small values of $\frac{\overline{w}}{\overline{W}}$, but saturates at larger values. On the other hand, a higher value of $\overline{w}/\overline{W}$ results in lower area of direct contact between the wall and the PCM. This contributes to reduced heat transfer from the wall into the PCM, $\bar{q}_1$, as seen in Figures 6(a)-(f). For

any given fin thermal conductivity, total heat absorbed by the PCM, given by the sum of $\bar{q}_1$ and $\bar{q}_2$, does not change considerably with fin thickness beyond a certain value of $\bar{w}/\overline{W}$. As a result, there is no thermal benefit in increasing the fin thickness beyond a minimum value. This clearly advocates for placing thin transverse fins.
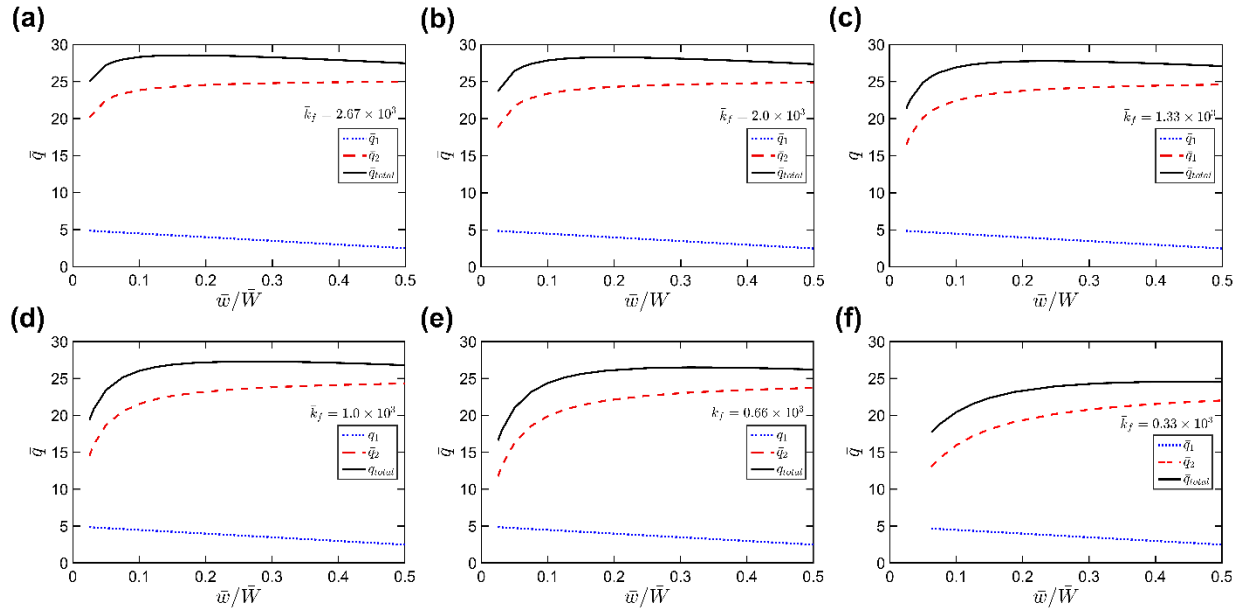
Figure 6. Heat absorbed by the PCM up to $\bar{t}=0.418$ as a function of fin size $\dfrac{\bar{w}}{\overline{W}}$ for six different fin thermal conductivities in transverse configuration with $\overline{W}=2$, $\overline{L}=4$, Ste=0.19, $\bar{c}_f=1.36$. Both components of heat absorbed are shown.

Figure 7(a) plots the total heat stored for all thermal conductivities on the same plot, and clearly shows, as expected, that the higher the fin thermal conductivity, the larger is the total heat absorbed in the PCM. Due to the saturation effect of $\bar{w}/\overline{W}$ on total heat stored, it is useful to define $(\bar{w}/\overline{W})_{min}$ as the value of $\bar{w}/\overline{W}$ that results in 98% of the maximum possible total heat stored. From a practical perspective, this may be viewed as the recommended fin size, beyond which, there is little additional thermal benefit. The dependence of $(\bar{w}/\overline{W})_{min}$ on fin thermal conductivity is shown in Figure 7(b). This Figure shows a shift in the location of $(\bar{w}/\overline{W})_{min}$

towards lower values when thermal conductivity of the fin increases. This occurs because, as the fin thermal conductivity increases, the fin thermal resistance decreases, and therefore, fin temperature saturates at lower $(\bar{w}/\bar{W})_{min}$ values. Figure 7(b) shows that improving fin thermal conductivity reduces the need for thick fin, but this effect does saturate quickly at high values of fin thermal conductivity. It is very important in practical fin design to consider the relationship between the peak stored energy, fin thermal conductivity and fin size, since selecting a thicker fin does not increase total stored energy.
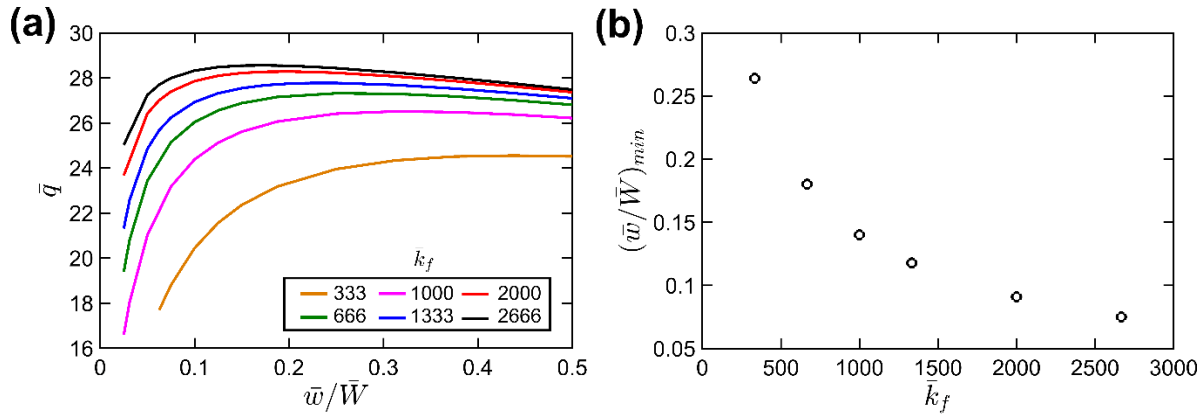
Figure 7. (a) Plot of $\bar{q}_{total}$ up to $\bar{t}$=0.418 as a function of fin size $\dfrac{\bar{w}}{\bar{W}}$ for different values of fin thermal conductivity for the case of transverse fin with $\bar{W}$=2, $\bar{L}$=4, Ste=0.19 ,$\bar{c}_f$=1.36; (b) Minimum value of $\dfrac{\bar{w}}{\bar{W}}$ needed to reach within 98% of the best possible heat absorbed, as a function of fin thermal conductivity.

Similar results for longitudinal fins are shown in Figure 8. In the case of four equally distributed longitudinal fins, the total heat absorbed by the PCM does not change significantly with fin thickness φ_f. The heat transferred from fin to PCM, $\bar{q}_2$ remains nearly constant with φ_f, whereas $\bar{q}_1$ decreases linearly with φ_f as contact area between inner cylinder and the PCM decreases when fin size increases. This shows that even a very thin fin sufficiently promotes heat transfer. Therefore, fin insertion is important, but changes in fin size do not significantly affect thermal

performance. Figure 9 presents the dependence of total heat absorbed by the PCM on fin thickness for different longitudinal fin thermal conductivity values. This dependence is seen to be weaker than the transverse fin case.
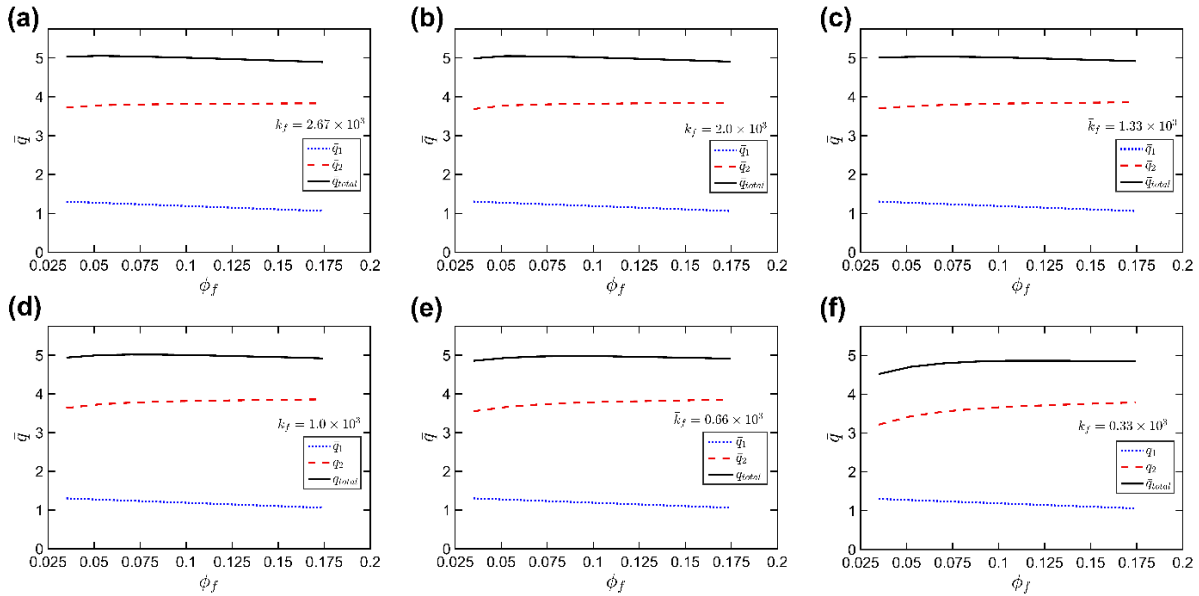
Figure 8. Heat absorbed by the PCM up to $\bar{t}=1.6722$ as a function of fin size φf for six different fin thermal conductivities in longitudinal configuration with φo= 0.7854, $\bar{L}=3$, Ste=0.19, $\bar{c}_f=1.36$. Both components of heat absorbed are shown.
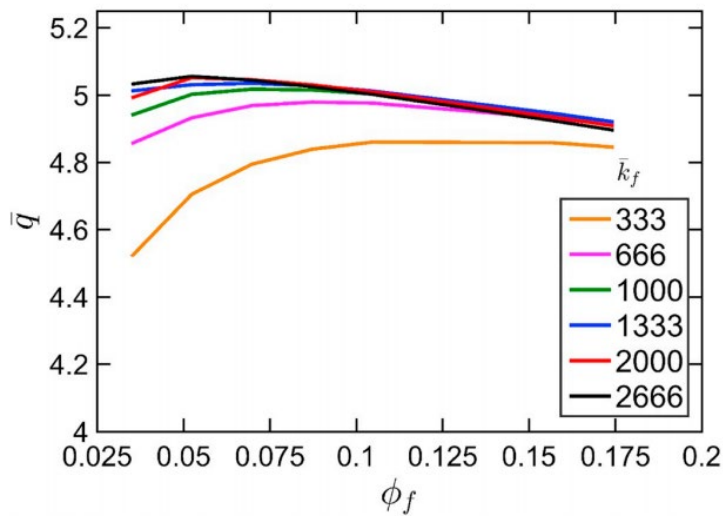
Figure 9. Plot of $\bar{q}_{total}$ at $\bar{t}=1.6722$ as a function of fin size φf for different values of fin thermal conductivity for the case of longitudinal fin with φo= 0.7854, $\bar{L}=3$, Ste=0.19, $\bar{c}_f=1.36$.

While the total energy stored for the case of Cartesian fins has been shown to be highly dependent on fin size [28], Figures (6)-(9) show that the same is not the case for transverse or longitudinal fins. Nevertheless, fin insertion is still a very effective mechanism for increasing energy storage capability of cylindrical systems. Even with a thin fin, energy stored is much higher than no fin at all. However, choosing large-sized fins does not necessarily improve thermal performance. Inserting large fins may also not be attractive from the perspective of system weight and cost.

Typically fins are high thermal conductivity materials with $\bar{k}_f$ in the range of 333 up to 2666, with octadecane as the PCM. This work shows that in a system with transverse fins, the optimal fin size is almost independent of fin thermal conductivity for conductivities beyond 1500, as seen in Figure 7(b). On the other hand, the optimal fin size depends strongly on fin thermal conductivity in the lower range of thermal conductivity. On the other hand, the maximum stored thermal energy in a system with longitudinal fins is not a strong function of fin size.

3-3-3. Effect of time available for heat transfer

Total time available for heat transfer in the system is a very important factor in determining effectiveness of the fin geometry. Clearly, the entire PCM will reach the wall temperature in the unlikely case of infinite time being available for heat transfer. In such a case, fin insertion is clearly counterproductive, since the presence of fins only reduces PCM volume, and consequently the total amount of energy stored. For most practical applications, where only a finite time is available, inserting fins is indeed beneficial. Figure 10 presents variation in $(\bar{w}/\bar{W})_{min}$ with total heat transfer time for transverse fins. A similar trend has been reported for Cartesian fins [28]. Clearly, the larger the available time, the smaller is the fin thickness needed for heat transfer enhancement.

As time passes, the role of the fin in providing extended surface and additional heat transfer pathway shrinks, and therefore, a larger fin becomes less and less attractive.
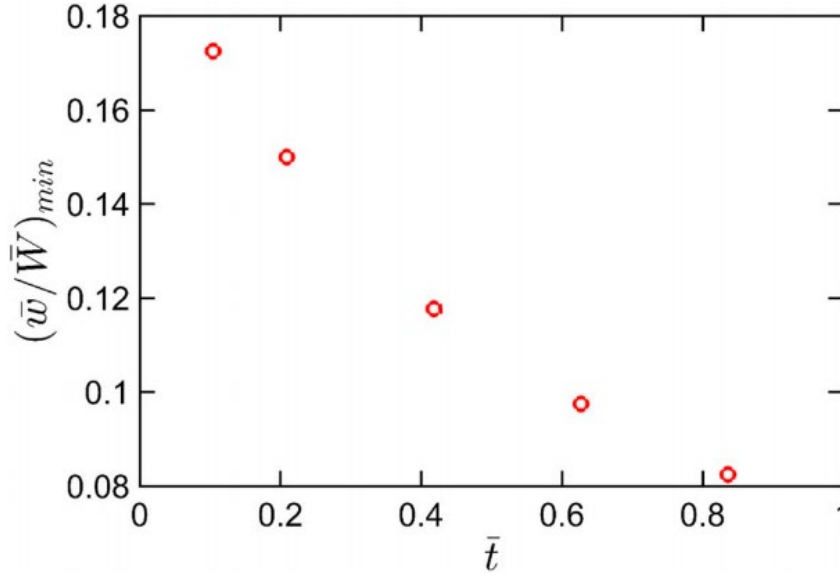
Figure 10. Effect of total time available for heat transfer on the minimum fin thickness to reach within 98% of maximum possible heat stored for a transverse fin configuration, with $\bar{W}$=2, $\bar{L}$=4, Ste=0.19, $\bar{k}_f$=1333, $\bar{c}_f$=1.36.

3-3-4. Effect of $\bar{t}^*$

As discussed in section 2.3, an approximation is used to initiate the time stepping process due to the singularity in equations (10) and (18) at $\bar{t}$=0. This approximation ignores heat transfer into the PCM from the fin up to a short time $\bar{t}^*$. Clearly, the error introduced by this approximation must be understood, and a maximum tolerable value of $\bar{t}^*$ must be determined for a given acceptable error. Figures 11(a) and 11(b) present fin temperature distribution for transverse and longitudinal configurations at $\bar{t}$=0.209 and $\bar{t}$=0.8361 respectively for multiple values of $\bar{t}^*$. For comparison, finite element simulation results are also presented. These Figures show that in both

cases, the approximation error reduces as $\bar{t}^*$ decreases. These plots establish the maximum value of $\bar{t}^*$ for a given error level for a specific set of parameters.

A key assumption underlying the analysis presented here is that the two phase change fronts develop independent of each other, for both transverse and longitudinal fins. This assumption enables the independent determination of q_1 and q_2. In order to verify the validity of this assumption, fin and PCM temperature distributions are computed using finite-element simulations for both transverse and longitudinal fins. Temperature distributions for the two cases are shown in Figures 12(a) and 12(b), respectively, at multiple times. Heat diffusion from inner cylindrical wall into the PCM, q_1, and heat diffusion from fin surface into the PCM, q_2, can be seen in the form of two independent phase change propagation fronts in these figures. Except for a small region close to the fin-wall interface, the two fronts do not interact much with each other. This justifies a key assumption behind the analysis in Section 2 that independently accounted for the contributions of the two fronts towards total energy stored.
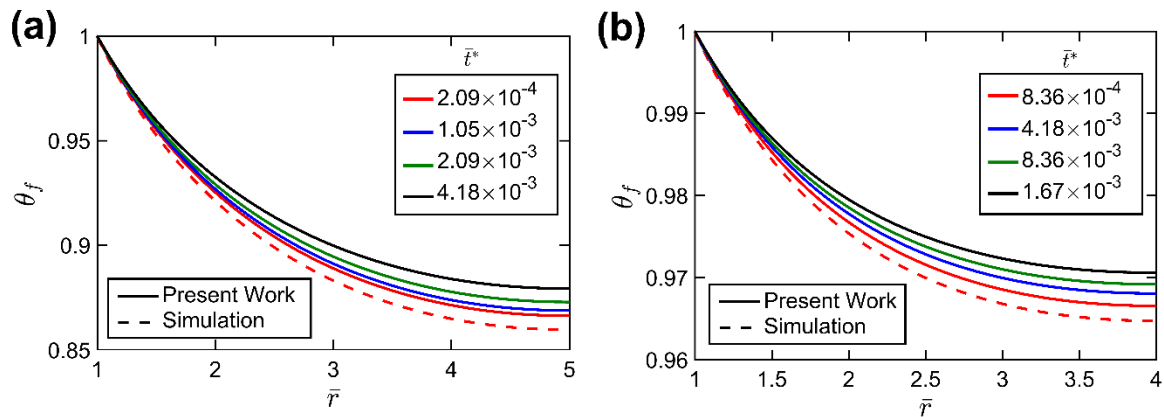
Figure 11. Effect of $\bar{t}^*$ on the accuracy of computed temperature distribution for case of (a) transverse fin at $\bar{t}=0.209$ and $\bar{W}=2$, $\bar{w}=0.5$, $\bar{L}=4$, Ste=0.19, $\bar{k}_f=1580$, $\bar{c}_f=1.36$ (b) longitudinal fin at $\bar{t}=0.8361$ and $\varphi_o=0.7854$, $\bar{L}=3$, Ste=0.19, $\bar{c}_f=1.36$. Results from finite-element simulation are also shown for comparison.

3-4. Conclusions

Results show that for both transverse and longitudinal fins, presence of fins increases thermal energy stored in the PCM significantly for a given time. However, in contrast with Cartesian fins, the amount of stored energy is not a strong function of fin size. This implies that even a very small fin provides considerable heat transfer enhancement and larger fins only diminishing returns.

The highly non-linear and transient nature of heat transfer in phase change energy storage systems presents formidable difficulties in theoretical analysis. This work presents a semi-analytical approach for solving this problem for transverse and longitudinal fins that are commonly used for heat transfer enhancement. Results show key similarities and differences between cylindrical fins and Cartesian fins studied in the recent past. A key conclusion of the present work is that in general, even a thin fin provides excellent heat transfer enhancement, and that larger fins offer diminishing returns. The underlying physics behind this process includes two conflicting effects of fin thickness on heat transfer components to the PCM, one indirectly through the fin and the other directly from the inner tube in contact with PCM were evaluated. The theoretical results presented here have several important practical applications. By quantifying the impact of fin geometry on heat transfer enhancement, the results presented here may help in geometrical optimization of phase change energy storage systems. The insights that even a small-sized fin results in significant benefit and that further increasing the fin size results in very little incremental benefit are both helpful for practical designers. The impact of available time window for heat transfer on the fin size is also an important consideration in practical designs.

3-5. Nomenclature

c volumetric heat capacity (J/m³K)

$\bar{c}_f$ non-dimensional fin volumetric heat capacity, $\bar{c}_f = \frac{c_f}{c_p}$

H Length of cylindrical wall (m)

k thermal conductivity (W/mK)

$\bar{k}_f$ non-dimensional fin thermal conductivity, $\bar{k}_f = \frac{k_f}{k_p}$

L fin length (m)

L_p volumetric latent heat of fusion (J/ m³)

N fin number

q heat absorbed per unit length (J/m)

$\bar{q}$ non-dimensional heat absorbed, $\bar{q} = \frac{q}{(T_w - T_m)c_p R_i^2}$

q''_{loss} heat flux from fin into PCM (W/m²)

Q'' thermal conduction heat flux (W/m²)

$\bar{S}_a$ non-dimensional source term, $\bar{S}_a = \frac{q''_{loss} R_i}{\varphi_f \bar{r}(T_w - T_m)k_f}$

$\bar{S}_r$ non-dimensional source term, $\bar{S}_r = \frac{q''_{loss} R_i}{\bar{w}(T_w - T_m)k_f}$

Ste Stefan number, $Ste = \frac{c_p(T_w - T_m)}{L_p}$

t time (s)

$\bar{t}$ non-dimensional time, $\bar{t} = \frac{\alpha_p t}{R_i^2}$

T temperature (K)

T_m phase change temperature (K)

T_w wall temperature (K)

r spatial coordinate (m)

$\bar{r}$ non-dimensional spatial coordinates, $\bar{r} = \dfrac{r}{R_i}$

R_i inner radius (m)

R_o outer radius (m)

w fin width (m)

W width of the domain (m)

$\bar{w}, \bar{W}$ non-dimensional fin and domain width, $\bar{w} = \dfrac{w}{R_i}, \bar{W} = \dfrac{W}{R_i}$

z spatial coordinates (m)

$\bar{z}$ non-dimensional spatial coordinates, $\bar{z} = \dfrac{z}{R_i}$

Greek symbols

α thermal diffusivity (m^2/s)

$\bar{\alpha}_f$ non-dimensional fin thermal diffusivity, $\bar{\alpha}_f = \dfrac{\alpha_f}{\alpha_p}$

β_n non-dimensional eigenvalues

θ non-dimensional temperature, $\theta = \dfrac{T - T_m}{T_W - T_m}$

φ angular coordinate (rad)

Subscripts and superscripts

f fin

LS liquid solid interface

p phase change material

W   wall

*   initial approximation

3-6. References

[1] U. Desideri, P.E. Campana, Analysis and comparison between a concentrating solar and a photovoltaic power plant, Applied Energy. 113 (2014) 422–433. doi:10.1016/j.apenergy.2013.07.046.

[2] U. Pelay, L. Luo, Y. Fan, D. Stitou, M. Rood, Thermal energy storage systems for concentrated solar power plants, Renewable and Sustainable Energy Reviews. 79 (2017) 82–100. doi:10.1016/j.rser.2017.03.139.

[3] A. Sharma, V. Tyagi, C. Chen, D. Buddhi, Review on thermal energy storage with phase change materials and applications, Renewable and Sustainable Energy Reviews. 13 (2009) 318–345. doi:10.1016/j.rser.2007.10.005.

[4] W.R. Humphries, E.I. Griggs, A design handbook for phase change thermal control and energy storage devices, National Aeronautics and Space Administration, Scientific and Technical Information Office, Washington, 1977. NASA Technical Paper 1074.

[5] K.E. N'Tsoukpoe, H. Liu, N.L. Pierrès, L. Luo, A review on long-term sorption solar energy storage, Renewable and Sustainable Energy Reviews. 13 (2009) 2385–2396. doi:10.1016/j.rser.2009.05.008.

[6] J.M. Mahdi, S. Lohrasbi, E.C. Nsofor, Hybrid heat transfer enhancement for latent-heat thermal energy storage systems: A review, International Journal of Heat and Mass Transfer. 137 (2019) 630–649. doi:10.1016/j.ijheatmasstransfer.2019.03.111.

[7] Y. Tao, Y.-L. He, A review of phase change material and performance enhancement method for latent heat storage system, Renewable and Sustainable Energy Reviews. 93 (2018) 245–259. doi:10.1016/j.rser.2018.05.028.

[8] N.I. Ibrahim, F.A. Al-Sulaiman, S. Rahman, B.S. Yilbas, A.Z. Sahin, Heat transfer enhancement of phase change materials for thermal energy storage applications: A critical review, Renewable and Sustainable Energy Reviews. 74 (2017) 26–50. doi:10.1016/j.rser.2017.01.169.

[9] C. Ho, J. Gao, Preparation and thermophysical properties of nanoparticle-in-paraffin emulsion as phase change material, International Communications in Heat and Mass Transfer. 36 (2009) 467–470. doi:10.1016/j.icheatmasstransfer.2009.01.015.

[10] S.C. Lin, H.H. Al-Kayiem, Evaluation of copper nanoparticles – Paraffin wax compositions for solar thermal energy storage, Solar Energy. 132 (2016) 267–278. doi:10.1016/j.solener.2016.03.004.

[11] K. Lafdi, O. Mesalhy, S. Shaikh, Experimental study on the influence of foam porosity and pore size on the melting of phase change materials, Journal of Applied Physics. 102 (2007) 083549. doi:10.1063/1.2802183.

[12] D. Li, C. Yang, H. Yang, Experimental and numerical study of a tube-fin cool storage heat exchanger, Applied Thermal Engineering. 149 (2019) 712–722. doi:10.1016/j.applthermaleng.2018.12.024.

[13] R. Velraj, R. Seeniraj, B. Hafner, C. Faber, K. Schwarzer, Experimental analysis and numerical modelling of inward solidification on a finned vertical tube for a latent heat storage unit, Solar Energy. 60 (1997) 281–290. doi:10.1016/s0038-092x(96)00167-3.

[14] K. Ismail, Henríquez J.r., L. Moura, M. Ganzarolli, Ice formation around isothermal radial finned tubes, Energy Conversion and Management. 41 (2000) 585–605. doi:10.1016/s0196-8904(99)00128-4.

[15] K. Ismail, C. Alves, M. Modesto, Numerical and experimental study on the solidification of PCM around a vertical axially finned isothermal cylinder, Applied Thermal Engineering. 21 (2001) 53–77. doi:10.1016/s1359-4311(00)00002-8.

[16] W. Ogoh, D. Groulx, Effects of the number and distribution of fins on the storage characteristics of a cylindrical latent heat energy storage system: a numerical study, Heat and Mass Transfer. 48 (2012) 1825–1835. doi:10.1007/s00231-012-1029-3.

[17] C. Liu, D. Groulx, Experimental study of the phase change heat transfer inside a horizontal cylindrical latent heat energy storage system, International Journal of Thermal Sciences. 82 (2014) 100–110. doi:10.1016/j.ijthermalsci.2014.03.014.

[18] R.E. Murray, D. Groulx, Experimental study of the phase change and energy characteristics inside a cylindrical latent heat energy storage system: Part 1 consecutive charging and discharging, Renewable Energy. 62 (2014) 571–581. doi:10.1016/j.renene.2013.08.007.

[19] M. Kabbara, D. Groulx, A. Joseph, Experimental investigations of a latent heat energy storage unit using finned tubes, Applied Thermal Engineering. 101 (2016) 601–611. doi:10.1016/j.applthermaleng.2015.12.080.

[20] Y. Kozak, T. Rozenfeld, G. Ziskind, Close-contact melting in vertical annular enclosures with a non-isothermal base: Theoretical modeling and application to thermal storage, International Journal of Heat and Mass Transfer. 72 (2014) 114–127. doi:10.1016/j.ijheatmasstransfer.2013.12.058.

[21] T. Rozenfeld, Y. Kozak, R. Hayat, G. Ziskind, Close-contact melting in a horizontal cylindrical enclosure with longitudinal plate fins: Demonstration, modeling and application to thermal storage, International Journal of Heat and Mass Transfer. 86 (2015) 465–477. doi:10.1016/j.ijheatmasstransfer.2015.02.064.

[22] A. Rozenfeld, Y. Kozak, T. Rozenfeld, G. Ziskind, Experimental demonstration, modeling and analysis of a novel latent-heat thermal energy storage unit with a helical fin, International Journal of Heat and Mass Transfer. 110 (2017) 692–709. doi:10.1016/j.ijheatmasstransfer.2017.03.020.

[23] A. Erek, Z. Ilken, M.A. Acar, Experimental and numerical investigation of thermal energy storage with a finned tube, International Journal of Energy Research. 29 (2005) 283–301. doi:10.1002/er.1057.

[24] W.-W. Wang, L.-B. Wang, Y.-L. He, Parameter effect of a phase change thermal energy storage unit with one shell and one finned tube on its energy efficiency ratio and heat storage rate, Applied Thermal Engineering. 93 (2016) 50–60. doi:10.1016/j.applthermaleng.2015.08.108.

[25] A.A. Al-Abidi, S. Mat, K. Sopian, M. Sulaiman, A.T. Mohammad, Internal and external fin heat transfer enhancement technique for latent heat thermal energy storage in triplex tube heat exchangers, Applied Thermal Engineering. 53 (2013) 147–156. doi:10.1016/j.applthermaleng.2013.01.011.

[26] A.A. Al-Abidi, S. Mat, K. Sopian, M. Sulaiman, A.T. Mohammad, Numerical study of PCM solidification in a triplex tube heat exchanger with internal and external fins, International Journal of Heat and Mass Transfer. 61 (2013) 684–695. doi:10.1016/j.ijheatmasstransfer.2013.02.030.

[27] Z. Liu, X. Sun, C. Ma, Experimental investigations on the characteristics of melting processes of stearic acid in an annulus and its thermal conductivity enhancement by fins, Energy Conversion and Management. 46 (2005) 959–969. doi:10.1016/j.enconman.2004.05.012.

[28] A. Mostafavi, M. Parhizi, A. Jain, Theoretical modeling and optimization of fin-based enhancement of heat transfer into a phase change material, Int. J. Heat Mass Transfer International Journal of Heat and Mass Transfer. 145 (2019) 118698:1-10. doi: 10.1016/j.ijheatmasstransfer.2019.118698

[29] P. Lamberg, K. Sirén, Approximate analytical model for solidification in a finite PCM storage with internal fins, Applied Mathematical Modelling. 27 (2003) 491–513. doi:10.1016/s0307-904x(03)00080-5.

[30] P. Lamberg, Approximate analytical model for two-phase solidification problem in a finned phase-change material storage, Applied Energy. 77 (2004) 131–152. doi:10.1016/s0306-2619(03)00106-5.

[31] P. Lamberg, K. Sirén, Analytical model for melting in a semi-infinite PCM storage with an internal fin, Heat and Mass Transfer. 39 (2003) 167–176. doi:10.1007/s00231-002-0291-1.

[32] V. Shatikian, G. Ziskind, R. Letan, Numerical investigation of a PCM-based heat sink with internal fins, International Journal of Heat and Mass Transfer. 48 (2005) 3689–3706. doi:10.1016/j.ijheatmasstransfer.2004.10.042.

[33] K.A. Rathjen, L.M. Jiji, Heat Conduction With Melting or Freezing in a Corner, Journal of Heat Transfer. 93 (1971) 101. doi:10.1115/1.3449740.

[34] M. Parhizi, A. Jain, 'The impact of thermal properties on performance of phase change based energy storage systems,' *Appl. Therm. Eng.*, 162 (2019) 114154:1-10. doi: 10.1016/j.applthermaleng.2019.114154.

[35] J. Caldwell, Y. Kwan, On the perturbation method for the Stefan problem with time-dependent boundary conditions, International Journal of Heat and Mass Transfer. 46 (2003) 1497–1501. doi:10.1016/s0017-9310(02)00415-5.

[36] G. Lock, J. Gunderson, D. Quon, J. Donnelly, A study of one-dimensional ice formation with particular reference to periodic growth and decay, International Journal of Heat and Mass Transfer. 12 (1969) 1343–1352. doi:10.1016/0017-9310(69)90021-0.

[37] N.R. Jankowski, F.P. McCluskey, A review of phase change materials for vehicle component thermal buffering, Applied Energy. 113 (2014) 1525–1561. doi:10.1016/j.apenergy.2013.08.026.

[38] K. Sasaguchi, H. Imura, H. Furusho, Heat transfer characteristics of a latent heat storage unit with a finned tube (Experimental studies on solidification and melting processes), Bulletin of JSME, 29 (1986) 2978-2985.

Chapter 4

Unsteady convective heat transfer from a flat plate with heat flux that varies in space and time

4-1. Introduction

Heat transfer between a flat plate and fluid flow is a classical problem in convective heat transfer [1-3], with applications in a wide variety of engineering applications. As the fluid flows past the plate, hydrodynamic and thermal boundary layers develop, across which, momentum and thermal transport occurs. Analytical solutions of several such problems are available in textbooks [1-3] and in the research literature. Despite its classical, long-standing nature, external convective heat transfer in flat plate boundary layers continues to be a research topic of current interest [4,5].

Several simplifying assumptions are often made in order to solve the underlying momentum and energy conservation equations, including steady state, uniform freestream velocity and temperature, laminar, incompressible flow, and uniform plate temperature or heat flux [1]. Two distinct approaches have been used for analytically solving such problems. In the differential approach, the underlying momentum and energy conservation equations, written in differential form are solved in order to determine the velocity and temperature distributions [1]. Self-similar solutions are often sought for these equations [2], although this approach works only for the simplest problems, such as a flat plate with constant temperature. In most other problems, one must rely on numerical computation using finite-volume or similar methods. On the other hand, integral approaches [1] seek a solution that satisfies the energy equation integrated over the boundary layer, which results in some error, but also, considerable simplification. In the Karman-Pohlhausen integral approach [1], polynomial forms of velocity and temperature profiles in the boundary layers are written in order to satisfy various boundary conditions at the wall and edge of the boundary layer. These polynomials are then used in the integral energy balance equation to solve the problem. The assumption of polynomial forms for velocity and temperature profiles is an approximation, but has been justified because parameters governing plate-flow interactions

such as the Nusselt number depend only on processes near the wall and are relatively unaffected by the velocity/temperature distribution in the remainder of the boundary layer [1,6,7]. Polynomial expressions up to the fourth order have been used in the past [6,7].

While flow past a flat plate at a constant temperature or flux are amongst the simplest problems in external convective heat transfer, analytical solutions for several other, more complicated problems have also been reported. For example, spatial variation in plate temperature or heat flux has been accounted for using superimposition or Duhamel's theorem [8]. The Karman-Pohlhausen approach has also been used for solving this problem [6]. The steady-state problem with a specific heat flux profile has been solved using a differential approach [9]. While this results in an exact solution, it is valid only for the specific flux profile assumed, and is not valid in general. A discrete Green's function approach has also been developed to solve such problems [4,10]. Solutions for several other steady-state problems have also been summarized [8]. Unsteady convective heat transfer has also been analyzed [11,12]. For example, the effect of time-varying plate flux, including a step change in heat flux has been accounted for using the Karman-Pohlhausen approach [7], resulting in a partial differential equation for the plate temperature as a function of time and space. This problem has also been solved using Laplace transform approach [13] and Green's functions [14]. Other considerations such as turbulence [15], non-flat surface [16] and finite thickness plate [17] have also been investigated. Unsteady convective heat transfer analysis often results in a differential equation that must be solved numerically due to the lack of a closed-form analytical solution.

While there is, in general, extensive literature on external convective heat transfer, one particular problem that has not been discussed much in the literature is that of a flat plate with heat flux that varies both in space and in time, i.e. $q_p=q_p(x,t)$. While solutions have been presented for

problems where the heat flux varies only in space, $q_p(x)$ [6] or only in time, $q_p(t)$ [7], a solution of the general $q_p(x,t)$ problem is desirable for many practical applications. For example, the problem of fluid flow over a bed of phase change material (PCM) occurs commonly in latent energy storage systems [18,19]. In such a case, heat flux at the fluid-PCM interface varies over space due to boundary layer development in the fluid flow, and also varies in time because of phase change front propagation into the PCM over time [20]. While such problems involving flow over a PCM have been solved by assuming a specific form of the Nusselt number [21,22], this assumption is likely to be inaccurate due to the expected time and spatial variation. Another example is the cooling of a Li-ion cell [23]. Thermal management of Li-ion cells – used commonly for energy storage and conversion in electric vehicles and other applications – often involves flow of a coolant fluid over the cell or battery pack. In such a case, the interface flux may vary with space due to boundary layer growth, and may also vary in time due to fluctuations in heat generation inside the cell in response to transient changes in the electrical load. Analysis of convective heat transfer from a plate with heat flux that varies in both space and time is critical for understanding and optimizing these and other related engineering applications. Unlike problems with only time-varying or only spatially-varying heat flux, the more general problem identified above has not been sufficiently addressed in the literature.

This paper presents a solution for external convective heat transfer between a flat plate and fluid flow where the plate heat flux changes with time as well as space. Laminar incompressible flow with constant freestream velocity and temperature is assumed. Velocity and temperature distributions are represented by fourth-order Karman-Pohlhausen polynomials. It is shown that the plate temperature is governed by a first-order hyperbolic partial differential equation involving the given heat flux and its derivatives. While an analytical solution for this equation is unlikely, the

equation is integrated numerically to determine the plate temperature as a function of space and time for any arbitrary heat flux distribution. Results from this work are shown to agree well with past results for special cases of time-varying [7], spatially-varying [6] or constant flux [1]. Various general cases of time- and space-varying heat flux, such as those that might arise in applications discussed above are analyzed.

4-2. Mathematical modeling

As shown schematically in Figure 1, consider laminar, incompressible fluid flow past a thin, one-dimensional flat plate in which the wall flux, q_p, varies both in space and in time. Uniform freestream velocity U_∞ and temperature T_∞ are assumed. All properties are assumed to be independent of temperature. Viscous dissipation is neglected. The interest here is to determine the nature of heat transfer between the flat plate and the fluid flow. In particular, the resulting plate temperature $T_p(x,t)$ due to the spatial and time variation in flux, $q_p(x,t)$, is of interest.
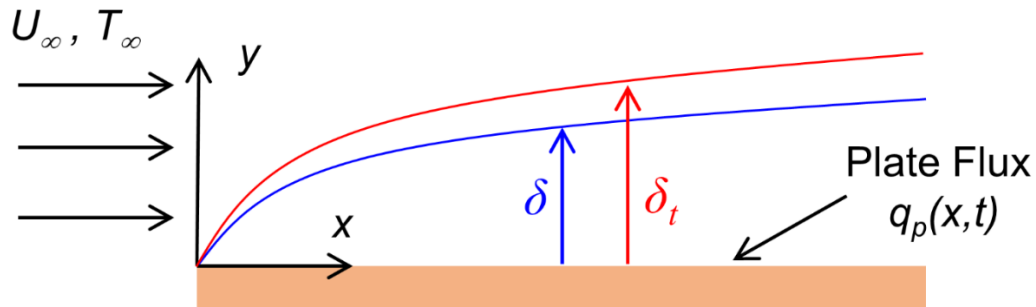
Figure 1. Schematic of the geometry considered in this work, comprising laminar, incompressible flow past a thin, flat plate with time- and space-varying heat flux.

Under the assumptions listed above, and referring to Figure 1 for the coordinate system, the governing equations for conservation of mass, momentum and energy can be written as

$$\frac{\partial U}{\partial x} + \frac{\partial V}{\partial y} = 0 \qquad (1)$$

$$U\frac{\partial U}{\partial x} + V\frac{\partial U}{\partial y} = \nu\frac{\partial^2 U}{\partial y^2} \qquad (2)$$

$$\alpha\frac{\partial^2 \theta}{\partial y^2} = \frac{\partial \theta}{\partial t} + U\frac{\partial \theta}{\partial x} + V\frac{\partial \theta}{\partial y} \qquad (3)$$

Where $\theta = T - T_\infty$.

The boundary conditions are

$$U = U_\infty; \ \theta = 0 \ at \ x = 0 \qquad (4)$$

$$U = 0; V = 0 \ at \ y = 0 \qquad (5)$$

$$U = U_\infty \ at \ y \geq \delta \qquad (6)$$

$$\theta = 0 \ at \ y \geq \delta_t \qquad (7)$$

$$-k\frac{\partial \theta}{\partial y} = q_p(x, t) \ at \ y = 0 \qquad (8)$$

Equation (4) represents the uniform freestream velocity of the fluid flow. Equation (5) is the no slip condition at the wall. Equations (6) and (7) are based on δ and δ_t, the momentum and thermal boundary layer thicknesses, respectively. Equation (8) is the given heat flux at the flat plate. In addition, the initial temperature field, $\theta(x, y, t = 0)$, is assumed to be zero. The interest is in solving this set of equations to determine the plate temperature $\theta_p(x, t) = \theta(x, y = 0, t)$.

4-2-1. Solution procedure

It is assumed that hydrodynamic boundary layer growth is unaffected by heat transfer. Integral analysis of momentum transfer in this problem can be shown to result in the following expression for the momentum boundary layer thickness, δ [6,7]

$$\delta(x) = 5.83 \sqrt{\frac{vx}{U_\infty}} \tag{9}$$

In order to solve this problem, the velocity and temperature distributions in their respective boundary layers are assumed to be given by fourth-order Karman-Pohlhausen polynomials [1,6,7] as follows:

$$\frac{U(x,y,t)}{U_\infty} = 2\frac{y}{\delta} - 2\left(\frac{y}{\delta}\right)^3 + \left(\frac{y}{\delta}\right)^4 \tag{10}$$

$$\frac{\theta(x,y,t)}{\theta_p} = 1 - 2\frac{y}{\delta_t} + 2\left(\frac{y}{\delta_t}\right)^3 - \left(\frac{y}{\delta_t}\right)^4 \tag{11}$$

These polynomials that already satisfy several boundary conditions in the problem are substituted into the integrated form of the energy equation in order to satisfy overall energy conservation. To do so, equation (3) is first integrated from $y=0$ to $y=\delta_t$, resulting in

$$\frac{\partial}{\partial t}\int_0^{\delta_t} \theta\,dy + \frac{\partial}{\partial x}\int_0^{\delta_t} U\theta\,dy = -\alpha\left(\frac{\partial\theta}{\partial y}\right)_{y=0} = \frac{q_p}{\rho c} \tag{12}$$

By substituting the polynomial form of θ from equation (11) into the first term of equation (12), it can be shown that

$$\frac{\partial}{\partial t}\int_0^{\delta_t}\theta dy = \frac{6}{5}\frac{k\theta_p}{q_p}\frac{\partial\theta_p}{\partial t} - \frac{3}{5}\frac{k\theta_p^2}{q_p^2}\frac{\partial q_p}{\partial t} \tag{13}$$

Also, substituting equations (10) and (11) into the second term in equation (12) results in

$$\frac{\partial}{\partial x}\int_0^{\delta_T}U\theta dy = U_\infty\frac{\partial}{\partial x}\left[\frac{8}{15}\frac{k^2\theta_p^3}{q_p^2 C\sqrt{x}} - \frac{12}{35}\frac{k^4\theta_p^5}{q_p^4 C^3 x\sqrt{x}} + \frac{8}{45}\frac{k^5\theta_p^6}{q_p^5 C^4 x^2}\right] \tag{14}$$

Where $C = 5.83\sqrt{\dfrac{v}{U_\infty}}$.

Recognizing that θ_p and q_p are both functions of x and t, equation (14) can be differentiated by parts to result in

$$\frac{\partial}{\partial x}\int_0^{\delta_T}U\theta dy = U_\infty\left[\frac{8}{15}\frac{k^2}{C}\left(-\frac{2}{q_p^3}\frac{\partial q_p}{\partial x}\frac{\theta_p^3}{\sqrt{x}} + \frac{1}{q_p^2}\left(\frac{3\theta_p^2}{\sqrt{x}}\frac{\partial\theta_p}{\partial x} - \frac{\theta_p^3}{2x\sqrt{x}}\right)\right)\right.$$

$$-\frac{12}{35}\frac{k^4}{C^3}\left(-\frac{4}{q_p^5}\frac{\partial q_p}{\partial x}\frac{\theta_p^5}{x\sqrt{x}} + \frac{1}{q_p^4}\left(\frac{5\theta_p^4}{x\sqrt{x}}\frac{\partial\theta_p}{\partial x} - \frac{3\theta_p^5}{2x^2\sqrt{x}}\right)\right) \tag{15}$$

$$\left.+\frac{8}{45}\frac{k^5}{C^4}\left(-\frac{5}{q_p^6}\frac{\partial q_p}{\partial x}\frac{\theta_p^6}{x^2} + \frac{1}{q_p^5}\left(\frac{6\theta_p^5}{x^2}\frac{\partial\theta_p}{\partial x} - \frac{2\theta_p^6}{x^3}\right)\right)\right]$$

Substituting equations (13) and (15) in the integral energy equation given in equation (12), followed by mathematical simplification results in a partial differential equation of the form

$$A(\theta_p, x, t)\frac{\partial\theta_p}{\partial t} + B(\theta_p, x, t)\frac{\partial\theta_p}{\partial x} = F(\theta_p, x, t) \tag{16}$$

Where

$$A(\theta_p, x, t) = \frac{6}{5} \frac{\theta_p q_p^4 C}{k^3} \tag{17}$$

$$B(\theta_p, x, t) = U_\infty \left[\frac{8}{5} \frac{\theta_p^2 q_p^3}{k^2 \sqrt{x}} - \frac{12}{7} \frac{\theta_p^4 q_p}{C^2 x \sqrt{x}} + \frac{16}{15} \frac{\theta_p^5}{C^3 x^2} k \right] \tag{18}$$

$$F(\theta_p, x, t) = \frac{\alpha q_p^6 C}{k^5} + \frac{3C \theta_p^2 q_p^3}{5k^3} \frac{\partial q_p}{\partial t}$$

$$+ \left[\frac{4\theta_p^3 q_p^3}{15k^2 x\sqrt{x}} - \frac{18q_p \theta_p^5}{35C^2 x^2 \sqrt{x}} + \frac{16k\theta_p^6}{45C^3 x^3} \right] U_\infty \tag{19}$$

$$- \frac{\partial q_p}{\partial x} \left[-\frac{16q_p^2 \theta_p^3}{15k^2 \sqrt{x}} + \frac{48\theta_p^5}{35C^2 x\sqrt{x}} - \frac{8k\theta_p^6}{9C^3 x^2 q_p} \right] U_\infty$$

Equation (16) along with coefficients defined in equations (17)-(19) represents the governing equation for the plate temperature for the general case considered here, where the imposed plate flux varies with both x and t. Note that the heat flux function $q_p(x, t)$ and its derivatives appearing in the coefficients of equation (16) are known in advance, and therefore, equation (16) is a non-linear, first-order hyperbolic partial differential equation in $\theta_p(x, t)$. While it is unlikely that equation (16) has a general closed-form solution, hyperbolic differential equations such as equation (16) can be solved numerically.

4-2-2. Numerical integration

In order to numerically compute the solution of equations (16)-(19), discretization in x direction is carried out to convert the partial differential equation into a coupled system of ordinary differential equations in $\theta_{p,i}(t)$ where the subscript i refers to the discretized spatial location. The coupled system of ordinary differential equations is then solved by numerical integration over time

with a three-stage, third-order, Runge-Kutta solver using adaptive time-stepping [24]. The initial condition provides the initial state needed for starting the integration process.

4-3. Results and discussion

4-3-1. Special cases

It is instructive to compare special cases of the general results derived in Section 2 with past work that investigated specific special cases of this problem.

In case the plate flux is a function of time alone, i.e. $q_p = q_p(t)$, then the last set of terms in equation (19) that appear with $\frac{\partial q_p}{\partial x}$ can be set to zero. Even if the plate flux may not be spatially dependent, the plate temperature will still be a function of both x and t due to boundary layer development. For this case, the general governing equation can be simplified to

$$\frac{6}{5}\frac{\theta_p q_p^4 C}{k^3}\frac{\partial \theta_p}{\partial t} + \left[\frac{8}{5}\frac{\theta_p^2 q_p^3}{k^2\sqrt{x}} - \frac{12}{7}\frac{\theta_p^4 q_p}{C^2 x\sqrt{x}} + \frac{16}{15}\frac{\theta_p^5}{C^3 x^2}k\right]U_\infty\frac{\partial \theta_p}{\partial x} - \frac{3C\theta_p^2 q_p^3}{5k^3}\frac{\partial q_p}{\partial t}$$

$$- \left[\frac{4\theta_p^3 q_p^3}{15k^2 x\sqrt{x}} - \frac{18 q_p\theta_p^5}{35C^2 x^2\sqrt{x}} + \frac{16k\theta_p^6}{45C^3 x^3}\right]U_\infty = \frac{\alpha q_p^6 C}{k^5}$$

(20)

Equation (20) matches exactly with the result from Lachi, *et al.* [7] that considered the specific case of time-varying heat flux on the flat plate.

Further, the case of only spatially-varying plate flux, i.e. $q_p = q_p(x)$ is of interest. In such a case, the $\frac{3C\theta_p^2 q_p^3}{5k^3}\frac{\partial q_p}{\partial t}$ term appearing in equation (19) can be eliminated. Therefore, the governing equation for this case is

$$\frac{6}{5}\frac{\theta_p q_p^4 C}{k^3}\frac{\partial \theta_p}{\partial t} + \left[\frac{8}{5}\frac{\theta_p^2 q_p^3}{k^2\sqrt{x}} - \frac{12}{7}\frac{\theta_p^4 q_p}{C^2 x\sqrt{x}} + \frac{16}{15}\frac{\theta_p^5}{C^3 x^2}k\right]U_\infty\frac{\partial \theta_p}{\partial x}$$

$$+ \frac{\partial q_p}{\partial x}\left[-\frac{16 q_p^2\theta_p^3}{15 k^2\sqrt{x}} + \frac{48\theta_p^5}{35 C^2 x\sqrt{x}} - \frac{8k\theta_p^6}{9 C^3 x^2 q_p}\right]U_\infty \qquad (21)$$

$$+ \left[-\frac{4\theta_p^3 q_p^3}{15 k^2 x\sqrt{x}} + \frac{18 q_p\theta_p^5}{35 C^2 x^2\sqrt{x}} - \frac{16k\theta_p^6}{45 C^3 x^3}\right]U_\infty = \frac{\alpha q_p^6 C}{k^5}$$

The transient problem of spatially-varying plate flux was presented by Polidori & Padet [6]. Appendix A shows that the governing equation obtained above by simplifying the equation for the general $q_p(x,t)$ case agrees exactly with results from Polidori & Padet [6].

Further, the steady state component of the spatially-varying heat flux problem is a standard problem, for which, the solution is available [1] as follows:

$$\theta_p(x) = \frac{0.623}{k}Pr^{-1/3}Re_x^{-1/2}\int_0^x q_p(\xi)\left[1 - \left(\frac{\xi}{x}\right)^{3/4}\right]^{-2/3}d\xi \qquad (22)$$

In comparison, in the present work, for steady state conditions with $q_p=q_p(x)$, equation (21) can be further simplified to

$$\left[\frac{8}{5}\frac{\theta_p^2 q_p^3}{k^2\sqrt{x}} - \frac{12}{7}\frac{\theta_p^4 q_p}{C^2 x\sqrt{x}} + \frac{16}{15}\frac{\theta_p^5}{C^3 x^2}k\right]U_\infty\frac{\partial \theta_p}{\partial x}$$

$$+ \frac{\partial q_p}{\partial x}\left[-\frac{16 q_p^2\theta_p^3}{15 k^2\sqrt{x}} + \frac{48\theta_p^5}{35 C^2 x\sqrt{x}} - \frac{8k\theta_p^6}{9 C^3 x^2 q_p}\right]U_\infty \qquad (23)$$

$$+ \left[-\frac{4\theta_p^3 q_p^3}{15 k^2 x\sqrt{x}} + \frac{18 q_p\theta_p^5}{35 C^2 x^2\sqrt{x}} - \frac{16k\theta_p^6}{45 C^3 x^3}\right]U_\infty = \frac{\alpha q_p^6 C}{k^5}$$

Equation (23) is an ordinary differential equation in $\theta_p(x)$, which is difficult to solve analytically due to its non-linear nature. However, a numerical computation of equation (23) can be compared against equation (22).

Finally, note that the solution for a flat plate with constant heat flux is [1]

$$\theta_p(x) = \frac{q_p}{0.453k} Pr^{-1/3} Re_x^{-1/2} x \tag{24}$$

whereas, the present work, through elimination of terms appearing with $\frac{\partial q_p}{\partial x}$ in equation (23) results in

$$\left[\frac{8}{5} \frac{\theta_p^2 q_p^3}{k^2 \sqrt{x}} - \frac{12}{7} \frac{\theta_p^4 q_p}{C^2 x \sqrt{x}} + \frac{16}{15} \frac{\theta_p^5}{C^3 x^2} k \right] U_\infty \frac{\partial \theta_p}{\partial x}$$
$$+ \left[-\frac{4\theta_p^3 q_p^3}{15 k^2 x \sqrt{x}} + \frac{18 q_p \theta_p^5}{35 C^2 x^2 \sqrt{x}} - \frac{16 k \theta_p^6}{45 C^3 x^3} \right] U_\infty = \frac{\alpha q_p^6 C}{k^5} \tag{25}$$

The equations for special cases resulting from the present work are plotted along with past results in the next section.

4-3-2. Model validation

The analytical model derived in this work is compared against results from past papers that have presented theoretical analysis of similar problems. Firstly, results are compared with Lachi, *et al.* [7], who presented the analysis of unsteady convective heat transfer with a time-dependent flat plate heat flux, $q_p(t)$. For this comparison, a specific case of step change heat flux considered by Lachi, *et al.* was also implemented in the present analytical model. This step change involves a change of heat flux from φ_1 to φ_2 ($\varphi_2 > \varphi_1$) at a time t_0. Equation (20) is solved for this specific heat flux profile in order to compute the plate temperature as a function of x and t. Under the same freestream conditions and fluid properties, a comparison with Lachi, *et al.* [7] is presented in Figure 2, where plate temperature and Nusselt number at multiple locations are plotted as functions of

time in Figures 2(a) and 2(b), respectively. In general, there is very good agreement between the present work and Lachi, *et al.* for the special case of time-dependent plate heat flux. The plate temperature rises with time, including a sharp rise beyond $t=t_0$ when the heat flux undergoes a step change. Further, the greater the value of x, the higher is the temperature, which is due to boundary layer growth and diminished heat transfer from the plate at large x. Similarly, Nu reduces with time and then undergoes a large increase at $t=t_0$ due to the increased heat flux, as expected, and then finally reduces with increasing time. The larger the value of x, the higher is the value of Nu, which is also expected.
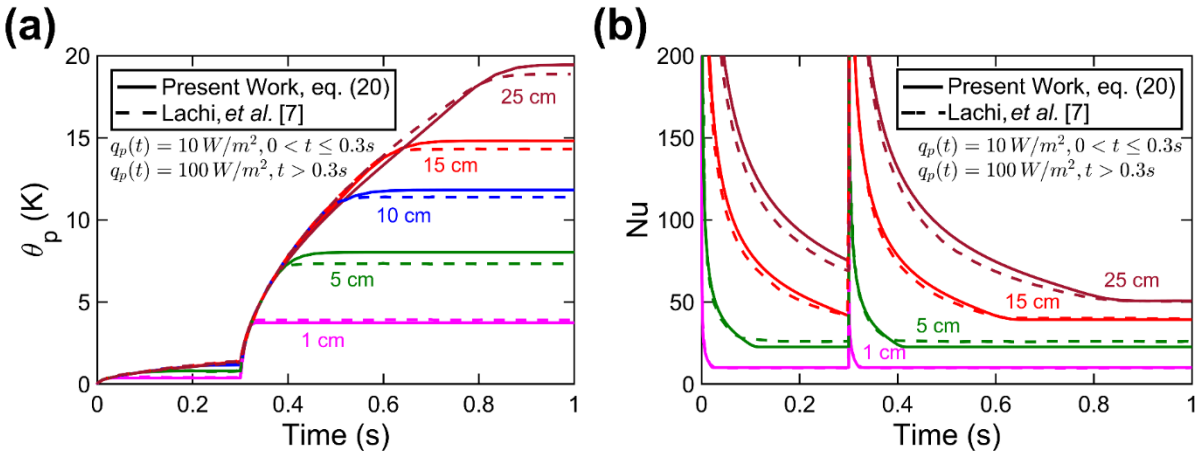
Figure 2. Comparison of present work with Lachi, et al. [7] for the special case of time-dependent heat flux, $q_p(t) = \begin{cases} 10\ W/m^2, & 0 < t \leq 0.3\ s \\ 100,\ W/m^2 & t > 0.3\ s \end{cases}$: (a) Plate temperature, θ_p vs t at multiple x, and (b) Nu vs t at the plate at multiple x.

Further, the present work is compared with Polidori & Padet [6] for the special case of spatially-varying heat flux, qp(x). A specific form of $q_p(x) = 150 \cdot \exp(-10x)\ W/m^2$ used in their work is also implemented in the present model, equation (21), which pertains to the special case of spatially-varying heat flux, qp(x). Comparison of the present work with Polidori & Padet is presented in Figure 3, which plots the spatial distribution in the plate temperature at multiple

times prior to steady state. At each time, the plate temperature increases with x, and then decreases after reaching a maxima. This is because the plate flux reduces exponentially as x increases. At each time, there is good agreement between the past work and the present model. Please note that the approach for numerical solution of the derived equations are different between Polidori & Padet and the present work. Polidori & Padet adopted an explicit finite-difference scheme [6], whereas in the present work, the partial differential equation is discretized in space, and the resulting system of ordinary differential equations are solved numerically using a three-stage, third-order, Runge-Kutta method. This difference between the two approaches may explain the small discrepancy between the two sets of curves in Figure 3.
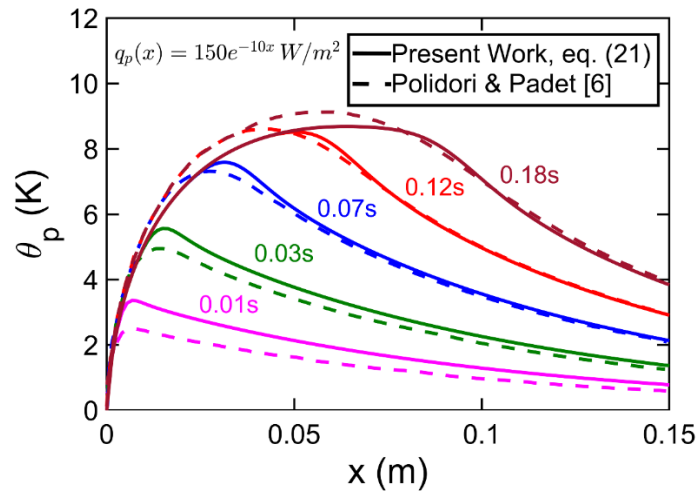
Figure 3. Comparison of present work with Polidori & Padet [6] for the special case of spatially-varying heat flux: Plate temperature, θ_p as a function of x at multiple different times for $q_p(x) = 150e^{-10x} \, W/m^2$. Note that x is in m.

The problem of spatially-varying plate temperature has also been solved in steady state using superposition methods [1]. In short, the solution for a problem with constant plate temperature has been derived and then superimposed based on linearity of the problem to determine the solution for the spatially-varying plate temperature problem. A comparison of the present work with these

results is presented in Figures 4(a) and 4(b) for two specific $q_p(x)$ profiles – linear and one in which $q_p(x)$ reduces proportional to $\sqrt{x}$. In both cases, there is good agreement between the two. Note that this good agreement is particularly encouraging because the approach in the superposition-based method is distinctly different from the approach in the present work.
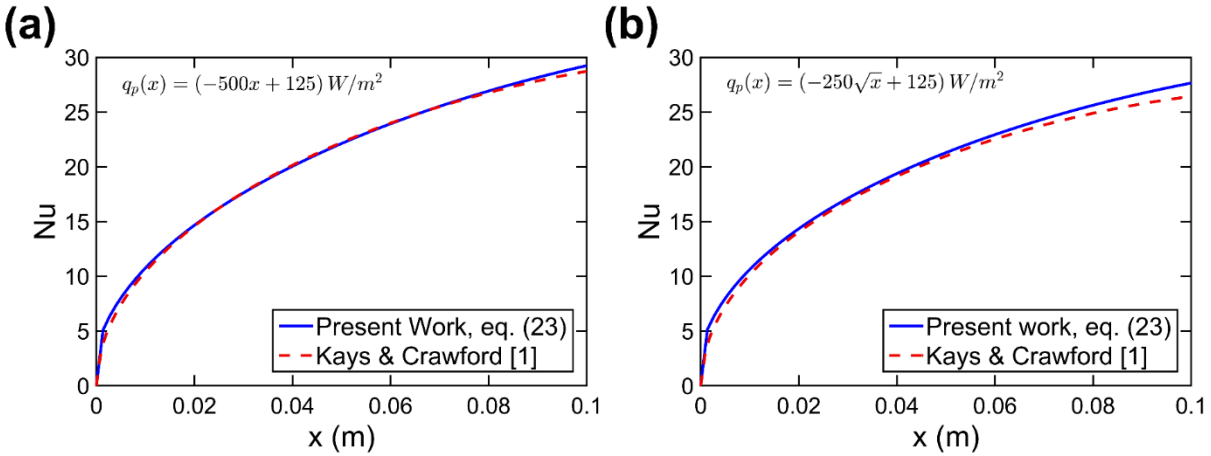
Figure 4. Comparison of present work with Kays & Crawford [1] for the special case of steady state spatially-dependent heat flux: (a) Plate temperature in the form of Nusselt number, Nu, as a function of x for (a) linear $q_p(x) = -500x + 125\ W/m^2$, (b) non-linear $q_p(x) = -250\sqrt{x} + 125\ W/m^2$. Note that x is in m.

Finally, comparison with past work is carried out for the simplest case of a constant heat flux plate. A solution for this case has been presented in Kays & Crawford [1], and is reproduced as equation (24) in the present work. Figure 5 presents the variation in Nu as a function of x for a constant heat flux plate, based on the present model as well as past results. The two are in excellent agreement with each other.
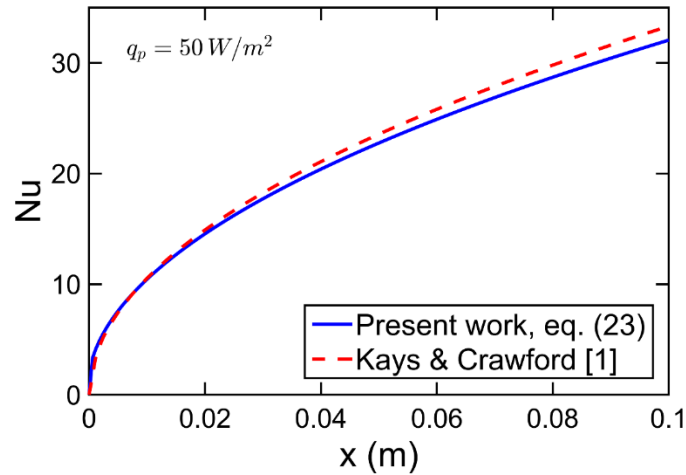
Figure 5. Comparison of present work with Kays & Crawford [1] for the special case of steady state constant heat flux (a) Nu as a function of x.

The good agreement between the present work and various past results for special cases of $q_p(t)$, $q_p(x)$ and constant q_p provides confidence in the present approach.

4-3-3. Plate temperature for specific $q_p(x,t)$ functions

The plate temperature distribution is determined for several representative plate flux profiles in order to further demonstrate the capability of the present analytical model.

In order to analyze a scenario where the plate flux changes with both time and space, a plate flux profile given by $q_p(x,t) = A + Bx + Ct$ is considered, where $A = 200 \, W/m^2$, $B = -400 \left(\frac{W}{m^2}\right)/m$ and $C = -50 \left(\frac{W}{m^2}\right)/s$. The freestream velocity is assumed to be 1 m/s. Room temperature properties of air are used. The resulting plate temperature distribution determined by solving equation (16) is plotted in Figure 6. Plate temperature as a function of x at three different times is plotted in Figure 6(a), while plate temperature as a function of time at four different locations is plotted in Figure 6(b). Figure 6(a) shows, as expected, that the plate temperature increases with x at any given time. A saturation effect at large values of x is also seen, as expected,

due to the saturation in boundary layer growth. The plate temperature decreases with time due to the decreasing nature of qp with time. Figure 6(b) shows that the plate temperature at any specific location increases sharply first, reaches a peak and then slowly decreases. The initial rise in temperature is due to heating up of the plate, which is followed by a cool down because the plate flux reduces with time according to the assumed form of the plate flux distribution, while the plate continues to be convectively cooled by the flow. Figure 6(b) shows that the larger the value of x, the larger is the temperature rise, which is expected due to the increasing boundary layer thickness and therefore, diminishing convective cooling as x increases.
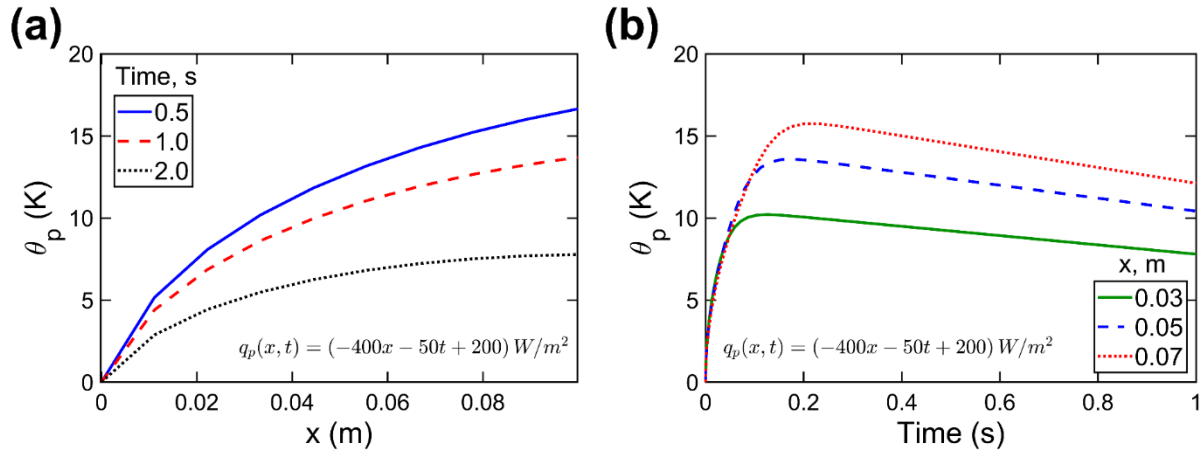
Figure 6. Plate temperature, θp as a function of (a) x at multiple times, and (b) time at multiple x for a general heat flux distribution given by $q_p(x, t) = [200 - 400x - 50t]\ W/m^2$.

.

Figure 7 presents results for a similar heat flux distribution, given by $q_p(x, t) = A + B\sqrt{x} + C\sqrt{t}$, with $A = 500\ W/m^2$, $B = -400\ \left(\frac{W}{m^2}\right)/\sqrt{m}$ and $C = -50\ \left(\frac{W}{m^2}\right)/\sqrt{s}$. Here, the dependence of plate flux of x and t is weaker than the previous case. Other problem parameters such as freestream velocity as the same as the previous Figure. Figures 7(a) and 7(b) plot the variation in plate temperature as a function of x and time, respectively. Similar to Figure 6(a), the plate temperature distribution in Figure 7(a) shows increasing temperature with x at any time, which is

consistent with reduced convective cooling at large x. Compared to Figure 6(a), the three curves in Figure 7(a) at three different times are much closer to each other, which is likely due to the slower rate of reduction in the plate heat flux with time compared to Figure 6. Note that the assumed plate flux for results shown in Figure 7 decays as $\sqrt{x}$ and $\sqrt{t}$, compared to the linear decay for Figure 6. Similar to Figure 6(b), there is initial rise in plate temperature at any given location, as shown in Figure 7(b). This is followed by a reduction in temperature, but at a much slower rate than in the previous case. This is also likely due to the weaker decay in the plate flux compared to the previous case.
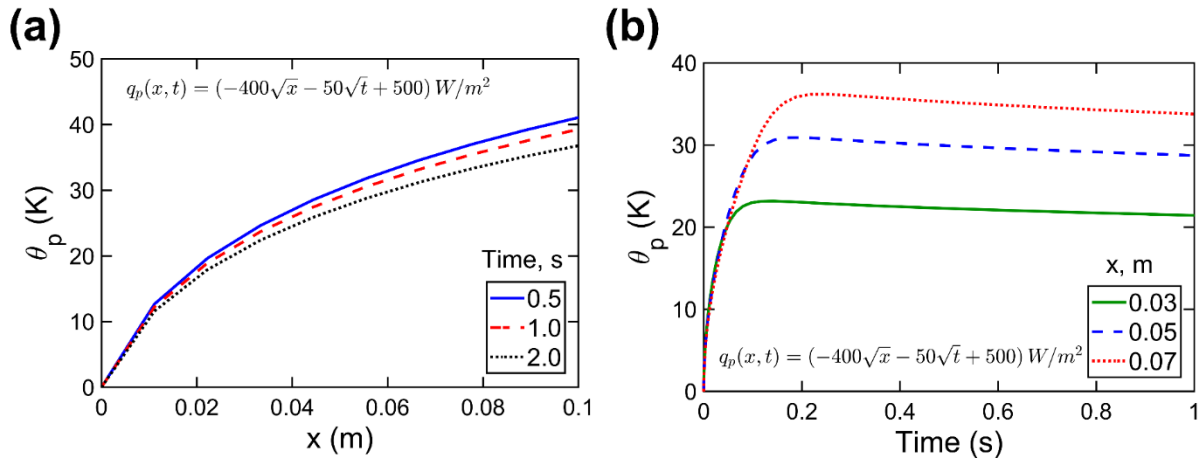
Figure 7. Plate temperature, θp as a function of (a) x at multiple times, and (b) time at multiple x for a general heat flux distribution given by $q_p(x,t) = [500 - 400\sqrt{x} - 50\sqrt{t}]\, W/m^2$.

Finally, a step function change in the plate flux is also considered, wherein the plate flux is given by $q_p = A + B_1\sqrt{x}$ for 0<t<0.3 s, and $q_p = A + B_2\sqrt{x}$ afterwards. The numerical values of these parameters are $A = 500\frac{W}{m^2}$, $B_1 = -400\left(\frac{W}{m^2}\right)/\sqrt{m}$ and $B_2 = -1000\left(\frac{W}{m^2}\right)/\sqrt{m}$. This constitutes a sharp drop in the plate flux after t=0.3 s. The resulting plate temperature distribution is plotted in Figure 8. Spatial distribution in the plate temperature at three different times is plotted in Figure 8(a), while plate temperature as a function of time at three different locations is plotted

in Figure 8(b). As expected, the plate temperature at any given location increases first with time up to t=0.3 s, with the temperature being greater at large values of x. This is followed by a gradual reduction due to the step change in the flux distribution. Eventually, the plate temperature at each location reaches a steady state. Temperature at steady state increases with increasing value of x, which is due to reduced convective cooling at large x. The plate temperature distribution at three different times, shown in Figure 8(a) indicates that the plate temperature rises with x and eventually plateaus out. Similar to Figure 8(b), this occurs due to the reduced convective cooling at large x, combined with the gradual reduction in the plate flux with x, based on the assumed flux distribution.

Figures 6-8 demonstrate the capability of the theoretical model derived in this work to account for a given plate heat flux as a function of both space and time in order to predict the resulting temperature distribution. If experimental data on the plate heat flux are available, it may also be inserted into equations (16)-(19) to predict the temperature distribution. In such a case, the derivatives $\frac{\partial q_p}{\partial t}$ and $\frac{\partial q_p}{\partial x}$ appearing in equation (17) may need to be evaluated numerically.
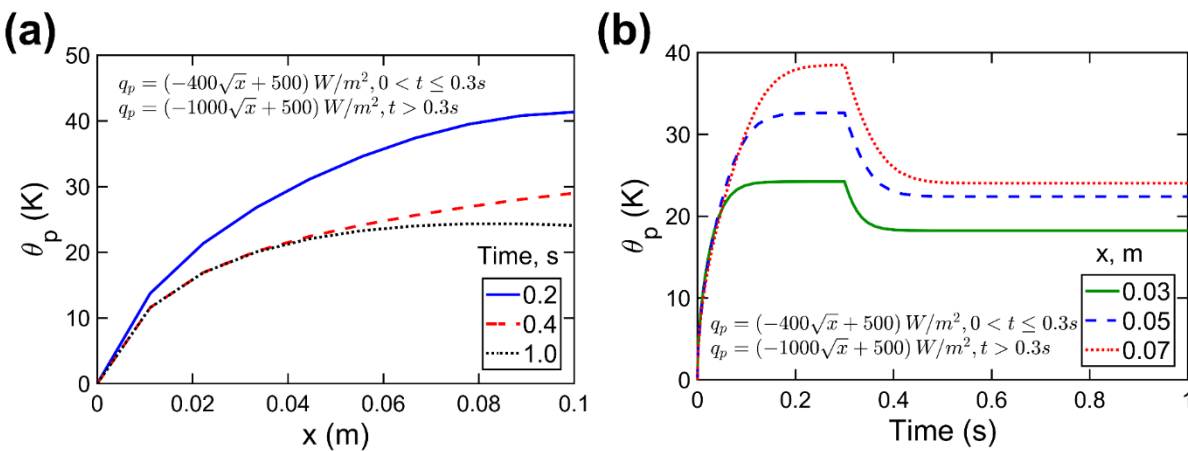
Figure 8. Plate temperature, θ_p as a function of (a) x at multiple times, and (b) time at multiple x for a general heat flux distribution given by $q_p(x, t) = [500 - 400\sqrt{x}] \, W/m^2$ for $t < 0.3s$ and $q_p(x, t) = [500 - 1000\sqrt{x}] \, W/m^2$ afterwards.

4-4. Conclusions

Understanding the nature of temperature distribution on a flat plate due to convective cooling in response to a plate heat flux that varies in both space and time is important for design and optimization of several practical engineering systems such as latent heat energy storage systems and thermal management of Li-ion batteries. In the past, such problems have been solved when the plate flux is a function of only time or only x. The present work generalizes this by considering the plate heat flux to be a function of both space and time. The generalized solution derived in this work is based on the integral approach and uses fourth-order Karman-Pohlhausen polynomials, which have been shown to offer reasonable accuracy. Results are shown to agree well with past work for specific cases of the general problem discussed in this work.

The present work does not account for second-order effects such as thermal resistance and capacitance of the flat plate, which may require solving a conjugate heat transfer problem, for which, the present results may be helpful. Also, turbulent effects, which may be important in specific applications are not accounted for in the present work.

The present work improves our fundamental understanding of external convective heat transfer. The results derived here may contribute towards design and optimization of practical engineering systems.

4-5. Nomenclature

c specific heat capacity, $Jkg^{-1}K^{-1}$

C coefficient, $C = 5.83\sqrt{\dfrac{\nu}{U_\infty}}$, $m^{0.5}$

k thermal conductivity, $Wm^{-1}K^{-1}$

Pr   Prandtl number

q   heat flux, Wm^{-2}

Re   Reynolds number

t   time, s

T   temperature, K

U,V   Velocities in *x* and *y* directions respectively, ms^{-1}

x,y   spatial coordinate, m

θ   relative temperature, K

α   thermal diffusivity, m^{2}s^{-1}

ν   kinematic viscosity, m^{2}s^{-1}

ρ   mass density kgm^{-3}

δ   boundary layer thickness, m

Subscripts

p   plate

t   thermal

∞   freestream

4-6. References

[1] W.M. Kays, M.E. Crawford, B. Weigand, Convective heat and mass transfer, McGraw-Hill Higher Education, Boston, 2005.

[2] A. Bejan, Convection heat transfer, Wiley, Hoboken (New Jersey), 2013.

[3] S. Kakaç, Y. Yener, A. Pramuanjaroenkij, Convective heat transfer, CRC Press, Boca Raton, FL, 2014.

[4] J.K. Eaton, The Discrete Green's Function for Convective Heat Transfer—Part 1: Definition and Physical Understanding, Journal of Heat Transfer. 142 (2020). doi:10.1115/1.4047515.

[5] J.H. Lienhard, Heat Transfer in Flat-Plate Boundary Layers: A Correlation for Laminar, Transitional, and Turbulent Flow, Journal of Heat Transfer. 142 (2020). doi:10.1115/1.4046795.

[6] G. Polidori, J. Padet, Transient laminar forced convection with arbitrary variation in the wall heat flux, Heat and Mass Transfer. 38 (2002) 301–307. doi:10.1007/s002310100273.

[7] M. Lachi, M. Rebay, E.C. Mladin, J. Padet, Alternative models for transient convection heat transfer in external flows over a plate exposed to a variable heat flux, International Journal of Thermal Sciences. 43 (2004) 809–816. doi:10.1016/j.ijthermalsci.2004.02.021.

[8] J.S. Klein, M. Tribus, Forced convection from nonisothermal surfaces, in: Proc.Heat Transfer Symp., University of Michigan Engineering Research Institute,1952.

[9] J.-J. Shu, I. Pop, On thermal boundary layers on a flat plate subjected to a variable heat flux, International Journal of Heat and Fluid Flow. 19 (1998) 79–84. doi:10.1016/s0142-727x(97)10026-1.

[10] J. Hacker, J. Eaton, Measurements of heat transfer in a separated and reattaching flow with spatially varying thermal boundary conditions, International Journal of Heat and Fluid Flow. 18 (1997) 131–141. doi:10.1016/s0142-727x(96)00142-7.

[11] N. Riley, Unsteady heat transfer for flow over a flat plate, Journal of Fluid Mechanics. 17 (1963) 97–104. doi:10.1017/s0022112063001130.

[12] S.C.R. Dennis, Unsteady heat transfer for boundary-layer flow over a flat plate, in: Recent Research on Unsteady Boundary Layers, IUTAM Symposium 1971, vol. 1, Laval University Press, Que., 1972, pp. 379–403.

[13] B. Chao, L. Cheema, Unsteady heat transfer in laminar boundary layer over a flat plate, International Journal of Heat and Mass Transfer. 11 (1968) 1311–1324. doi:10.1016/0017-9310(68)90177-4.

[14] A. Grine, J.Y. Desmons, S. Harmand, Models for transient conduction in a flat plate subjected to a variable heat flux, Applied Thermal Engineering. 27 (2007) 492–500. doi:10.1016/j.applthermaleng.2006.06.013.

[15] S.W. Churchill, A comprehensive correlating equation for forced convection from flat plates, AIChE Journal. 22 (1976) 264–268. doi:10.1002/aic.690220207.

[16] M. Jakob, W. M. Dow, Heat transfer from a cylindrical surface to air in parallel flow with and without unheated starting sections, Trans. ASME 88, 123-134 (1946).

[17] A. Luikov, Conjugate convective heat transfer problems, International Journal of Heat and Mass Transfer. 17 (1974) 257–265. doi:10.1016/0017-9310(74)90087-8.

[18] A. Trp, An experimental and numerical investigation of heat transfer during technical grade paraffin melting and solidification in a shell-and-tube latent thermal energy storage unit, Solar Energy. 79 (2005) 648–660. doi:10.1016/j.solener.2005.03.006.

[19] M. Lacroix, Study of the heat transfer behavior of a latent heat thermal energy storage unit with a finned tube, International Journal of Heat and Mass Transfer. 36 (1993) 2083–2092. doi:10.1016/s0017-9310(05)80139-5.

[20] V. Alexiades, A.D. Solomon, Mathematical Modeling of Melting and Freezing Processes, Routledge, Boca Raton, 2018.

[21] M. Bechiri, K. Mansouri, Exact solution of thermal energy storage system using PCM flat slabs configuration, Energy Conversion and Management. 76 (2013) 588–598. doi:10.1016/j.enconman.2013.07.051.

[22] C. Ding, Z. Niu, B. Li, D. Hong, Z. Zhang, M. Yu, Analytical modeling and thermal performance analysis of a flat plate latent heat storage unit, Applied Thermal Engineering. 179 (2020) 115722. doi:10.1016/j.applthermaleng.2020.115722.

[23] K. Shah, V. Vishwakarma, A. Jain, Measurement of Multiscale Thermal Transport Phenomena in Li-Ion Cells: A Review, Journal of Electrochemical Energy Conversion and Storage. 13 (2016). doi:10.1115/1.4034413.

[24] https://www.mathworks.com/help/matlab/ref/ode23.html, accessed Dec 21, 2020.

Appendix A: Proof that results from present work agree with Polidori & Padet [6] for special case of $q_P(x)$

The general equation derived in the present for the plate temperature due to a time- and spatially-varying heat flux $q_P(x,t)$ (equation (16)) reduces to a simpler form, equation (21), for the special case of a heat flux that varies only in x, i.e., $q_p(x)$. This specific problem has been discussed in the past by Polidori & Padet [6]. In order to establish that equation (21) matches with the results in Polidori & Padet [6], one may begin with equation (4) of their paper. This equation, with variable names changed to match the present work is

$$\frac{3}{10}\frac{\partial}{\partial t}[\theta_p \delta_t] + U_\infty \frac{\partial}{\partial x}\left[\theta_p\left(\frac{2}{15}\frac{\delta_t^2}{\delta} - \frac{3}{140}\frac{\delta_t^4}{\delta^3} + \frac{1}{180}\frac{\delta_t^5}{\delta^4}\right)\right] = \frac{\nu q_p}{k \cdot Pr} \tag{A.1}$$

Introducing $\delta(x) = C\sqrt{x}$ for the momentum boundary layer thickness and $\delta_t = \frac{2k\theta_p}{q_p}$, one may

simplify equation (A.1) to

$$\frac{6}{5}\frac{k\theta_p}{q_p}\frac{\partial \theta_p}{\partial t} + U_\infty \frac{\partial}{\partial x}\left[\left(\frac{8}{15}\frac{k^2\theta_p^3}{Cq_p^2\sqrt{x}} - \frac{12}{35}\frac{k^4\theta_p^5}{C^3q_p^4x\sqrt{x}} + \frac{8}{45}\frac{k^5\theta_p^6}{C^4q_p^5x^2}\right)\right] = \frac{\alpha q_p}{k} \tag{A.2}$$

Since θ_p and q_p are both functions of x, the second term in equation (A.2) is differentiated by

parts. In addition, the entire equation is multiplied by $\frac{Cq_p^5}{k^4}$, resulting in

$$\frac{6}{5}\frac{\theta_p q_p^4 C}{k^3}\frac{\partial \theta_p}{\partial t} + \left[\frac{8}{5}\frac{\theta_p^2 q_p^3}{k^2\sqrt{x}} - \frac{12}{7}\frac{\theta_p^4 q_p}{C^2 x\sqrt{x}} + \frac{16}{15}\frac{\theta_p^5}{C^3 x^2}k\right]U_\infty\frac{\partial \theta_p}{\partial x}$$

$$+ \frac{\partial q_p}{\partial x}\left[-\frac{16q_p^2\theta_p^3}{15k^2\sqrt{x}} + \frac{48\theta_p^5}{35C^2 x\sqrt{x}} - \frac{8k\theta_p^6}{9C^3 x^2 q_p}\right]U_\infty \tag{A.3}$$

$$+ \left[-\frac{4\theta_p^3 q_p^3}{15k^2 x\sqrt{x}} + \frac{18q_p\theta_p^5}{35C^2 x^2\sqrt{x}} - \frac{16k\theta_p^6}{45C^3 x^3}\right]U_\infty = \frac{\alpha q_p^6 C}{k^5}$$

Equation (A.3) is identical to the result from the present work for the special case of $q_p(x)$,

given by equation (21). Therefore, the generalized result derived in the present work reduces to

the one presented by Polidori & Padet [6] for the special case of a plate heat flux that varies only

with x.

Chapter 5

Theoretical analysis of unsteady convective heat transfer from a flat plate with time-varying and spatially-varying temperature distribution

Under Preparation for Journal Submission

5-1. Introduction

Convective heat transfer due to external flow past a solid surface such as a flat plate is a commonly occurring and heavily researched problem in heat transfer [1,2]. Despite the long history of research on such problems [3], this continues to be an area of active interest [2, 4]. A few representative applications include heat exchangers, turbine blade cooling, energy storage and propulsion. While practical problems may present several complexities such as compressible flow, surface curvature, temperature-dependent properties and turbulence, engineering approximations are commonly made to simplify analysis of the problem.

Broadly, there are two standard sets of problems in external convective heat transfer involving a flat plate. In the first set, the flat plate temperature, T_p is given and the interest is to determine the plate heat flux, q_p. The second set is the opposite problem – given the plate heat flux, the goal is to determine the plate temperature. In the simplest problems, the given plate temperature or heat flux is steady and uniform [1], whereas spatial and temporal dependence of the imposed boundary condition has also been accounted for in advanced problems [5-8]. For example, the steady state problem with spatially varying plate temperature or heat flux has been solved by superimposition of the solution of a fundamental problem of a plate with an unheated length [1, 9]. The Discrete Green's Function (DGF) technique has also been used for solving such problems [4]. A summary of steady state solutions for both temperature and heat flux boundary conditions is available [3, 10]. Unsteady problems with time-varying plate temperature have also been solved. Such problems often occur when the flat plate is suddenly heated up [5, 6], or when the temperature at the surface of a thick plate varies in time due to internal heat generation. The resulting rate of heat transfer to the fluid flow as a function of time is of interest. The simplest problem of step change in plate temperature at t=0 has been solved using Laplace transforms for large times [5, 6] and direct

solution of the differential energy conservation equation for small times [5]. This solution has also been used to construct the solution for an arbitrary variation in plate temperature with time [5]. Problems with time-dependent [7] and spatially-varying [8] heat flux boundary conditions have also been solved using the Karman-Pohlhausen integral technique [1]. More recently, this technique was used to solve a general problem in which the plate heat flux is a function of both space and time [11]. In addition to the analytical work summarized above, a vast amount of literature also exists [12] on the use of numerical methods to solve problems with additional complications such as temperature-dependent properties [13], conjugate heat transfer due to thermal resistance and capacitance offered by the flat plate [14, 15], etc.

Two common analytical approaches are available for solving convective heat transfer problems. In some cases, the use of self-similar velocity and temperature profiles is found to result in simplification of the problem and derivation of ordinary differential equations that can solved to determine the flow and temperature fields. A well-known example is that of a constant temperature flat plate, in which case, the Blasius solution for the flow field [16] can be used to derive a similar solution for the temperature distribution, and thus, the plate heat flux [1]. Despite the mathematical elegance and exactness of the solution, this technique is limited only to the simplest problems where a self-similar solution may be expected to exist. Another approach is based on the Karman-Pohlhausen method, in which, polynomial forms of the velocity and temperature fields that satisfy the required boundary conditions are assumed. These assumed forms are then used to satisfy the integral form of the conservation equation. The Karman-Pohlhausen approach is based on the premise that the specific form of the velocity and temperature profiles in the boundary layers is not as critical as the requirements to satisfy the boundary conditions. Karman-Pohlhausen polynomials of second, third and fourth degrees have been used [1, 2, 8] and

shown to result in reasonable accuracy. In addition to the two approaches discussed above, Green's functions [4] and Laplace transforms [5, 6] have also been used to solve steady-state and transient problems, respectively.

While problems with boundary conditions that vary in space alone or time alone have been addressed in the past, there is, in general, a lack of literature on problems where the plate temperature changes with both space and time. The analysis of such a problem may benefit several engineering applications. For example, temperature at the interface between a bed of Phase Change Material (PCM) and fluid flow in a latent heat energy storage system [17] is likely to change in both space and time. The interface temperature is likely to change in space due to heat transfer to/from the fluid which is greatest at the leading edge and trails off afterwards. Further, the interface temperature changes in time because as the phase change front propagates into the PCM over time, there will be reduced heat transfer to/from the fluid flow due to the additional thermal resistance of the newly formed phase. Other applications where the plate surface temperature may be a function of both space and time include thermal management of Li-ion cells undergoing variable-rate discharge [18], startup problems related to heat exchangers [19], etc. While recent work has analyzed the problem with given time- and space-dependent plate heat flux, $q_P(x,t)$ [11], it is of interest to solve the problem with given time- and space-dependent plate temperature, $T_p(x,t)$, since temperature is often more easily measured than heat flux. Such an analysis may help design and optimize several engineering systems such as those listed above.

This paper presents a solution for convective heat transfer due to laminar, incompressible flow over a flat plate with a given plate temperature that varies in both space and time, $T_p(x,t)$. The transient energy conservation equation in a fluid flow is integrated across the thermal boundary layer, and third-order Karman-Pohlhausen polynomial expressions for fluid temperature and

velocity fields are used. This is shown to result in a general, first-order hyperbolic partial differential equation for the thermal boundary layer thickness, that can be solved to determine the plate heat flux as a function of space and time. The equation derived is a generalization of past results for special cases such as time-varying, spatially-varying or constant plate temperature. Results discussed here may benefit the analysis and optimization of several engineering applications where transient convective heat transfer between a flat plate and fluid flow is important.

5-2. Mathematical modeling

5-2-1. Problem statement

Consider incompressible laminar fluid flow past a semi-infinite flat plate as shown in Figure 1. The plate is thin, so that its thermal resistance and capacitance can be neglected. The freestream velocity and temperature of the flow, U_∞ and T_∞ are assumed to be constant. The plate temperature is known to be $T_p(x,t)$ and the interest is in determining the heat flux $\varphi_p(x,t)$ to/from the plate at any location and at any time. All properties are assumed to be uniform and constant. Under these assumptions, the governing continuity, momentum and energy conservation equations are

$$\frac{\partial u_x}{\partial x} + \frac{\partial u_y}{\partial y} = 0 \tag{1}$$

$$u_x \frac{\partial u_x}{\partial x} + u_y \frac{\partial u_x}{\partial y} = v \frac{\partial^2 u_x}{\partial y^2} \tag{2}$$

$$\alpha \frac{\partial^2 \theta}{\partial y^2} = \frac{\partial \theta}{\partial t} + u_x \frac{\partial \theta}{\partial x} + u_y \frac{\partial \theta}{\partial y} \tag{3}$$

Where $\theta = T - T_\infty$.

The boundary and initial conditions are

$$u_x = U_\infty, \theta = 0 \; at \; x = 0 \tag{4}$$

$$u_x = u_y = 0 \; at \; y = 0 \tag{5}$$

$$u_x = U_\infty \; at \; y = \delta \tag{6}$$

$$\theta = 0 \; at \; y = \Delta \tag{7}$$

$$\theta = \theta_p(x, t) \; at \; y = 0 \tag{8}$$

Where δ and Δ are the momentum and thermal boundary layer thicknesses, respectively. From analysis of the momentum boundary layer for flow past a flat plate, the momentum boundary layer is given by [1]

$$\delta(x) = 4.64 \sqrt{\frac{vx}{U_\infty}} \tag{9}$$

While the momentum boundary layer thickness δ is independent of the thermal boundary conditions and is known in advance, the thermal boundary layer thickness Δ still needs to be determined separately. Given the nature of the boundary condition at the flat plate considered here, Δ is, in general, a function of both x and t.
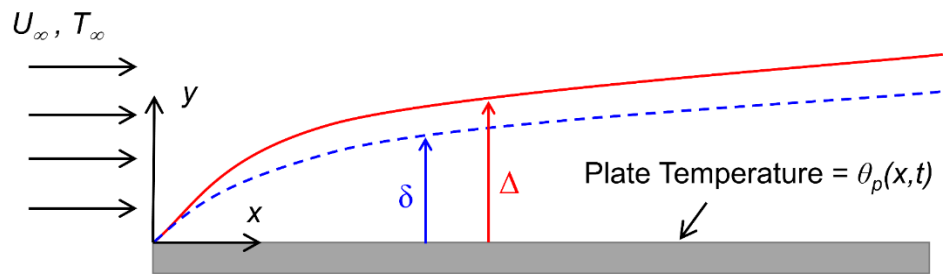
Figure 1. Schematic of laminar, incompressible flow past a thin, flat plate with a given time- and space-varying plate temperature distribution.

103

5-2-2. Solution procedure

A solution for the problem given in equations (1)-(8) is derived using third-order Karman-Pohlhausen polynomials as presented by Kays & Crawford. The analysis discussed here includes transient effects and the impact of space- and time-dependence of the flat plate temperature.

To start with, equation (3) is integrated from $y=0$ to $y=\Delta$, resulting in

$$\frac{\partial}{\partial t}\int_0^\Delta \theta dy + \frac{\partial}{\partial x}\int_0^\Delta u_x\theta dy = -\alpha \left(\frac{\partial\theta}{\partial y}\right)_{y=0} \qquad (10)$$

Third-order polynomial forms for velocity and temperature fields are determined based on the Karman-Pohlhausen approach. Third-order Karman-Pohlhausen polynomials have been widely used in the literature [1,20] and have been shown to facilitate analytical modeling while also offering excellent accuracy [1]. In order to determine these Karman-Pohlhausen polynomials, boundary conditions given by equations (5) and (6) for velocity and equations (7) and (8) for temperature are considered. In addition, as is common in the Karman-Pohlhausen approach, first derivative of velocity and temperature at the edge of the respective boundary layer and the second derivative at the plate are taken to be zero. With these boundary conditions, coefficients in the polynomial forms for velocity and temperature are determined. The final result is

$$\frac{u_x(x,y,t)}{U_\infty} = \frac{3}{2}\frac{y}{\delta} - \frac{1}{2}\left(\frac{y}{\delta}\right)^3 \qquad (11)$$

and

$$\frac{\theta(x,y,t)}{\theta_p} = 1 - \frac{3}{2}\frac{y}{\Delta} + \frac{1}{2}\left(\frac{y}{\Delta}\right)^3 \qquad (12)$$

where $\theta_p(x,t) = T_p(x,t) - T_\infty$.

Equation (10) can be simplified by introducing the enthalpy thickness of the thermal boundary layer, Δ_2, defined as

$$\Delta_2 = \frac{1}{U_\infty \theta_p} \frac{\partial}{\partial x} \int_0^\Delta u_x \theta \, dy \tag{13}$$

This results in simplification of equation (10) as follows:

$$\frac{1}{U_\infty \theta_p} \frac{\partial}{\partial t} \int_0^\Delta \theta \, dy + \frac{d\Delta_2}{dx} + \frac{\Delta_2}{\theta_p} \frac{d\theta_p}{dx} = \frac{\alpha}{U_\infty \theta_p} \left(\frac{\partial \theta}{\partial y} \right)_{y=0} \tag{14}$$

Now, using equations (11) and (12), Δ_2 can be expressed as [1]

$$\Delta_2 = \frac{1}{U_\infty \theta_p} \frac{\partial}{\partial x} \int_0^\Delta u_x \theta \, dy = \frac{3}{20} \frac{\Delta^2}{\delta} - \frac{3}{280} \frac{\Delta^4}{\delta^3} \tag{15}$$

Using equation (12), the right hand side of equation (13) and the first term on the left hand side can be evaluated as

$$\frac{\alpha}{U_\infty \theta_p} \left(\frac{\partial \theta}{\partial y} \right)_{y=0} = \frac{3}{2} \frac{\alpha}{U_\infty \theta_p} \left(\frac{\partial \theta}{\partial y} \right)_{y=0} \tag{16}$$

$$\frac{1}{U_\infty \theta_p} \frac{\partial}{\partial t} \int_0^\Delta \theta \, dy = \frac{3}{8} \frac{1}{U_\infty \theta_p} \frac{\partial}{\partial t} (\Delta \theta_p) \tag{17}$$

Combining equations (16) and (17) into the integral form of the energy equation (14) and simplifying, one may obtain

$$\frac{3}{20} r^2 \frac{d\delta}{dx} + \frac{3}{10} r\delta \frac{\partial r}{\partial x} + \left[\frac{3}{20} r^2 - \frac{3}{280} r^4 \right] \delta \frac{1}{\theta_p} \frac{\partial \theta_p}{\partial x} + \frac{3}{8} \frac{\delta}{U_\infty} \frac{\partial r}{\partial t} = \frac{3}{2} \frac{\alpha}{U_\infty \Delta} \tag{18}$$

Note that equation (18) has been expressed in terms of $r = \Delta/\delta$ for convenience.

The r^4 term in the brackets is neglected compared to the r^2 term, assuming that $r<1$, which occurs if $Pr<1$, i.e., the thermal boundary layer grows slower than the momentum boundary layer. Further rearrangement of equation (18) results in

$$r^3 + 4xr^2 \frac{\partial r}{\partial x} + 2xr^3 \frac{1}{\theta_p} \frac{\partial \theta_p}{\partial x} + 5 \frac{x}{U_\infty} \left[\frac{r^2}{\theta_p} \frac{\partial \theta_p}{\partial t} + r \frac{\partial r}{\partial t} \right] = \frac{13}{14} Pr \tag{19}$$

Equation (19) is a first-order partial differential equation for *r(x,t)* that must be solved to determine *r(x,t)*, and hence the thermal boundary layer thickness. The associated initial and boundary conditions are

$$r = 0 \; at \; t = 0 \tag{20}$$

$$r = 0 \; at \; x = 0 \tag{21}$$

Once solved, the thermal boundary layer thickness can be written using the expression for δ given by equation (9) in the definition of *r*. Finally, the heat flux at the plate is given by

$$q_p(x,t) = -k \left(\frac{\partial \theta}{\partial y}\right)_{y=0} = \frac{3}{2} \frac{k\theta_p(x,t)}{\left[4.64 \sqrt{\frac{\nu x}{U_\infty}}\right] r(x,t)} \tag{22}$$

Note that the $\frac{\partial \theta_p}{\partial x}$ term in equation (19) explicitly accounts for the given spatial variation in the plate temperature. While a similar term accounting for variation in θ_p with time is not present in equation (19), regardless, the variation in θ_p with time is accounted for when calculating the heat flux $q_p(x,t)$ using equation (22) based on the solution for *r(x,t)*.

As is the case with most external flow problems, equation (15) is unlikely to have a closed-form analytical solution. A numerical solution for equation (15) may be sought, following which, the wall heat flux can be determined from equation (18). To obtain a numerical solution, it is helpful to write equation (19) alternatively as

$$C(r,x,t)\frac{\partial r}{\partial t} + D(r,x,t)\frac{\partial r}{\partial x} = E(r,x,t) \tag{23}$$

where

$$C(r,x,t) = \frac{25xr}{3U_\infty} \tag{24}$$

$$D(r,x,t) = 4r^2x \tag{25}$$

$$E(r, x, t) = \frac{13}{14}Pr - r^3 - 2r^3x\frac{1}{\theta_p}\frac{\partial\theta_p}{\partial x} - \frac{5}{U_\infty\theta_p}xr^2\frac{\partial\theta_p}{\partial t} \qquad (26)$$

A numerical solution of equation (23) can be easily computed by discretizing in the x direction, which converts equation (23) into a set of ordinary differential equations in the r as a function of time at each location. These ordinary differential equations are integrated using a three-stage, third-order, Runge-Kutta solver with adaptive timestepping [21]. The initial condition provides the initial state needed for starting the integration process.

5-3. Results and discussion

5-3-1. Special cases

Several special cases of the general problem considered here have been investigated in past work and are of interest for comparison with the general result derived here.

When the plate temperature is a function of space only and the steady state heat flux from the plate is desired, the general result presented in equation (19) reduces to

$$r^3 + 4xr^2\frac{dr}{dx} + 2xr^3\frac{1}{\theta_p}\frac{\partial\theta_p}{\partial x} = \frac{13}{14}Pr \qquad (27)$$

Given a $\theta_p(x)$ distribution, equation (27) can be solved easily. Specifically, for constant plate temperature, the resulting differential equation for $r(x)$ can be obtained by putting $\frac{\partial\theta_p}{\partial x} = 0$ in equation (27), resulting in

$$r^3 + 4xr^2\frac{dr}{dx} = \frac{13}{14}Pr \qquad (28)$$

107

This is identical to the result for this special case presented in Kays & Crawford. Note that this equation was derived for the constant temperature flat plate by two independent methods – by directly solving the governing differential equation obtained from energy conservation, and by solving the integral form of the energy equation.

Several other results for special cases are also available for comparison with the present work. For example, the classical approach for solving the problem in which the plate temperature varying with x is by linear superimposition of solutions for multiple constant plate temperature problems with an unheated length [1]. This solution is given by

$$Nu_x(x) = \int_0^x 0.332 Pr^{1/3} Re_x^{1/2} \left[1 - \left(\frac{\xi}{x}\right)^{3/4}\right]^{-1/3} \frac{1}{\theta_p} \frac{\partial \theta_p}{\partial x} d\xi \tag{29}$$

Where $Re_x = \frac{U_\infty x}{\nu}$ is the Reynolds number.

Specifically, for a linear variation, $\theta_p = (a + bx)$, it can be shown that

$$Nu_x(x) = 0.332 Pr^{1/3} Re_x^{1/2} \frac{(a + 1.612bx)}{(a + bx)} \tag{30}$$

Finally, for the simplest case of constant plate temperature, the resulting Nusselt number is

$$Nu_x(x) = 0.332 Pr^{1/3} Re_x^{1/2} \tag{31}$$

Solutions for these special cases can be compared with the present work by solving equation (27) derived in this work.

In contrast with the special cases above, in which the plate temperature is a function of x only, another class of special cases is one in which the plate temperature is a function of time only. These

problems have been discussed in a number of past papers, the results of which can be compared with results from the present work. In the present work, consideration of plate temperature as a function of time alone results in minor simplification in the independent term of the governing equation for $r(x,t)$. Specifically, putting $\frac{\partial \theta_p}{\partial x} = 0$ and preserving the transient terms in equation (19) results in

$$F(r,x,t) = \frac{13}{14}Pr - r^3 - 2r^3x\frac{1}{\theta_p}\frac{\partial \theta_p}{\partial x} - \frac{5}{U_\infty \theta_p}r\frac{\partial \theta_p}{\partial t} \tag{32}$$

In contrast, a special case where the plate temperature is a step function of time at $t=0$ has been discussed by Cess [5]. The resulting plate heat flux is

$$q_p(x,t) = k\sqrt{Re_x}\frac{\theta_p}{x}\left[0.5642\sqrt{\frac{Pr}{\tau}}e^{-0.4858\tau} - 0.02076\tau e^{-0.3182\tau}\right. \tag{33}$$

$$\left. + 0.2957\,\mathrm{erf}\left(\sqrt{0.4858\tau}\right)\right]$$

where $\tau = \frac{U_\infty t}{x}$.

For an arbitrary variation in the plate temperature with time, the resulting plate heat flux is given by

$$q_p(x,t) = k\frac{\sqrt{Re_x}}{x}\int_0^\lambda \left[0.5642\sqrt{\frac{Pr}{\lambda}}\,e^{-0.4858\lambda} - 0.02076\tau e^{-0.3182\lambda} \right. \tag{34}$$

$$\left. + 0.2957\,\text{erf}\left(\sqrt{0.4858\lambda}\right) \right]$$

Finally, for the specific case of linear change in plate temperature, $\theta_p = Mt$, the resulting heat flux from the plate is given by

$$\frac{q_p(x,t)}{q_{qs}} = \begin{cases} 2\sqrt{\dfrac{\tau_a}{\tau}}, & \tau \leq \tau_a \\ 1 + \dfrac{\tau_a}{\tau}, & \tau \geq \tau_a \end{cases} \tag{35}$$

where $q_{qs} = 0.2957k\frac{\sqrt{Re_x}}{x}\theta_p$ and $\tau_a = 2.62$ for the case of air (Pr=0.72).

Each of these special cases can be compared with results from the more general model developed in this work.

5-3-2. Comparison with results for special cases

Figure 2 presents a comparison between the present work and the well-known Nusselt number relationship for the special case of a constant temperature plate. When the plate temperature does not change with x or t, the general result presented in Section 2 can be considerably simplified, as discussed in Section 3.1. The resulting Nusselt number distribution is very close to the standard isothermal flat plate result [1], as plotted in Figure 2 for $\theta_p = 100$. The good agreement is to be expected, since Section 3.2 shows that the results from the present work reduce to the well-known differential equation for a constant temperature plate [1].
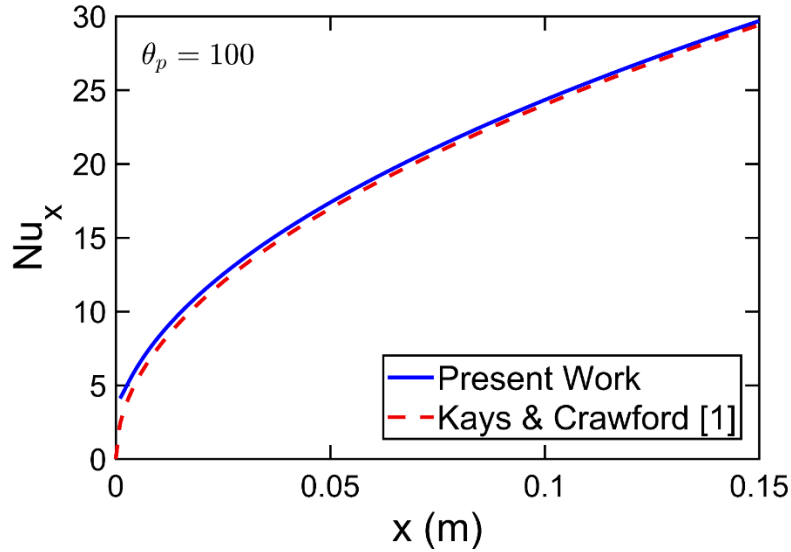
Figure 2. Nusselt number comparison of present work with Kays & Crawford [1] for the special steady-state case of constant plate temperature, $\theta_p = 100$.

.

Comparison with past work for the special case of spatially-varying plate temperature in steady state is considered next. Two specific distributions that have been used in past work are considered for this comparison. Figures 3(a) and 3(b) plot the Nusselt number distribution for linear $(\theta_p = 10x + 100)$ and exponentially-decaying $(\theta_p = \exp(-x) - 1)$ temperature distributions, respectively. In both cases, there is excellent agreement with equation (28) taken from Kays & Crawford. As expected, the Nusselt number, which represents the ratio of plate heat flux to plate temperature multiplied by x increases with x. In Figure 3(a), this is primarily because the plate temperature increases with x. On the other hand, in Figure 3(b), the heat flux reduces with increasing x, but the Nusselt number curve still increases due to the presence of the x term in the expression for Nu.
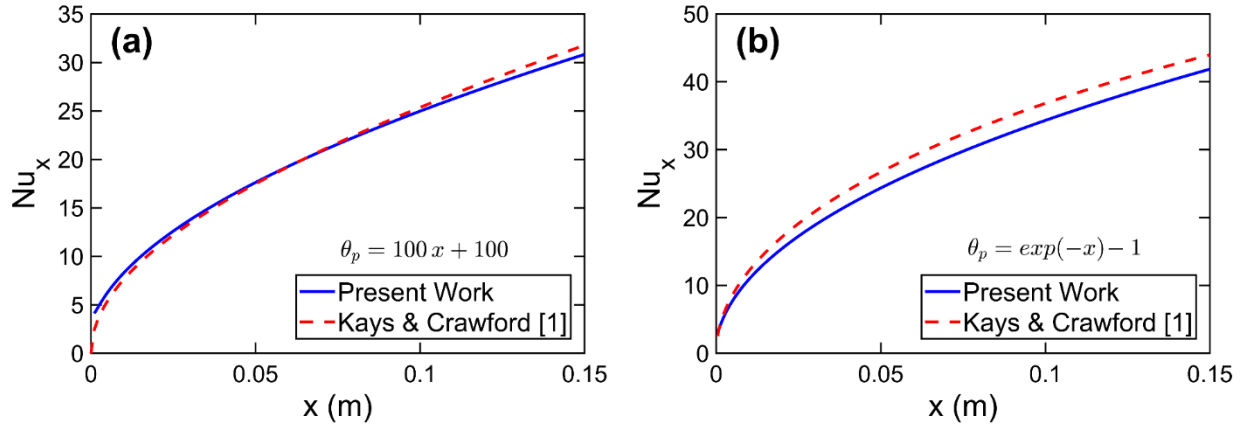
Figure 3. Nusselt number comparison of present work with Kays & Crawford [1] for the special case of steady state, space-dependent heat flux: (a) linear θ_p =(10x+100), (b) non-linear θ_p =exp(-x)-1. Note that x is in m.

Comparison of the present work with past work for transient cases is considered next. Several papers have presented solutions of the flat plate problem with time-varying plate temperature. Comparison with Cess [5] for the case of a step change in plate temperature at t=0 is presented in Figure 4 for $\theta_p = 100$. This problem corresponds to the transient component of the standard, constant plate temperature problem. In this case, Figure 4 plots the Nusselt number distribution at multiple times. At each time, there is good agreement between the present work and Cess. At small times, the Nusselt number rises rapidly with x, because of a rapid increase in the plate heat flux in response to the sudden increase in plate temperature. As time passes, the plate heat flux decreases and becomes steady, particularly at large x, and the Nusselt number curve approaches its steady state form. The t=0.5 s plot in Figure 4 is very close to the steady state plot presented earlier in Figure 2 for the same plate temperature.
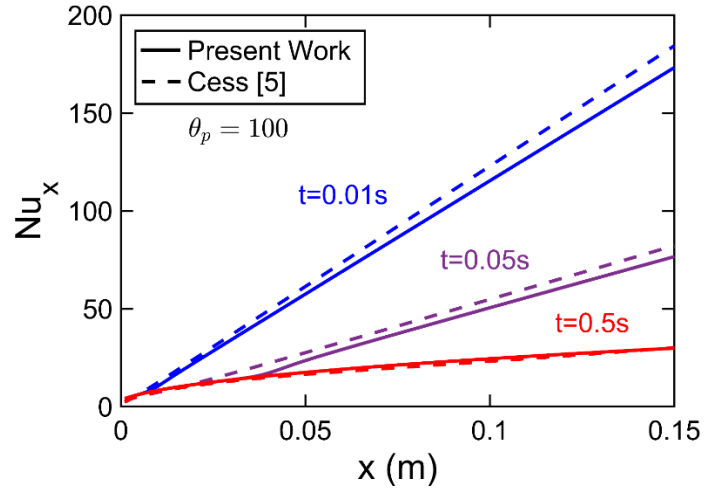
Figure 4. Nusselt number comparison of present work with Cess [5] for uniform plate temperature with step-change at t=0, i.e., θ_p =100, t>0. Comparison is presented at multiple times.

Finally, comparison with past work is presented for a more complicated transient problem, in which, the plate temperature increases linearly with time. For $\theta_p = 100t$, Figure 5 plots the plate heat flux distribution on the plate at two different times. Constant, room-temperature properties of air are assumed in this and subsequent Figures. Results from the present work are compared with Cess [5], as given in equation (34) in Section 3.1. There is very good agreement at both times. In this case, there is no sudden jump in the plate temperature. At any location, the Nusselt number decays with x because of greater convective heat transfer near the leading edge of the plate, as expected, and as seen in Figure 5(a). As the plate temperature rises gradually with time, the plate heat flux at any given location increases as expected and as shown in Figure 5(b). At any given time, the plate heat flux decays with x, which is.

Note that papers such as Cess [5] accounted only for variation in the plate temperature with time, i.e., the plate temperature was assumed to be spatially uniform at any given time. On the other hand, the present work generalizes this to a situation where the plate temperature may vary arbitrarily in both space and time.

113
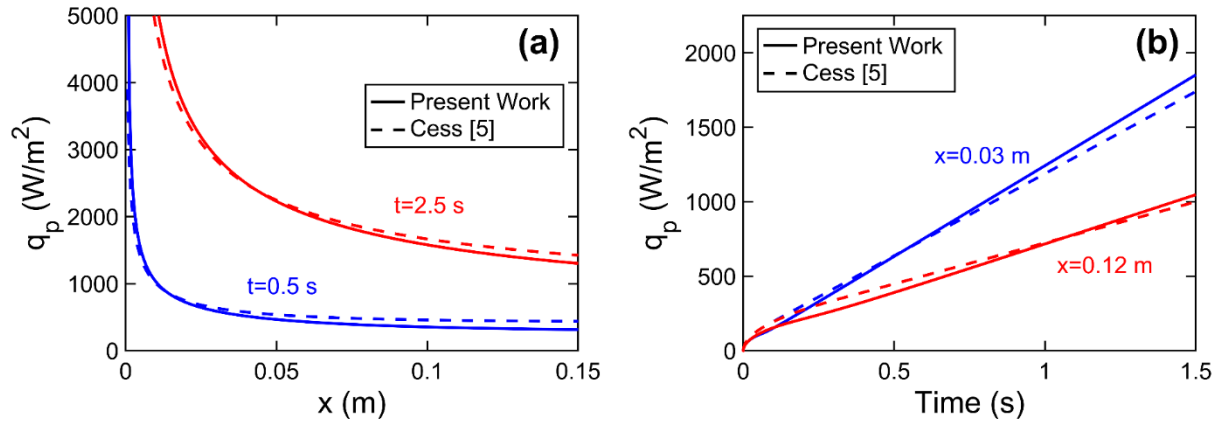
Figure 5. Plate heat flux comparison of present work with Cess [5] for uniform plate temperature that increases linearly with time, $\theta_p = 100t$, t>0. Comparison is presented at two different times.

5-3-3. Comparison with numerical simulations

Results from the present work are also compared with finite-element numerical simulations carried out in a computational software tool. The flow domain is modeled with a rectangular 0.15m by 0.15m 2D surface. A quadrilateral mesh network with total number of 30000 elements is constructed with largest element size of 0.001 m. Due to boundary layer effect, the mesh grid is refined in y direction close to the plate. Grid independency is ensured by verifying minimal change in simulation results with different mesh sizes. The comparison is carried out for a plate temperature that varies in both space and time. Two specific plate temperature functions, $\theta_p = 200x + 400t + 50$ and $\theta_p = 10\sqrt{x} + 50\sqrt{t} + 20$ are considered in Figures 6(a) and 6(b), respectively. In both cases, the plate heat flux is plotted as a function of x at two different times. Figure 6 shows excellent agreement between numerical simulations and the present work for both plate temperature functions. In each case, the plate heat flux decays with x due to the growing thermal boundary layer. Further, the plate heat flux increases with time, which is consistent with the increasing nature of the plate temperature with time. The plate temperature increases more

114

rapidly with time for the first case, which is why, the plate flux is greater for Figure 6(a) than for Figure 6(b). The good agreement with numerical simulations demonstrated in Figure 6 provides additional confidence in the present work.
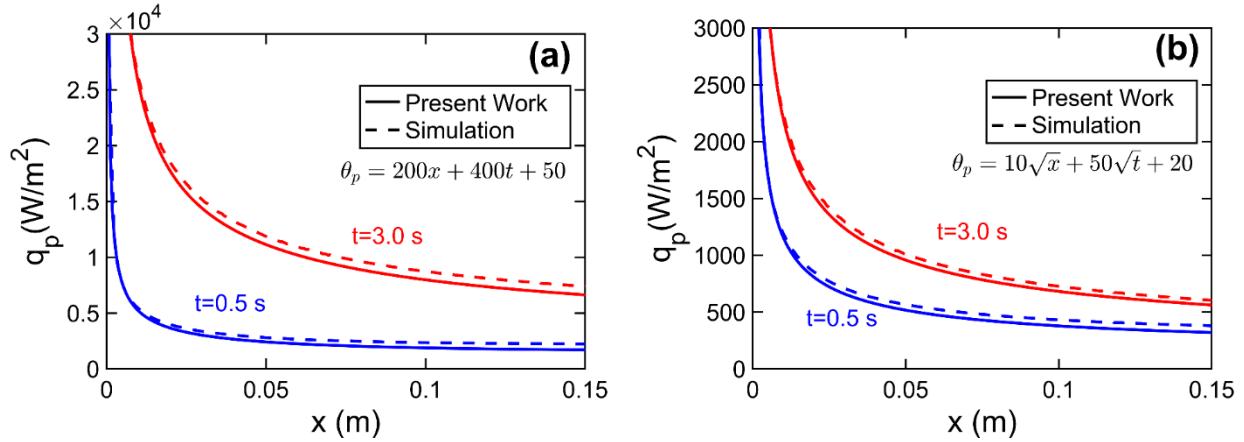
Figure 6. Comparison of the present work with numerical simulations: Plate heat flux as a function of x for two different spatially- and time-varying plate temperature distributions (a) $\theta_p = 200x + 400t + 50$; (b) $\theta_p = 10\sqrt{x} + 50\sqrt{t} + 20$.

5-3-4. Applications of the analytical model

The analytical model is next used to determine the plate heat flux in response to a variety of practical plate temperature distributions that may be encountered in engineering systems. These examples demonstrate the capability of the analytical model to account for a general time- and space-dependent plate heat flux.

The case of the plate heat flux that varies linearly with both time and x is considered first. Specifically, for $\theta_p = 100x + 100t + 10$, Figure 7(a) plots the plate heat flux as a function of x at two different times. A similar plot of plate heat flux as a function of time at two different locations is presented in Figure 7(b). As shown in Figure 7(a), the plate heat flux decays with x, which is consistent with the convective heat transfer being largest in magnitude near the leading

edge, and decaying with x due to boundary layer growth. At a given location, the plate heat flux decreases during a short time period close to t=0, following which, there is a linear increase over time. At large times, the smaller the value of x, the larger is the heat flux. There is a reversal of this trend for a short time close to t=0, which is because, according to the plate temperature distribution, at t=0, the plate suddenly attains a larger temperature at larger value of x. As time passes, however, the effect of boundary layer growth begins to dominate, and there is greater heat flux at lower x.
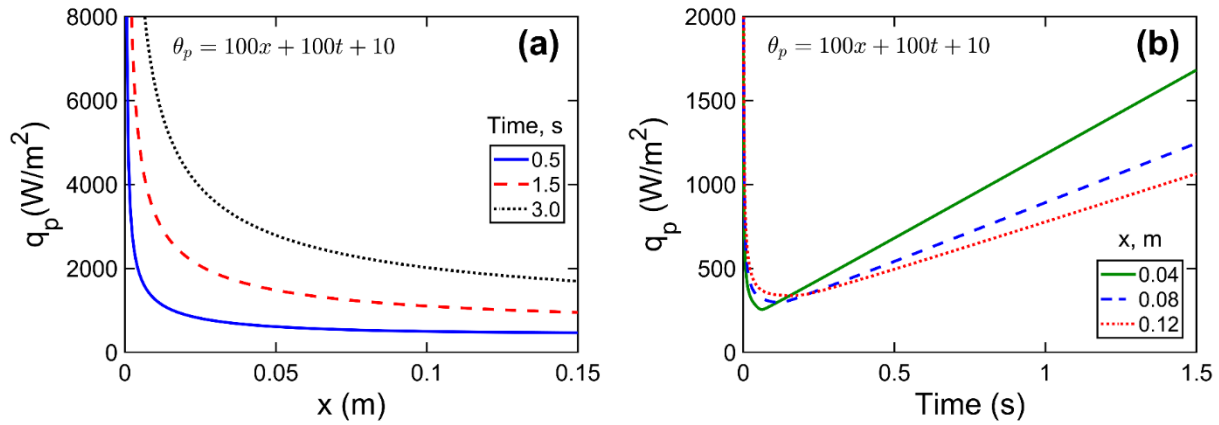
Figure 7. Plate heat flux, q_p as a function of (a) x at different times, and (b) time at different x for a general plate temperature distribution, $\theta_p(x,t) = 100x + 100t + 10$.

Similar results for a plate temperature distribution given by for $\theta_p = 100\sqrt{x} + 100\sqrt{t} + 10$ are presented in Figures 8(a) and 8(b). In this case, the plate temperature increase with x and time is less rapid that the previous case, which is why, the decay in heat flux with x shown in Figure 8(a) is less sharp than the similar plot for the previous case, shown in Figure 7(a). After a short initial period, during which, the effect of the imposed plate temperature distribution dominates over the boundary layer growth, there is a gradual increase in heat flux with time, as shown in Figure 8(b). This increase is slower than linear, which is consistent with the $\sqrt{t}$-dependence of plate temperature in this case, compared to the linear dependence considered in the previous case.
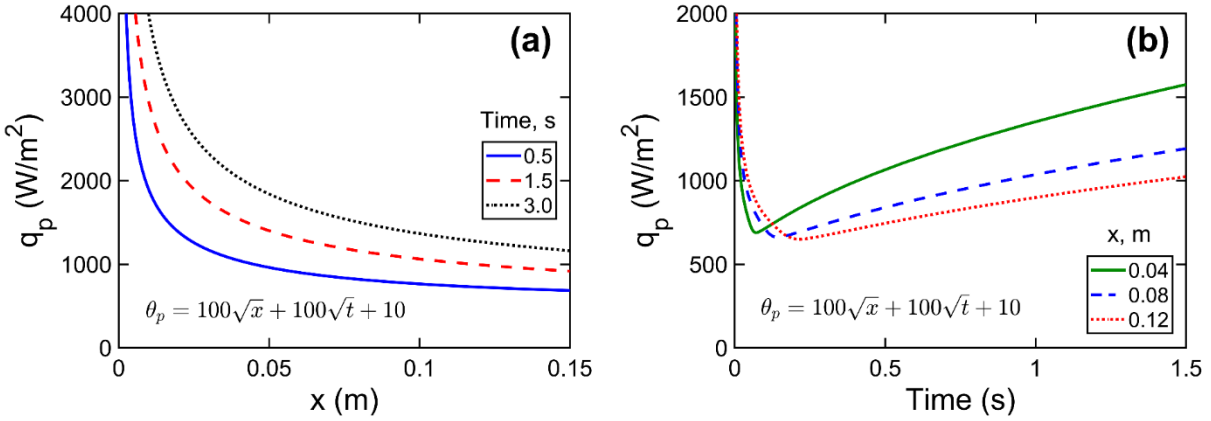
Figure 8. Plate heat flux, q_p as a function of (a) x at different times, and (b) time at different x for a general plate temperature distribution, $\theta_p(x,t) = 100\sqrt{x} + 100\sqrt{t} + 10$.

The next Figure considers step function change in the plate temperature distribution. First, a step function in time is considered, wherein $\theta_p = 50\sqrt{x} + 20$ for $t \leq 0.5s$ and $\theta_p(x,t) = 400\sqrt{x} + 20$ afterwards. Figures 9(a) and 9(b) plot spatial distribution of heat flux at two different times before and after the step change, and variation of heat flux with time at two different locations, respectively. In Figure 9(a), there is a gradual reduction in heat flux with x, which is consistent with boundary layer growth, both before and after the step change. Also, the plate heat flux is greater at t=0.7s compared to t=0.3s, which is because of the jump in heat flux that occurs at t=0.5s. In Figure 9(b), the heat flux shows an initial sharp decrease towards a steady state value. However, due to the step change in plate temperature at t=0.5 s, there is a corresponding jump in plate heat flux, which then attains a steady state value, as shown in Figure 9(b). At very small times, the heat flux at x=0.1 m is greater than at x=0.05 m, because of the greater plate temperature at x=0.1 m. However, this effect is quickly dominated by the thicker boundary layer at x=0.1 m, due to which, the heat flux at x=0.1 m eventually becomes lower than at x=0.05 m.
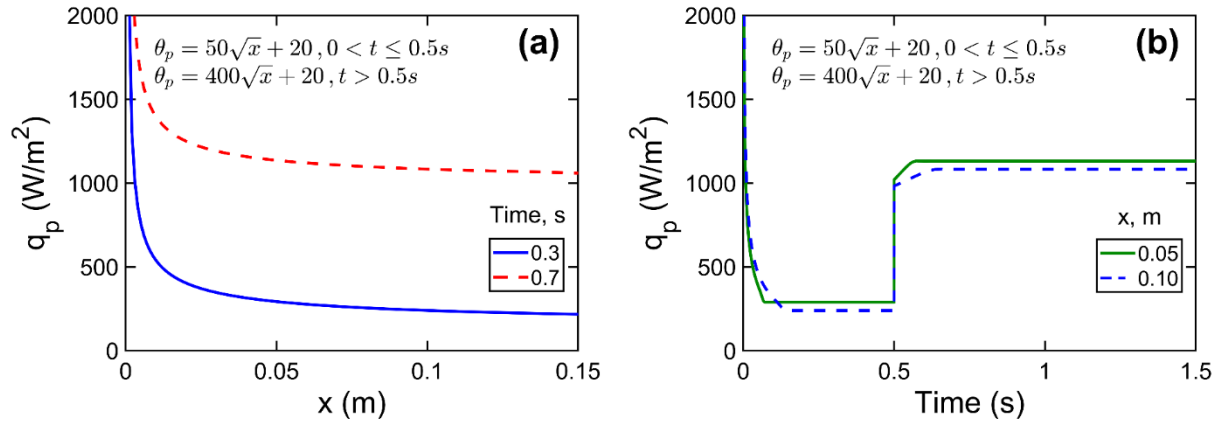
Figure 9. Plate heat flux, q_p as a function of (a) x at different times, and (b) time at different x for a general plate temperature distribution, $\theta_p(x,t) = 50\sqrt{x} + 20$ for $t \leq 0.5s$ and $\theta_p(x,t) = 400\sqrt{x} + 20$ for $t > 0.5s$.

5-4. Conclusions

The generalized analysis presented in this work accounts for variation in the plate temperature with both time and space, and therefore, may be more appropriate for realistic scenarios compared to past models in which the plate temperature is treated to be either time-dependent or space-dependent, but not both. Comparison of results from the present model with past work for special cases increases confidence in the present model. Several cases are also presented to demonstrate the capability of the present model to predict the plate heat flux in a variety of complicated scenarios.

The present model is based on solving the integral form of the governing equations using third-order Karman-Pohlhausen polynomials. This approach has been shown to result in good accuracy in several past papers. It is also important to be cognizant of other key assumptions made in this present work, including temperature-independent properties, laminar flow and fully developed velocity field as well as zero thermal resistance/capacitance of the flat plate.

In addition to contributing towards the fundamental theoretical understanding of convective heat transfer, it is expected that the present work may also help in the design and optimization of practical and realistic heat transfer devices and systems.

5-5. Nomenclature

k	thermal conductivity, $\text{Wm}^{-1}\text{K}^{-1}$
q	heat flux, Wm^{-2}
Pr	Prandtl number
t	time, s
T	temperature, K
T_∞	freestream temperature, K
u	velocity, ms^{-1}
U_∞	freestream velocity, ms^{-1}
α	thermal diffusivity, m^2s^{-1}
δ	momentum boundary layer thickness, m
Δ	thermal boundary layer thickness, m
Δ_2	enthalpy thickness of the thermal boundary layer, m
ν	kinematic viscosity, m^2s^{-1}
θ	temperature field relative to ambient temperature, K

Subscripts

x	direction along with flat plate

y   direction normal to the flat plate

p   plate

5-6. References

 [1] '*Convective heat and mass transfer,*' W.M. Kays, M.E. Crawford, B. Weigand, McGraw-Hill Higher Education, Boston, 2005.

[2] J.H. Lienhard, 'Heat Transfer in Flat-Plate Boundary Layers: A Correlation for Laminar, Transitional, and Turbulent Flow', *J. Heat Transf.*, **142**, pp. 061805:1-14, 2020.

[3] J.S. Klein, M. Tribus, 'Forced convection from nonisothermal surfaces,' in: Proc. Heat Transfer Symp., University of Michigan Engineering Research Institute, 1952.

[4] J.K. Eaton, 'The Discrete Green's Function for Convective Heat Transfer—Part 1: Definition and Physical Understanding,' *J. Heat Transf.*, **142**, pp. 102101:1-9, 2020.

[5] R.D. Cess, 'Heat transfer to laminar flow across a flat plate with a non-steady surface temperature,' *J. Heat Transf.*, **83**, pp. 274-279, 1961.

[6] B.T. Chao, L.S. Cheema, 'Unsteady heat transfer in laminar boundary layer over a flat plate,' *Int. J. Heat Mass Transf.*, **11**, pp. 1311-1324, 1968.

[7] M. Lachi, M. Rebay, E.C. Mladin, J. Padet, 'Alternative models for transient convection heat transfer in external flows over a plate exposed to a variable heat flux,' *Int. J. Therm. Sci.*, **43**, pp. 809–816, 2004.

[8] G. Polidori, J. Padet, 'Transient laminar forced convection with arbitrary variation in the wall heat flux,' *Heat and Mass Transf.*, **38**, pp. 301–307, 2002.

[9] '*Heat and Mass Transfer,*' E.R.G. Eckert, R.M. Drake, McGraw Hill, New York, 1959, ISBN: 9780070189249

[10] D.C. Baxter, W.C. Reynolds, 'Fundamental solutions for heat transfer from nonisothermal flat plates,' *J. Aerosci.*, **25**, pp. 403-404, 1958.

[11] A. Mostafavi, A. Jain, 'Unsteady convective heat transfer from a flat plate with heat flux that varies in space and time,' *Int. J. Heat Mass Transfer*, **172**, pp. 121084:1-8, 2021.

[12] '*Computational Heat Transfer,*' Y. Jaluria, K.E. Torrance, CRC Press, 2002, ISBN: 9781560324775

[13] D.K. Gartling, 'Convective heat transfer analysis by the finite element method,' *Computer Methods in Appl. Mechanics & Eng.*, **12**, pp. 365-382, 1977.

[14] L. He, M.L.G. Oldfield, 'Unsteady Conjugate Heat Transfer Modeling.' *ASME. J. Turbomach.*, **133**, pp. 031022, 2011.

[15] '*Conjugate Problems in Convective Heat Transfer*,' A.S. Dorfman, 1st Ed., CRC Press, 2018. ISBN: 978-1138372719

[16] H. Blasius, 'Grenzschichten in Flüssigkeiten mit kleiner Reibung.' *Zeits. f. Math. u. Phys*, **56**, pp. 1-37, 1908.

[17] G. Hed, R. Bellander, 'Mathematical modelling of PCM air heat exchanger,' *Energy Build.*, **38**, pp. 82–89, 2006.

[18] D. Chalise, K. Shah, R. Prasher, A. Jain, 'Conjugate heat transfer analysis of thermal management of a Li-ion battery pack,' *ASME J. Electrochem. Energy Conversion & Storage*, **15**, pp. 011008:1-8, 2018.

[19] D.J. Correa, J.L. Marchetti, 'Dynamic simulation of shell-and-tube heat exchangers,' *Heat Transf. Eng.*, **8**, pp. 50-59, 1987.

[20] '*Heat Convection*,' L. Jiji, Springer-Verlag Berlin Heidelberg, 2009. ISBN: 978-3-642-02970-7

[21] https://www.mathworks.com/help/matlab/ref/ode23.html, accessed Dec 21, 2020.

Chapter 6

Analytical modeling of conjugate heat transfer between a bed of phase change material and laminar convective flow

Under Preparation for Journal Submission

6-1. Introduction

Phase change materials (PCMs) are used commonly for latent energy storage [1] and thermal management [2]. For example, excess thermal energy produced in a Concentrated Solar Power (CSP) plant is often stored in the form of latent heat to be utilized when direct solar energy is not available. Phase change heat transfer has also been investigated for transient thermal management of engineering systems such as electronics [2] and Li-ion cells [3].

Understanding the nature of heat transfer during phase change in a PCM is critical for improving efficiency of latent energy storage. This involves heat transfer both within the PCM and between the PCM and the surroundings. A significant amount of experimental investigation has been reported on heat transfer enhancement in latent energy storage systems by mechanisms such as improving thermal conductivity of the PCM [4], or providing fins within the PCM [5-7]. A number of analytical and numerical tools have also been developed to model and optimize phase change processes, particularly the interaction between the PCM and the surroundings to/from where heat transfer occurs. On one hand, fundamental heat transfer modeling of the phase change process under various boundary conditions has been carried out. For example, perturbation method based solutions of phase change problems under time-dependent temperature [8] and heat flux [9] boundary conditions have been developed. Analytical and numerical models for the impact of fins on the rate of latent energy storage have been developed [5], and an optimal fin size has been demonstrated [6]. The impact of thermal properties such as thermal conductivity and heat capacity has also been investigated [10]. Most of these papers that analyze heat transfer only in the PCM represent the surroundings in the form of an appropriate boundary condition. On the other hand, substantial literature also exists on theoretical and numerical modeling of practical latent heat energy storage geometries. For example, the problem of heat exchange between PCM in a tube

and air flow over the tube has been analyzed [11,12]. Semi-analytical models have been proposed for flat plate latent heat storage, in which convective heat transfer between a flat bed of PCM and fluid flow over the bed is responsible for latent heat storage [13-15]. Numerical modeling has been used to analyze the impact of fins in a tubular latent heat energy storage unit [16]. Numerical modeling of phase change energy storage in spherical PCMs has also been presented [17].

Amongst the various geometries for a latent heat energy storage system outlined above, the flat bed geometry is one of the simplest and most fundamental. As shown schematically in Figure 1, in this geometry, convective heat transfer due to fluid flow over one or more flat PCM beds is responsible for phase change and latent heat storage. Despite its simplicity, heat transfer modeling of this geometry is not straight-forward. On one hand, the phase change process occurring in the bed is non-linear in nature [18]. On the other hand, fluid flow and convective heat transfer over the bed is also, in general, non-linear [19]. In general, the convective heat transfer coefficient between the bed and fluid is a function of both space and time, and is not known in advance because neither the temperature nor the heat flux at the PCM-fluid interface is known. While a few papers have attempted to develop an analytical heat transfer model for a flat bed phase change system [14,15], these papers assume certain expressions for the convective heat transfer coefficients corresponding to isothermal and constant flux boundary conditions, which is clearly not valid for the boundary across which phase change occurs. In order to overcome these shortcomings, it is important to treat the PCM-fluid heat transfer problem as a conjugate problem, with convective heat transfer in the fluid and phase change heat transfer in the PCM. A conjugate heat transfer analysis – which in general is considerably complicated [20] – is expected to result in the phase change front as well as convective heat transfer coefficient at the interface as functions of space and time.

An iterative approach has been proposed in the recent past to solve conjugate heat transfer problems [21]. The iterative approach assumes a temperature distribution at the interface between the two problems, and solves the heat transfer problem in one of the regions by using the temperature distribution as a boundary condition for that region. The resulting interfacial heat flux distribution is used to solve the heat transfer problem in the other region, which is then used to update the interfacial temperature distribution. Several iterations of this process have been shown to result in a converged temperature distribution. This approach has been used for solving steady-state [21] and transient problems [22], including those including phase change heat transfer [23].

This paper presents analytical heat transfer modeling of a flat bed phase change system, in which phase change is driven by convective flow past the PCM bed. This work overcomes the shortcomings of past attempts at solving this problem by deriving an exact solution without assuming an expression for the convective heat transfer coefficient between the PCM bed and fluid flow. An iterative approach is used to solve the phase change and convective heat transfer problems. While the phase change problem is solved using a perturbation method, the convective heat transfer problem is solved by representing the flow velocity and temperature distributions using Karman-Pohlhausen polynomials [19,24]. Convergence of the temperature distribution over multiple iterations is demonstrated, and is used to predict the evolution of the phase change front in the PCM over time. Good agreement with finite-element simulations is demonstrated. The resulting analytical model is used to understand the impact of various problem parameters on the performance of latent heat energy storage.

6-2. Mathematical modeling

6-2-1. Problem definition

Figure 1(a) shows a schematic of a flat bed latent heat storage system, in which a fluid flows over multiple PCM beds and convective heat transfer between the two results in phase change energy storage driven by melting or solidification of the PCM bed. Due to symmetry in the geometry, a representative unit cell shown in Figure 1(b) may be considered for analysis. A number of assumptions are made to facilitate analysis of this problem. On the fluid side, laminar flow is assumed, with a uniform freestream velocity U_∞ and temperature T_∞. All properties are assumed to be independent of temperature. Viscous dissipation is assumed to be negligible. On the PCM side, phase change is assumed to be one-dimensional, i.e., there is no heat transfer within the PCM in the x direction, so that temperature distribution and location of the phase change front at any x in the PCM is assumed to be influenced only by the boundary condition at that x, and not by the boundary condition at other locations. Heat flow in the PCM is assumed to be one-dimensional. The plate length is L. Similar to the fluid, PCM thermal properties are also assumed to be independent of temperature. The PCM is assumed to be initially at its solid phase at its melting temperature T_m. Convection in the liquid phase is neglected. Finally, it is also assumed that the fluid flow and PCM are separated by a thin plate of negligible thermal resistance and capacitance. The case of $T_\infty > T_m$ is considered here, leading to heat flow into the PCM and propagation of the melting front into the PCM over time. The opposite case of freezing of liquid PCM by flow of a cold fluid can also be analyzed using the techniques discussed here.

Based on the assumptions listed above, the momentum and energy conservation equations governing the velocity and temperature fields in the fluid flow are given by

$$\frac{\partial u}{\partial x} + \frac{\partial v}{\partial y} = 0 \qquad (1)$$

$$u\frac{\partial u}{\partial x} + v\frac{\partial u}{\partial y} = \nu_f \frac{\partial^2 u}{\partial y^2} \qquad (2)$$

$$\alpha_f \frac{\partial^2 T_f}{\partial y^2} = \frac{\partial T_f}{\partial t} + u\frac{\partial T_f}{\partial x} + v\frac{\partial T_f}{\partial y} \qquad (3)$$

The associated boundary conditions are

$$u = U_\infty; \; T_f = T_\infty \; at \; x = 0 \qquad (4)$$

$$u = 0; v = 0 \; at \; y = 0 \qquad (5)$$

$$u = U_\infty \; at \; y \geq \delta \qquad (6)$$

$$T_f = T_\infty \; at \; y \geq \delta_t \qquad (7)$$

The governing energy conservation equation on the PCM side is given by

$$\alpha_p \frac{\partial^2 T_p}{\partial y^2} = \frac{\partial T_p}{\partial t} \qquad (8)$$

with

$$T_p = T_m \; at \; y = y_{LS} \qquad (9)$$

Energy balance at the phase change interface yields the following equation for the evolution of the phase change front location with time

$$\rho L \frac{dy_{LS}}{dt} = -k_p \frac{\partial \theta_p}{\partial y} \ at \ y = y_{LS} \qquad (10)$$

In addition to the equations given above, temperature and heat flux conservation apply at the interface. As a result, one may write

$$T_f = T_p = T_s(x,t) at \ y = 0 \qquad (11)$$

and

$$-k_f \frac{\partial T_f}{\partial y} = -k_p \frac{\partial T_p}{\partial y} = q_s(x,t) \ at \ y = 0 \qquad (12)$$

where $T_s(x,t)$ and $q_s(x,t)$ are the temperature and heat flux at the interface plate between the flow and PCM. θ_s and q_s are both functions of time due to the transient nature of the phase change process, and are also both functions of x due to effect of fluid flow in the x direction. For example, it is expected that q_s will be greatest at small x where convective heat transfer due to fluid flow is the greatest. Similarly, it is expected that q_s will reduce over time as the phase change front grows and slows down the rate of further phase change. Note that T_s and q_s are not known in advance.
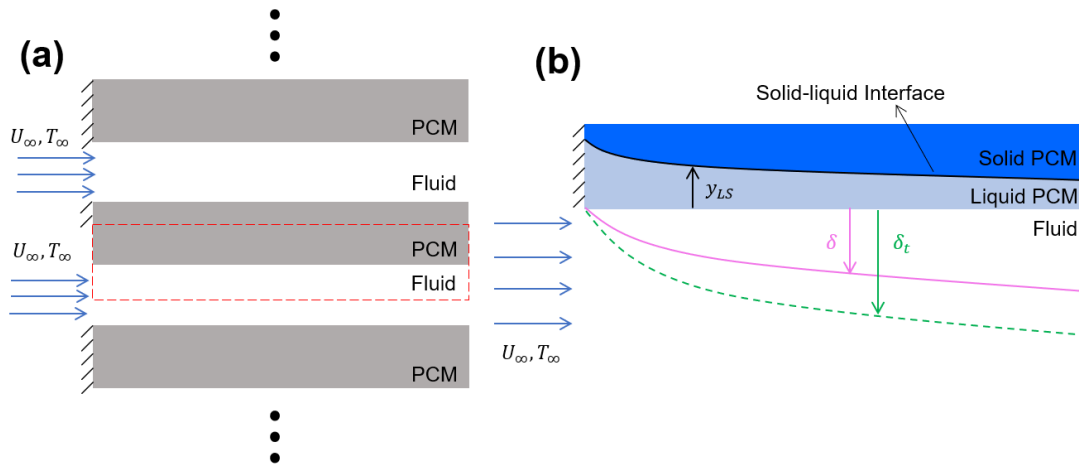
Figure 1. Schematic of (a) overall flat bed storage system comprising several flat PCM beds in parallel; (b) a single PCM-flow system obtained as a symmetry unit cell from.

Finally, both PCM and fluid fields are assumed to be initially at the PCM melting temperature, i.e. $T_f = T_p = T_m$ at $t=0$.

It is helpful to non-dimensionalize the set of equations here to ensure generality of the results. The following non-dimensionalization scheme is followed: $\theta_p = \frac{T_p - T_m}{T_\infty - T_m}$, $\theta_f = \frac{T_\infty - T_f}{T_\infty - T_m}$, $\xi = \frac{x}{L}$, $\eta = \frac{y}{L}$, $\tau = \frac{\alpha_p t}{L^2}$, $\bar{\alpha}_f = \frac{\alpha_f}{\alpha_p}$, $\bar{k}_f = \frac{k_f}{k_p}$, $\bar{u} = \frac{uL}{\alpha_p}$, $\bar{v} = \frac{vL}{\alpha_p}$, $\bar{\delta}_t = \frac{\delta_t}{L}$, $Ste = \frac{C_p(T_\infty - T_m)}{L_p}$. Note that L is an arbitrary length scale, which can be taken to be 1. $T_\infty - T_m > 0$ in the present melting problem. Based on this, the non-dimensional equations to solve the temperature field and determine the propagation of the melting front can be expressed as follows: On the fluid side,

$$\frac{\partial \bar{u}}{\partial \xi} + \frac{\partial \bar{v}}{\partial \eta} = 0 \tag{13}$$

$$\bar{u}\frac{\partial \bar{u}}{\partial \xi} + \bar{v}\frac{\partial \bar{u}}{\partial \eta} = Pr \cdot \bar{\alpha}_f \frac{\partial^2 u}{\partial \eta^2} \tag{14}$$

$$\bar{\alpha}_f \frac{\partial^2 \theta_f}{\partial \eta^2} = \frac{\partial \theta_f}{\partial \tau} + \bar{u}\frac{\partial \theta_f}{\partial \xi} + \bar{v}\frac{\partial \theta_f}{\partial \eta} \tag{15}$$

$$\theta_f = 0 \qquad\qquad \eta >= \bar{\delta}_t \tag{16}$$

$$\theta_f = 0; \bar{u} = \bar{U}_\infty \qquad\qquad \xi = 0 \tag{17}$$

where $Pr = \nu_f/\alpha_f$ is the Prandtl number and $\bar{U}_\infty = U_\infty L/\alpha_p$ is the non-dimensional freestream velocity.

On the PCM side,

$$\frac{\partial^2 \theta_p}{\partial \eta^2} = \frac{\partial \theta_p}{\partial \tau} \tag{18}$$

$$\theta_p = 0 \qquad\qquad \eta{=}\eta_{LS} \tag{19}$$

$$-Ste \frac{\partial \theta_p}{\partial \eta} = \frac{d\eta_{LS}}{d\tau} \qquad\qquad \eta{=}\eta_{LS} \tag{20}$$

Where $\eta_{LS} = y_{LS}/L$ is the non-dimensional location of the phase change front.

Finally, at the PCM-fluid interface,

$$\theta_f = \theta_s; \ \theta_p = 1 - \theta_s \qquad\qquad at \ \eta = 0 \tag{21}$$

$$-\bar{k}_f \frac{\partial \theta_f}{\partial \eta} = -\frac{\partial \theta_p}{\partial \eta} = G(\xi, \tau) \qquad\qquad at \ \eta = 0 \tag{22}$$

Where $G(\xi, \tau) = \frac{q_s(x,t)L}{k_p(T_\infty - T_m)}$ and $\theta_s(\xi, \tau) = \frac{T_\infty - T_s(x,t)}{T_\infty - T_m}$ are the non-dimensional interface flux and

temperature distributions, respectively.

Equations (13)-(22) fully define the conjugate heat transfer problem considered here. Section 2.4 discusses an iterative approach to solve this problem by dividing it into two sub-problems and utilizing temperature and heat flux conservation at the interface to match the two solutions. This technique utilizes solutions for two sub-problems in the PCM and flow regions, respectively, which are first presented in the next two sub-sections.

6-2-2. Solution of phase change sub-problem

The problem defined in section 2.1 is solved iteratively, making use of two previously-reported techniques to solve the PCM and fluid flow problems separately [9,24]. Figures 2(a) and

130

2(b) show schematics of the two separate sub-problems. Solutions of the two sub-problems are needed to drive the iterative procedure. Solution for the PCM and fluid flow sub-problems are described in this and next sub-section, respectively. The iterative technique that combines these two solutions is discussed in section 2.4.

First, the PCM problem is considered. In this case, the governing equations are given by equations (18)-(20), and the boundary condition at the PCM-flow interface, $\eta = 0$ is given by equation (22). Since heat transfer within the PCM in x direction is neglected, therefore, for any location x, this is a problem of one-dimensional phase change with time-dependent heat flux boundary condition. A perturbation method based solution of this problem has been presented in the literature [k]. Assuming that the Stefan number is small, the perturbation method expresses the temperature distribution in a power series involving Ste. By using the energy balance at the phase change front as well as the time-dependent heat flux boundary condition specified at $\eta = 0$, the following expression for the temperature distribution into the PCM at any location ξ :

$$\theta_p(\eta, \eta_{LS}) = \theta_0(\eta, \eta_{LS}) + Ste \cdot \theta_1(\eta, \eta_{LS}) + Ste^2 \cdot \theta_2(\eta, \eta_{LS}) \tag{23}$$

where

$$\theta_0(\eta, \eta_{LS}) = -G(\eta - \eta_{LS}) \tag{24}$$

$$\theta_1(\eta, \eta_{LS}) = G\left[-\frac{G'}{\eta'_{LS}}\left(\frac{\eta^3 - \eta_{LS}^3}{6}\right) + \left(G(t) + \frac{G'}{\eta'_{LS}}\eta_{LS}\right)\left(\frac{\eta^2 - \eta_{LS}^2}{2}\right)\right] \tag{25}$$

$$\theta_2(\eta, \eta_{LS}) = \frac{A}{20}(\eta^5 - \eta_{LS}^5) + \frac{B}{12}(\eta^4 - \eta_{LS}^4) + \frac{C}{6}(\eta^3 - \eta_{LS}^3) + \frac{D}{2}(\eta^2 - \eta_{LS}^2) \tag{26}$$

$$A = -\frac{1}{6}G\left(\left[\frac{G'}{\eta'_{LS}}\right]^2 + \frac{G''}{(\eta'_{LS})^2}G\right) \tag{27}$$

$$B = \frac{1}{2}G\left(\eta_{LS}\left(\left[\frac{G'}{\eta'_{LS}}\right]^2 + \frac{G''}{(\eta'_{LS})^2}G\right) + 3G\frac{G'}{\eta'_{LS}}\right) \tag{28}$$

$$C = G\frac{G'}{\eta'_{LS}}\left[\eta_{LS}\left(\eta_{LS}\frac{G'}{\eta'_{LS}} + G\right) - \frac{G'}{\eta'_{LS}}\frac{\eta^2_{LS}}{2}\right] \tag{29}$$

$$D = \begin{bmatrix} -G\left(\eta_{LS}\frac{G'}{\eta'_{LS}} + G\right)\left(\eta_{LS}\left(\eta_{LS}\frac{G'}{\eta'_{LS}} + G\right) - \frac{G'}{\eta'_{LS}}\frac{\eta^2_{LS}}{2}\right) + \\ G\left(-2G\frac{G'}{\eta'_{LS}}\eta^2_{LS} - \eta_{LS}G^2 - \frac{1}{3}\eta^3_{LS}\left(\left[\frac{G'}{\eta'_{LS}}\right]^2 + \frac{G''}{(\eta'_{LS})^2}G\right)\right) \end{bmatrix} \tag{30}$$

where $'$ and $''$ refer to differentiation with respect to time.

In equations (24)-(30), the location of the phase change front can be determined by solving the following differential equation numerically

$$\frac{d\eta_{LS}}{d\tau} = -Ste\begin{bmatrix} -G + Ste \times G\left(\left(y_{LS}\frac{G'}{y'_{LS}} + G\right)y_{LS} - \frac{G'}{y'_{LS}}\frac{y^2_{LS}}{2}\right) + \\ Ste^2\left(\frac{A}{4}y^4_{LS} + \frac{B}{3}y^3_{LS} + \frac{C}{2}y^2_{LS} + Dy_{LS}\right) \end{bmatrix} \tag{31}$$

As discussed in section 2.4, the temperature at the PCM-fluid interface obtained from equation (23) is used for heat transfer analysis of the fluid flow sub-problem, which is discussed next.

6-2-3. Solution of convective heat transfer sub-problem

As shown schematically in Figure 2(b), the fluid flow problem comprises laminar, incompressible fluid flow with uniform freestream velocity U_∞ and temperature T_∞ past a flat plate

with a given temperature $\theta_s(x,t)$. The mass, momentum and energy conservation equations for this problem are given by equations (1-3), along with the boundary/initial conditions given by equations (4-7). An additional boundary condition is that of a given tempearture $\theta_s(x,t)$ at the flat plate. The interest is in solving this set of equations to determine the plate heat flux as a function of space and time, $q_s(x,t)$. While standard solutions are available for this problem in case of a constant plate temperature [19], the case of a temperature that varies in both space and time – as is the case for the PCM melting problem being discussed here – is more complicated. Recently, a solution for this problem has been proposed through the use of Karman-Pohlhausen polynomials. In this technique, the velocity and temperature distributions within the fluid flow are expressed in terms of third-order polynomials. Coefficients of these Karman-Pohlhausen polynomials are chosen to satisfy all boundary conditions, which is known to result in very good accuracy [19]. By inserting these expressions in the energy conservation equation (15), the following partial differential equation can be derived:

$$r^3 + 4\xi r^2 \frac{\partial r}{\partial \xi} + 2\xi r^3 \frac{1}{\theta_s}\frac{\partial \theta_s}{\partial \xi} + 5\frac{\xi}{\bar{U}_\infty}\left[\frac{r^2}{\theta_s}\frac{\partial \theta_s}{\partial \tau} + r\frac{\partial r}{\partial \tau}\right] = \frac{13}{14}Pr \tag{32}$$

Where $r = \frac{\bar{\delta}_t}{\bar{\delta}}$ and $\bar{\delta} = 4.64\sqrt{\frac{\bar{\alpha}_f Pr \xi}{\bar{U}_\infty}}$

$$r = 0 \ at \ \tau = 0 \tag{33}$$

$$r = 0 \ at \ \xi = 0 \tag{34}$$

Once equation (32) is solved, heat flux at the plate interface is determined by

$$G(\xi,\tau) = -\frac{3}{2}\frac{\bar{k}_f \theta_s(\xi,\tau)}{\left[4.64\sqrt{\dfrac{\bar{\alpha}_f Pr\xi}{\bar{U}_\infty}}\right] r(\xi,\tau)} \qquad (35)$$

Note that equations (32)-(35) represent a non-linear partial differential equation for the interface flux distribution, and the interface temperature $\theta_s(\xi,\tau)$ appearing in these equations is known from the plate boundary condition. While an analytical solution of equations (32)-(35) is unlikely to exist, a numerical integration of equation (32) can be carried out easily to determine the interface heat flux in response to a given interface temperature distribution. As discussed in the next sub-section, the heat flux determined in this manner is used in the iterative approach to solve the combined, conjugate heat transfer problem.
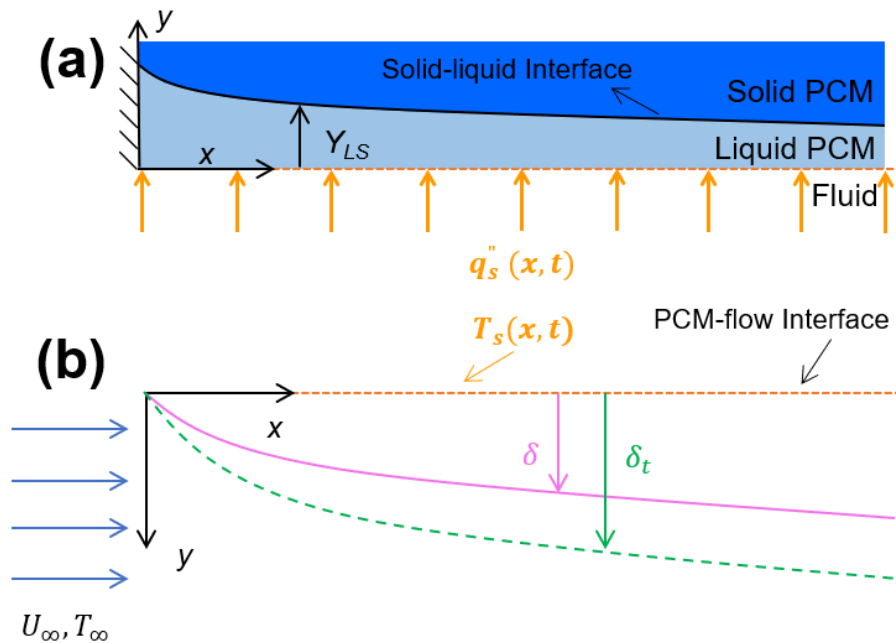
Figure 2. Schematic of (a) the PCM sub-problems; (b) flow sub-problems.

134

6-2-3 Iterative technique

An iterative technique is used to combine the solutions of the two sub-problems described in sections 2.2 and 2.3 in order to solve the combined problem. This technique starts by assuming a distribution for the interfacial heat flux, $G(\xi, \tau)$. Based on this, the PCM sub-problem is solved, as described in section 2.2. Specifically, the interfacial temperature distribution $\theta_s(\xi, \tau) = 1 - \theta_p(\xi, \eta = 0, \tau)$ is determined from equation (23). $\theta_s(\xi, \tau)$ is then used to solve the flow sub-problem as described in section 2.3. The plate flux distribution $G(\xi, \tau)$ computed from the solution of the flow sub-problem, given by equation (25) is computed. This is used to update the assumed plate temperature distribution by solving the PCM sub-problem again. A blend factor β is used to combine the old and computed plate temperature distributions to provide the new plate temperature distribution, with which to carry out the next iteration. Convergence is obtained when the old and computed plate temperature distributions are within tolerance of each other, so that further iterative computations do not change the solution by much. Figure 3 shows a flowchart of this iterative process for solving the conjugate problem involving both PCM and fluid flow regions.
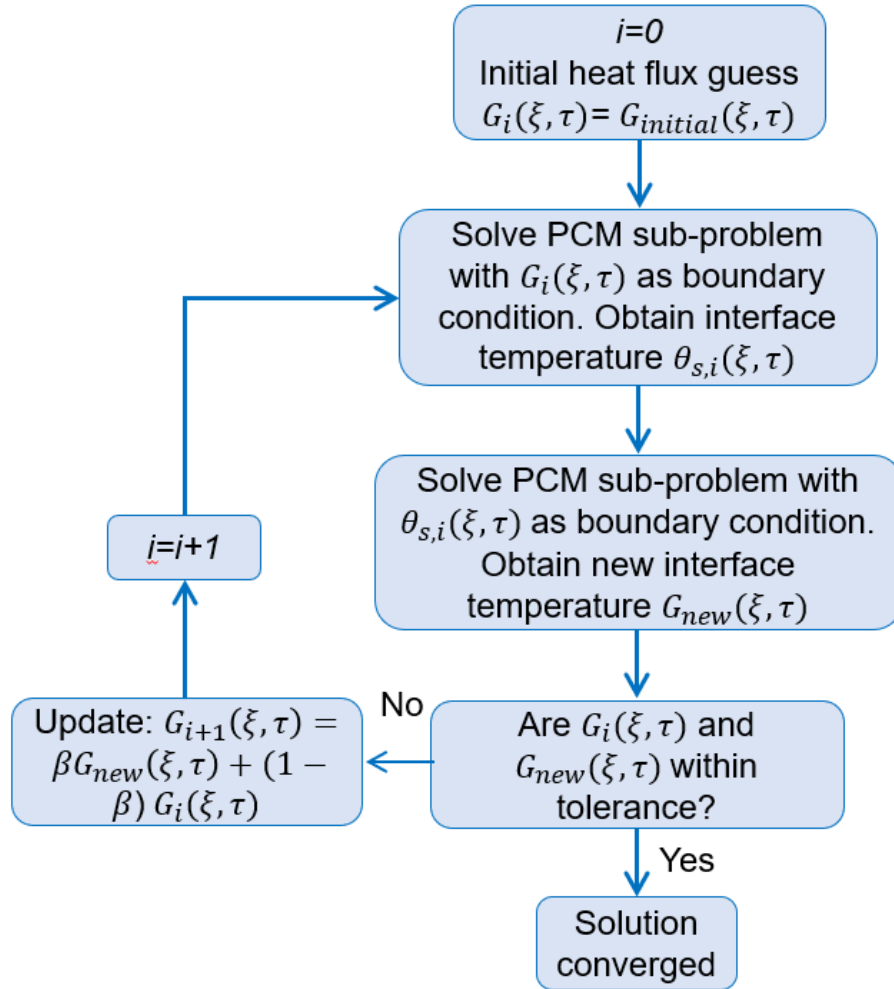
Figure 3. Flowchart of this iterative process for solving the conjugate problem involving both PCM and fluid flow regions.

6-3. Results and discussion

6-3-1. Iterative model validation

The iterative technique for the solving the complete conjugate PCM-flow problem discussed in section 2 is first compared with numerical simulation and the comparison is presented in Figure 4. In this case, air flow at $\bar{U}_\infty = 8.36 \times 10^8$ over a 0.1m long octadecane bed is considered. Freestream air temperature is 50 °C above the PCM melting temperature. Room temperature

136

values are used for thermal properties of air. Figure 4(a) shows a comparison of interface temperature distribution determined from the iterative model presented in Section 2 with numerical simulation results at $\tau = 8.36 \times 10^{-6}$. The model is found to be in good agreement with numerical simulation. Figure 4(b) plots a comparison of heat flux distribution at the PCM flow interface at $\tau = 8.36 \times 10^{-6}$. Similar to Fig. 4(a), good agreement is obtained between the model and numerical simulation.
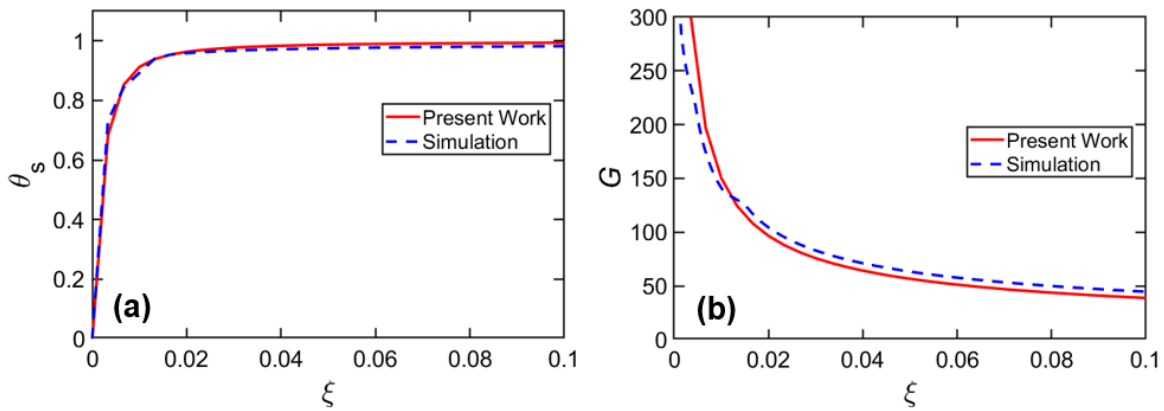
Figure 4. Comparison of the iterative approach with numerical simulation for the complete problem for distribution of (a) Interface temperature and (b) Heat flux at $\tau = 8.36 \times 10^{-6}$. In these plots, $\bar{U}_\infty = 8.36 \times 10^8$ and *Ste*=0.4713

Due to the iterative nature of the conjugate technique presented in this work, it is important to characterize iterative convergence and determine the number of iterations needed for a desired level of accuracy. While a general mathematical analysis of the convergence characteristics is very difficult, the evolution of the computed solution over several iterations is investigated for a representative problem. For the same parameters as Figure 5, except *Ste*=0.188, the computed temperature distribution at the PCM-flow interface at $\tau = 8.36 \times 10^{-6}$ s is plotted at the end of one, three and five iterations in Figure 5(a). The initial guess of $\theta_s = 1$ is also shown. Figure 5 shows rapid convergence of the computed temperature distribution, which, stabilizes and does not show any appreciable change subsequent to three iterations. This indicates that for a typical PCM-

flow problem, only around three iterations may be sufficient to reach a converged result. This finding is of much practical relevance, since a small number of iterations results in significant saving in computational cost.

A melting point temperature distribution at the interface is a reasonable initial guess, particularly for large ξ, since the temperature distribution at the interface is expected to be close to zero, bounded on the other end by the freestream temperature. However, in general, it is also important to determine the impact of the initial guess on the converged results and to verify that the converged solution is independent of the initial guess. This is particularly important when an initial guess may be significantly different from the converged solution. In order to investigate this, the iterative technique is carried out with two distinct – and very different – initial guesses. The convergence of these two cases is shown in Figure 5(b), in terms of temperature distributions at the end of successive iterations. It is shown that while the two cases considered here start from different points, both rapidly converge to the same temperature distribution. The temperature distributions at the end of five iterations for both cases are practically identical, as shown in Figure 5(b).
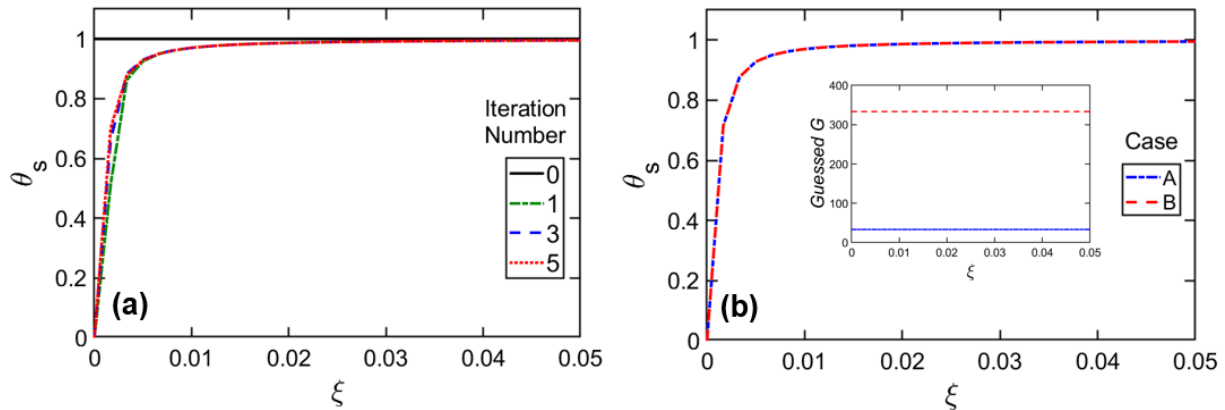
Figure 5. Validation of the iterative approach (a) interface temperature evolution over iterations and (b) effect of initial guess on the converged interface temperature. In these plots, $\bar{U}_\infty = 8.36 \times 10^8$, Ste=0.188 and $\tau = 8.36 \times 10^{-6}$.

The application of the iterative technique for understanding conjugate PCM-flow problems and the impact of various problem parameters on system performance is discussed next. The two key performance parameters of interest include the rate of phase change propagation into the PCM, and the amount of energy stored into or released from the PCM. Figure 6 plots the phase change front, η_{LS} distribution over the PCM bed at multiple times for a representative problem of flow of $\overline{U}_\infty = 8.36 \times 10^8$ and Ste=0.188 over an octadecane bed. As expected, the highest amount of phase change occurs close to the leading edge where the boundary layer is thinnest, resulting in very large rate of heat flow. As ξ increases, the boundary layer grows, heat flux reduces, and therefore, the extent of phase change is also lower.
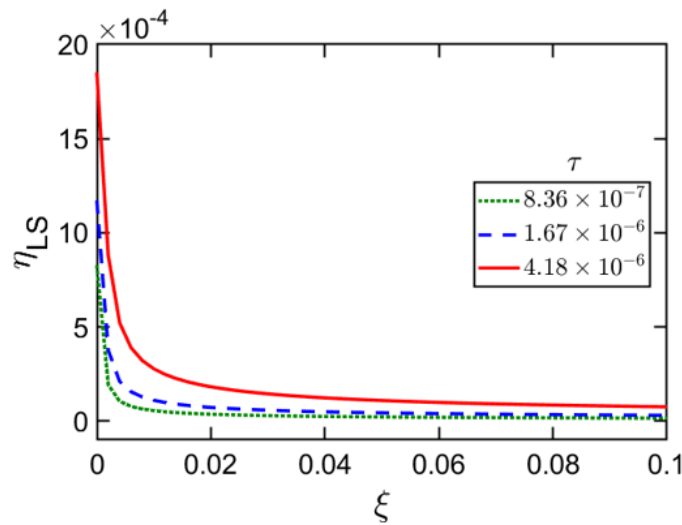
Figure 6. Melting front thickness distribution over the flat PCM bed at different times. In this plot, $\overline{U}_\infty = 8.36 \times 10^8$ and Ste=0.4713

Thermal conductivities of the fluid and PCM are the key thermal properties that influence phase change propagation and energy storage. The impact of these properties on system performance is investigated next. Figure 7(a) plots the total energy stored in the PCM as a function

of $\bar{k}_p$, while holding all other parameters constant, including $\bar{k}_f$. For this analysis, air with $\bar{U}_\infty =$ 8.36×10^8 and $Ste{=}0.4713$ is assumed to flow over a PCM bed for $\tau = 4.18 \times 10^{-6}$. Figure 7(b) shows the total energy stored in the PCM as a function of $\bar{k}_f$, while other parameters, including $\bar{k}_p$ are held constant. These plots show that the total energy stored is a much stronger function of thermal conductivity of the fluid rather than of the PCM. This indicates that under these conditions, the rate-limiting step in heat transfer and energy storage is on the fluid flow side rather than the PCM side. Therefore, efforts on improving energy storage must focus on improving convective heat transfer to/from the fluid rather than phase change heat transfer in the PCM.
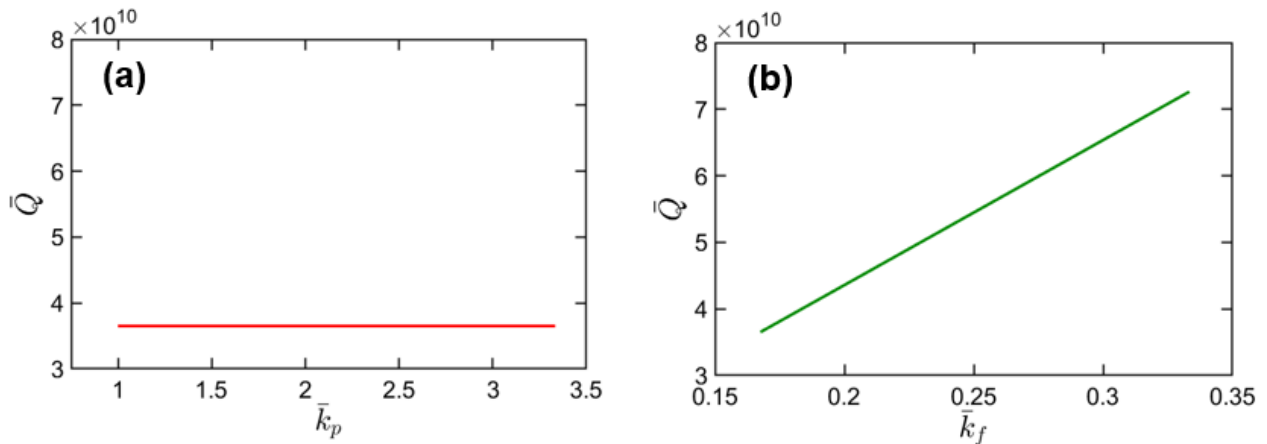
Figure 7. Total energy stored in the PCM up to $\tau = 4.18 \times 10^{-6}$ as a function of (a) PCM thermal conductivity and (b) fluid flow thermal conductivity. In this plot, $\bar{U}_\infty = 8.36 \times 10^8$ and $Ste{=}0.4713$

6-4. Conclusions

Understanding the nature of convective heat transfer in a flat bed PCM system is important to improve performance of latent energy storage systems. Generally, the heat transfer coefficient at

140

the PCM-flow interface is a function of both space and time which results in a complicated non-linear heat flux distribution at the interface. The present work establishes an analytical iterative approach to solve the conjugate heat transfer problem with heat transfer in the PCM and convective heat transfer in the fluid flow. The approach account for transient space varying conjugate heat transfer which was not accounted in the past.

From a theoretical perspective, this work improves the understanding of heat transfer in flat bed PCM systems. From a practical perspective, dependence of total heat stored in the system on thermal conductivity of the fluid and PCM is discussed. The results show that total heat stored is a much stronger function of thermal conductivity of the fluid rather than of the PCM. Phase change front propagation is also determined. The results may contribute towards design optimization of such systems for practical engineering applications.

The present work neglects the effect of natural convection in the liquid phase of PCM, which is not important for the PCM slabs mounted horizontally in a system.

6-5. Nomenclature

c specific heat capacity, $Jkg^{-1}K^{-1}$

G nondimensional heat flux, $G = \dfrac{q_s L}{k_p(T_\infty - T_m)}$

k thermal conductivity, $Wm^{-1}K^{-1}$

L reference length scale, m

L_p latent heat of fusion, Jkg^{-1}

Pr Prandtl number

q heat flux, Wm^{-2}

Re Reynolds number

Ste Stefan number, $Ste = \frac{c_p(T_\infty - T_m)}{L_p}$

t time, s

T temperature, K

T_m melting temperature, K

u,v Velocities in x and y directions, ms^{-1}

x spatial coordinate, m

θ nondimensional temperature, K

τ nondimensional time, $\tau = \frac{\alpha_p t}{L^2}$

α thermal diffusivity, m^{2}s^{-1}

ν kinematic viscosity, m^{2}s^{-1}

ρ mass density, kgm^{-3}

δ boundary layer thickness. m

ξ,η nondimensional spatial coordinates, $\xi = \frac{x}{L}, \eta = \frac{y}{L}$

Subscripts

f fluid flow

LS solid-liquid interface

p phase change material

s PCM- fluid flow interface

t thermal

∞ freestream

6-6. References

[1] Dincer, I., & Rosen, M. (2002). Thermal energy storage: systems and applications. John Wiley & Sons.

[2] Bar-cohen, A. (Ed.). (2018). Encyclopedia Of Thermal Packaging, Set 3: Thermal Packaging Applications (A 3-volume Set) (Vol. 3). World Scientific.

[3] Parhizi, M., & Jain, A. (2019). Analytical modeling and optimization of phase change thermal management of a Li-ion battery pack. Applied Thermal Engineering, 148, 229-237.

[4] Mills, A., Farid, M., Selman, J. R., & Al-Hallaj, S. (2006). Thermal conductivity enhancement of phase change materials using a graphite matrix. Applied thermal engineering, 26(14-15), 1652-1661.

[5] Lamberg, P., & Siren, K. (2003). Approximate analytical model for solidification in a finite PCM storage with internal fins. Applied Mathematical Modelling, 27(7), 491-513.

[6] Mostafavi, A., Parhizi, M., & Jain, A. (2019). Theoretical modeling and optimization of fin-based enhancement of heat transfer into a phase change material. International Journal of Heat and Mass Transfer, 145, 118698.

[7] Rozenfeld, T., Kozak, Y., Hayat, R., & Ziskind, G. (2015). Close-contact melting in a horizontal cylindrical enclosure with longitudinal plate fins: demonstration, modeling and application to thermal storage. International Journal of Heat and Mass Transfer, 86, 465-477.

[8] Caldwell, J., & Kwan, Y. Y. (2003). On the perturbation method for the Stefan problem with time-dependent boundary conditions. International Journal of Heat and Mass Transfer, 46(8), 1497-1501.

[9] Parhizi, M., & Jain, A. (2019). Solution of the phase change Stefan problem with time-dependent heat flux using perturbation method. Journal of Heat Transfer, 141(2).

[10] Parhizi, M., & Jain, A. (2019). The impact of thermal properties on performance of phase change based energy storage systems. Applied Thermal Engineering, 162, 114154.

[11] Dubovsky, V., Ziskind, G., & Letan, R. (2011). Analytical model of a PCM-air heat exchanger. Applied Thermal Engineering, 31(16), 3453-3462.

[12] Ezra, M., Kozak, Y., Dubovsky, V., & Ziskind, G. (2016). Analysis and optimization of melting temperature span for a multiple-PCM latent heat thermal energy storage unit. Applied Thermal Engineering, 93, 315-329.

[13] Vakilaltojjar, S. M., & Saman, W. (2001). Analysis and modelling of a phase change storage system for air conditioning applications. Applied Thermal Engineering, 21(3), 249-263.

[14] Ding, C., Niu, Z., Li, B., Hong, D., Zhang, Z., & Yu, M. (2020). Analytical modeling and thermal performance analysis of a flat plate latent heat storage unit. Applied Thermal Engineering, 179, 115722.

[15] Bechiri, M., & Mansouri, K. (2013). Exact solution of thermal energy storage system using PCM flat slabs configuration. Energy conversion and management, 76, 588-598.

[16] Lacroix, M. (1993). Study of the heat transfer behavior of a latent heat thermal energy storage unit with a finned tube. International journal of heat and mass transfer, 36(8), 2083-2092.

[17] Arnold, D. (1990). Dynamic simulation of encapsulated ice stores. Part I: the model. ASHRAE Trans, 97(2), 1170-1178.

[18] Alexiades, V., & Solomon, A. D. (2018). Mathematical modeling of melting and freezing processes. Routledge.

[19] W.M. Kays, M.E. Crawford, B. Weigand (2005). Convective heat and mass transfer. McGraw-Hill Higher Education, Boston.

[20] Dorfman, A. S. (2009). Conjugate problems in convective heat transfer. CRC Press.

[21] Shah, K., & Jain, A. (2015). An iterative, analytical method for solving conjugate heat transfer problems. International Journal of Heat and Mass Transfer, 90, 1232-1240.

[22] Chalise, D., Shah, K., Prasher, R., & Jain, A. (2018). Conjugate heat transfer analysis of thermal management of a Li-ion battery pack. Journal of Electrochemical Energy Conversion and Storage, 15(1).

[23] Murray, R. E., & Groulx, D. (2014). Experimental study of the phase change and energy characteristics inside a cylindrical latent heat energy storage system: Part 1 consecutive charging and discharging. Renewable energy, 62, 571-581.

[24] Mostafavi, A., & Jain, A. (2019). theoretical analysis of unsteady convective heat transfer from a flat plate with time-varying and spatially-varying temperature distribution. International Journal of Heat and Mass Transfer, in review.

Chapter 7

Dual-purpose thermal management of li-ion cells using solid-state thermoelectric elements

7-1. Introduction

The intermittent nature of renewable energy sources such as solar and wind power necessitates a robust mechanism for energy storage. A number of different energy storage technologies have been investigated in the past, including sensible and latent thermal energy storage [1], thermochemical energy storage [2], electrochemical energy storage [3], etc. Amongst these, electrochemical energy storage in Li-ion based cells and battery packs offers several advantages, such as compact energy storage, high discharge rates, etc. As a result, Li-ion cells have been widely investigated for electrochemical energy storage, in addition to applications in consumer electronics, electric vehicles and military applications [4]. Overheating of Li-ion cells during energy conversion and storage processes presents a key technological challenge that affects both performance and safety [5,6]. Heat generated in a Li-ion cell during charge or discharge leads to significant temperature rise due to its poor thermal conductivity [7]. If the temperature exceeds a certain threshold, a series of cascading exothermic decomposition reactions occur that result in ever-increasing cell temperature, eventually leading to fire and explosion [8]. Manufacturers often specify a maximum permission temperature in the range of 60-70 °C to avoid thermal runaway.

On the other hand, low temperature operation of Li-ion cells is also undesirable, as it has been shown to reduce performance and lifetime [9]. A Li-ion cell at low temperature must be rapidly heated up to an optimum window of 15 °C to 35 °C. This is a particularly important consideration for Li-ion cells in an electric vehicle that may be required to rapidly start and operate in cold climates.

As a result of these considerations, a robust, dual-purpose thermal management system is critically important for the performance and safety of Li-ion cells. The thermal management system must be able to limit cell temperature rise due to heat generation during charge/discharge.

146

It must also be able to rapidly heat up the cell from a low temperature ambient. Ideally, the same thermal management technique must be able to address both heating and cooling requirements, with seamless switching between the two modes.

A number of different approaches have been demonstrated separately for cell cooling and heating. Cooling approaches include air and liquid cooling [10], heat pipes [11], phase change cooling [12] and thermoelectric cooling [13]. Air cooling is typically easiest to implement, but may not be effective in aggressive conditions. Studies on air cooling systems have mainly focused on optimization of flow configuration and cell layout. Results of a parametric study on staggered battery pack identified top-located airflow inlet and outlet as the best cooling strategy [14]. Operating air flow pattern including forward and backward cycle was proposed to optimize temperature distribution of a single pouch cell [15]. Compared to air cooling, liquid cooling systems remove more heat, but are more complicated and required greater power [16]. Experiments on thermal silica plates integrated with water tubes show significant increase in cooling capacity and reduction in maximum temperature of the battery module [17]. Many other papers have also reported on optimization of cold plates for water cooling battery thermal management systems [16,18,19]. Phase change and heat pipe based thermal management systems offer the advantage of being passive in nature [20]. In order to heat up a cell in a cold climate, Joule heating in a metal foil inserted in the cell has been shown to result in rapid self-heating [21]. Self-heating using alternate current passed through the cell has also been proposed [22]. Most thermal management approaches investigated in the past, including the literature cited above, do not address both cooling and heating requirements of a Li-ion cell.

Thermoelectric based thermal management may be an attractive approach for Li-ion cells because of the dual ability to remove heat from and pump heat into the cell as needed.

Thermoelectric modules are solid-state heat pumps that produce a directional heat flow in response to an applied potential difference based on Peltier effect [23]. A standard single stage thermoelectric module consists of N-type and P-type semiconductor junctions connected electrically in series and thermally in parallel [24]. A potential difference applied across the device results in the flow of heat from one face to the other. Reversing the polarity of the potential difference results in reversal of direction of heat flow, and therefore, heat can be either removed or pumped into the system of interest. Performance of a thermoelectric element is characterized by the figure of merit, which is governed by the Seebeck coefficient, electrical conductivity and thermal conductivity of the thermoelectric element. Bismuth telluride (Bi_2Te_3) alloys are widely used bulk material in commercial thermoelectric elements [25]. Thermoelectric elements offer reliable and passive operation, with no moving parts, but often suffer from high power consumption due to low figure of merit [26].

Despite the high power consumption, a thermoelectric element may be suitable for Li-ion cell thermal management for niche applications where cooling during charge/discharge and heating in a low temperature ambient are both critical needs. While thermoelectric elements have been used widely for heating and cooling, their application for thermal management of Li-ion cells is somewhat limited. Most available literature focuses on numerical simulations rather than experimental measurements. More importantly, the dual use of thermoelectric elements for cooling and heating of Li-ion cells has not been recognized and investigated in the past. Numerical simulation of thermoelectric cooling has been compared to experimental data in the context of cooling of battery pack of an electrical vehicle [27]. In a related study, cooling of Lithium iron phosphate cells with thermoelectric element was evaluated [28]. Numerical simulation of a battery pack cooled by thermoelectric elements was carried out [29]. Heat exchanger design optimization

was performed with numerical simulation of a battery cell cooled by thermoelectric modules [30]. In another paper, thermoelectric elements were used to cool down the heat transfer fluid that in turn cools a cylindrical heater that mimics a Li-ion cell [31]. Given the theoretical possibility of obtaining both cooling and heating effects by reversing the polarity of the thermoelectric current, thermoelectric elements may offer an attractive approach for dual-purpose thermal management of a Li-ion cell.

This paper presents experimental and numerical analysis of dual-purpose thermal management of a Li-ion polymer cell using thermoelectric elements. Excellent cooling of the cell at aggressive discharge rates, as well as rapid heating of the cell in a low temperature ambient are demonstrated by simply reversing the polarity of thermoelectric current. Experimental data are found to be in very good agreement with numerical simulations. These results demonstrate the capability of thermoelectric elements to address two critical thermal management challenges in Li-ion cells. Experiments and numerical simulations are described in sections 2 and 3, respectively. Section 4 discusses key results, including experimental measurements, comparison with numerical simulations and prediction of core temperature of Li-ion cell.

7-2. Experiments

All experiments are carried out on a Li-ion polymer cell manufactured by Skyrich Battery Company. The cell has 4000 mAh nominal capacity and 3.2 V nominal voltage. Cell dimensions are 51.0 mm by 142.5 mm by 6.3 mm thick. The thermoelectric elements used in this work are manufactured by Hebei I.T. (Shanghai) Co. The rated maximum current and voltage of each thermoelectric element are 6.4 A and 16.4 V, respectively. Since each thermoelectric element covers an area of around 40 mm by 40 mm, the Li-ion cell is covered by three thermoelectric

elements on each face for full coverage. All thermoelectric elements are connected in series to an Extech Instruments DC power supply (model number 382270).

Figure 1 shows a picture of the first set of experiments in which the cooling effect of thermoelectric elements during high-rate cell discharge is characterized. In these experiments, a 9-fin aluminum heat sink, and a brushless DC fan are mounted on the hot side of the thermoelectric elements for heat removal to ambient air. The fans are powered by a 12 V Keysight E3644A power supply. The Li-ion cell is charged/discharged in room temperature ambient by a Kikusui PFX2512 battery charge/discharge controller that controls an electronic load PLZ14W and a power supply unit PWR800L for desired charge/discharge cycling of the cell. BPChecker3000 software is used for programming the charge/discharge cycle and for acquiring cell voltage and current data. Cell surface temperature is measured at two points using K-type thermocouples from Omega. Thermocouples are connected to a National Instruments NI-9213 data acquisition system controlled by LabVIEW software for temperature data acquisition. Three different thermoelectric currents and two different discharge rates are investigated in these experiments.

In the second set of experiments, the heating up of the cell from a cold ambient by the thermoelectric elements is investigated. The cell is first kept inside a low temperature chamber long enough for thermal equilibration with the set temperature of the cold chamber, and then heated up by the thermoelectric elements. Current is passed through the thermoelectric elements with switched polarity, so that the side connected to the cell now serves as the hot side, and the thermoelectric elements effectively pump heat into the cell, as opposed to removing heat in the first set of experiments. Cell temperature data acquisition is carried out similar to the first set of experiments.
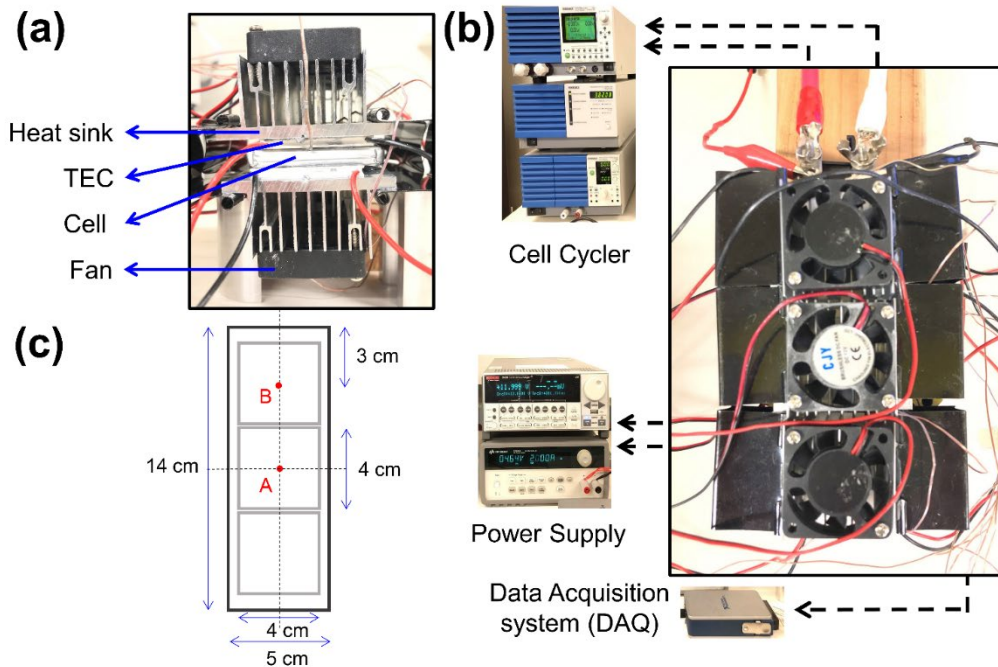
Figure 1. Pictures of the setup for thermoelectric-based cell cooling experiments: (a) and (b) show side-view and top-view pictures, respectively; (c) shows a schematic top view, including dimensions and thermocouple locations.

7-3 Simulation modeling

A finite-volume based heat transfer and fluid flow simulation is carried out in ANSYS Icepak software that numerically solves the equations governing thermal and fluid flow. These simulations serve to validate experimental measurements, as well as predict the core temperature of the cell, which is difficult to measure directly due to lack of access to the core of the cell. For these simulations, a model of the cell along with thermoelectric elements and heat sink, similar to the experimental setup shown in Figure 1(a) is placed inside a cabinet geometry. An opening with pressure outlet is considered for the sides of the simulation domain. Continuity, momentum and energy equations govern incompressible flow and heat transfer in the simulation as follows:

151

$$\nabla.V = 0 \tag{1}$$

$$\rho\left(\frac{\partial V}{\partial t} + (V.\nabla)V\right) = -\nabla p + \nabla.\tau + \rho g \tag{2}$$

$$\rho c_p\left(\frac{\partial T}{\partial t} + (V.\nabla)T\right) = k\nabla^2 T + Q \tag{3}$$

where V, p, τ and Q denote velocity vector, pressure, stress tensor and heat source term respectively. ρ, c_p, k and g are density, heat capacity, thermal conductivity and acceleration due to gravity, respectively. Associated boundary conditions include openings for inflow and outflow, while no-slip is defined at other boundaries.

The geometry of the cell, thermoelectric elements, heat sinks and fans are modeled in order to closely match experimental conditions. The simulation domain is meshed with quadrilateral elements. A total of 920232 nodes are used. Further mesh refinement is found to result in negligible change in results. Values of thermal properties reported for a Li-ion polymer cell of the same chemistry and similar size as the present cell [32] are used in simulations. Thermal conductivity of the Li-ion cell is modeled to be anisotropic in nature, with values of 0.99 $Wm^{-1}K^{-1}$ and 24.6 $Wm^{-1}K^{-1}$ in the through-plane (thickness) and in-plane directions, respectively. Specific heat capacity of the cell is taken to be 1050 $Jkg^{-1}K^{-1}$, as reported by the same paper. Mass density of the cell is determined through measurements to be 2050 kgm^{-3}.

The value of heat generation rate as a function of C-rate has been reported in the past for a Li-ion polymer cell of the same chemistry and similar size as the cell in the present study [32, 33]. These values of heat generation rate are used in simulations. Heat generation rate is expressed on a volumetric basis to account for the different capacities of the present cell and the one in the

previous paper. Heat generation rate in the cell is assumed to remain constant during the discharge period [34]. The use of previously-reported thermal parameters in these simulations is reasonable because the cell in the present has the same chemistry and similar size as the previously-reported cell. Unfortunately, direct measurement of heat generation rate was not possible on the present cell.

Standard thermal properties of aluminum are used for the heat sink. Air speed from the fan is measured directly using an Extech 45118 anemometer and provided as a boundary condition for the simulations. Icepak offers a library of different thermoelectric elements for simulation. In each case, the values of thermoelectric element properties including Seebeck coefficient, electrical resistivity and thermal conductivity are defined as third-order polynomial functions of absolute average temperatures between the cold and hot side. While such data for the specific thermoelectric elements used in present experiments are not directly available, values for a thermoelectric element from Laird Company, that has very close mechanical and thermal properties compared to the present thermoelectric element, are used. Based on the expressions for temperature-dependent properties, the thermoelectric effect is simulated and combined with thermal and fluid flow calculations to predict temperatures of cold and hot sides of the thermoelectric element for the specified thermoelectric current. Considering the standard simplified energy equilibrium for a thermoelectric module, the cooling capacity Q_c can be described as

$$Q_c = \alpha I T_c - k(T_h - T_c) - 0.5RI^2 \tag{4}$$

where α, k, R, I, T_c, T_h represent Seebeck coefficient, thermal conductivity, resistance, current, cold side and hot side temperatures of the TEC module, respectively. The input electrical power for the TEC module is given by

$$P_e = \alpha I (T_h - T_c) + R I^2 \tag{5}$$

which represents the sum of Joule heating and work done against the Seebeck effect [24]. Mixing length turbulent model is used for flow simulations, which is appropriate due to the fairlysimple geometry and flow characteristics [35]. Radiative heat transfer is neglected due to the relatively small temperature rise. A fixed time step of 0.05s is used throughout the computations, which are run for the entire charge/discharge duration. Residual convergence criterion is set to 10^{-5} for continuity and momentum equations, and 10^{-7} for energy equation.

7-4. Results and discussion

A number of experiments are carried out to characterize the cooling and heating aspects of thermoelectric-based thermal management. These experiments help understand the extent of cooling expected during high-rate discharge, as well as the capability of fast heating of a cell by operating the thermoelectric element in reverse polarity. A simulation model is also developed for comparison with experimental data. These results are discussed in sub-sections below.

7-4-1. Cooling effect of thermoelectric elements

The Li-ion pouch cell is discharged at 4C and 5C rates while being cooled by thermoelectric elements on both surfaces using the experimental methodology presented in section 2. The cell surface temperature, measured at point A (Figure 1(c)) is plotted as a function of depth of discharge (DOD) for 4C and 5C discharge rates in Figures 2(a) and 2(b), respectively. During a discharge process, the value of DOD changes from 0.0 (fully charged) to 1.0 (fully discharged). In each case, three different thermoelectric cooling currents are used, and compared against the baseline case without thermoelectric cooling. Figure 2(a) shows that the cell surface temperature increases steadily during 4C discharge for the baseline line without thermoelectric cooling. In comparison,

there is a significant reduction in temperature when the thermoelectric element is used. For each thermoelectric current, the cell surface temperature first reduces below ambient temperature and then slowly rises. Even at the end of the discharge process, the cell surface temperature is actually lower than the temperature at the start of the discharge process. Compared to the 20 °C temperature rise in the baseline case, this is a very favorable thermal outcome.

The reason for the temperature dip in the initial period is that as the discharge process proceeds, the cell surface is first influenced by the cooling effect of the thermoelectric element, which begins as soon as thermoelectric current begins to flow. As expected, the extent of the initial temperature reduction is greater for higher thermoelectric currents. As time passes, diffusion of heat generated within the cell to the surface becomes more and more significant, causing an increase in temperature. While the thermoelectric cooling effect is near-instantaneous, in contrast, the heating effect of heat generation within the cell takes longer to reach the cell surface due to the finite diffusion timescale. This explains why the cell surface temperature first drops and then steadily rises with time. Cell surface temperature at the end of the process is largely invariant of the thermoelectric current.
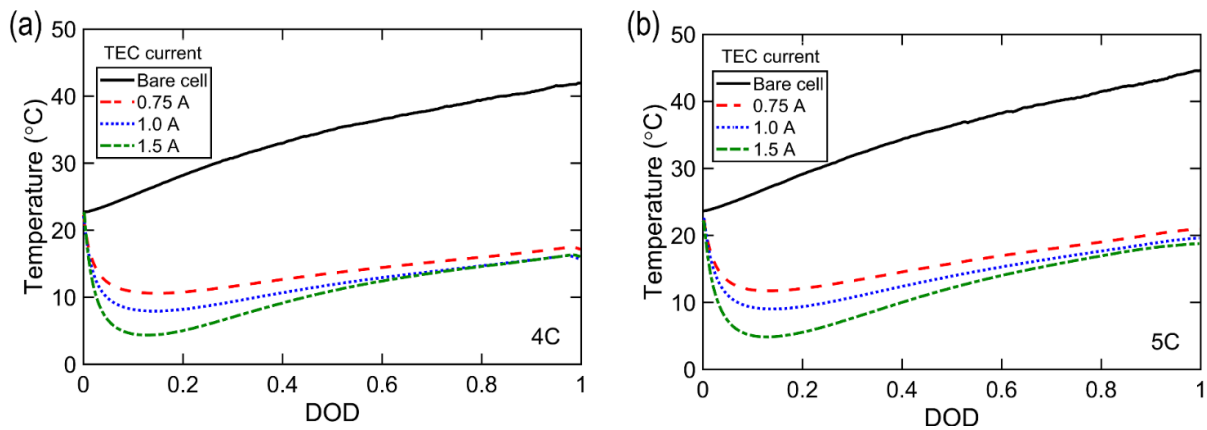
Figure 2. Cell surface temperature as a function of depth of discharge during thermoelectric-based cooling for (a) 4C, and (b) 5C discharge rates. In each case, data are plotted for three different thermoelectric currents and the baseline case with no thermoelectric cooling.

The nature of measurements at 5C discharge rate shown in Figure 2(b) is consistent with the 4C data – cell surface temperature reduces first and then rises steadily. By comparing measurements with the baseline case, there is somewhat greater benefit of thermoelectric cooling (compared to the baseline) in the 5C case than in the 4C case.

These data show that thermoelectric cooling is very effective for thermal management during high rate discharge – there is nearly zero temperature rise compared to a temperature rise of 20-25 °C for the baseline case without thermoelectric cooling. Note that the high power consumption of the thermoelectric elements may be a concern. The thermoelectric element is estimated to consume around 2.6 W power at 0.75 A current. Some strategies to minimize this power consumption may be possible. For example, experiments described here resulted in nearly zero temperature rise at 0.75A thermoelectric current. Depending on the application, it may be possible to tolerate a small temperature rise with the benefit of a lower thermoelectric current. Pulsed operation of thermoelectric elements may be another option for reducing power consumption.

7-4-2. Heating effect in cold ambient

Fast heating of a Li-ion cell in a cold ambient is also an important thermal management need for practical applications. For example, in a cold environment, it is important to rapidly heat up the cells in an automotive battery pack to the optimal operating temperature range. This may be relevant, for example, when an electric car has been parked outside overnight in a very cold climate and the battery pack now needs to be rapidly heated up for optimal performance. By reversing the polarity of the thermoelectric element, it is possible to pump heat into the Li-ion cell instead of removing heat, and thereby help address this important thermal management requirement.

A number of experiments are carried out in order to characterize the thermoelectric heating effect on the Li-ion cell. In each case, the Li-ion pouch cell, with thermoelectric elements attached

on both faces is placed in a cold ambient for a long time. Once the cell has reached thermal equilibrium with its ambient, electric current is passed through the thermoelectric element with reversed polarity compared to experiments in section 4.1, with the goal of providing heating to the cell, so that the optimal operating temperature can be reached as soon as possible. Three different thermoelectric currents are investigated at two different values of the cold ambient temperature. There is no charge/discharge of the cell during these experiments, since the goal is simply to characterize the impact of the thermoelectric element on heating up of the cell.

Figure 3(a) plots cell surface temperature at point A as a function of time for three different thermoelectric currents for a 0 °C ambient. In each case, the cell temperature rises with time, with a greater rate of increase for larger thermoelectric currents. Taking 20 °C as the target cell temperature, it is seen that it takes around 75 s for the cell to heat up when the thermoelectric current is somewhat low, at 0.75 A. At greater thermoelectric current, cell temperature rises much faster. For both 1.0 A and 1.5 A cases, the cell reaches 20 °C within 30 and 10 seconds, respectively, which is a relatively short duration.

In order to characterize the thermoelectric heating effect in even more stringent conditions, these experiments are repeated in a -23 °C ambient. These results, plotted in Figure 3(b) show that with 1.5 A thermoelectric current, optimal cell temperature is reached in about 70 seconds. As expected, at 1.0 A thermoelectric current, the cell reaches 20 °C after much longer, by around 310 s. With 0.75 A thermoelectric current, the cell does not reach the optimal 20 °C temperature at all, instead stabilizing at a lower temperature. These data are along expected lines, since a lower ambient temperature makes it more challenging to heat up the cell, and therefore, it takes longer time, and in some cases, the optimal temperature is not reached at all.

It is quite significant that the optimal temperature can be reached within 10 s and 70 s for ambient temperatures of 0 °C and -23 °C, respectively with 1.5 A thermoelectric current. These data show that thermoelectric elements can help heat up a Li-ion cell into its optimal operating temperature range within a short time. Following initial warmup, the same thermoelectric element can be used for cooling the cell during charge/discharge by simply reversing the polarity of the thermoelectric current. This represents effective and seamless management of two key thermal challenges in a Li-ion cell.
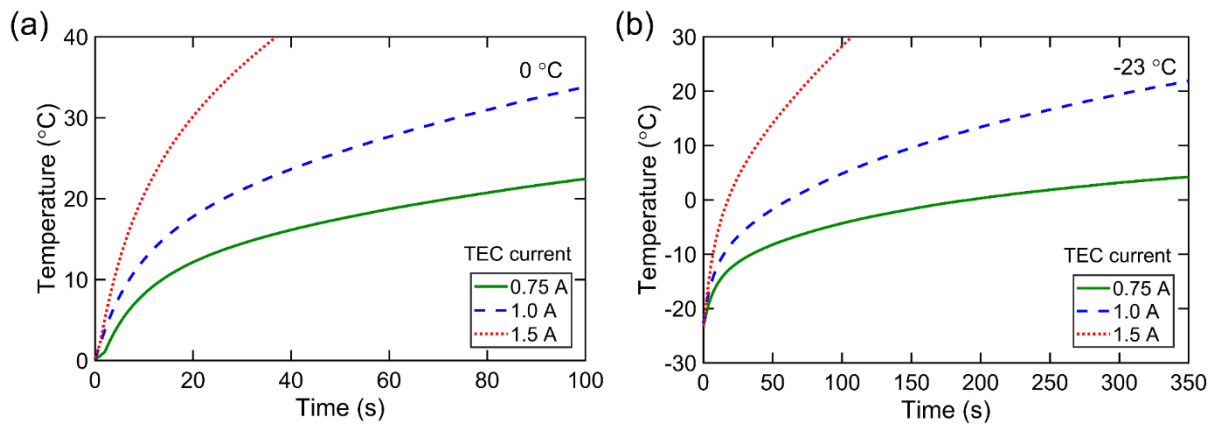
Figure 3. Cell surface temperature as a function of time during thermoelectric-based heating for (a) 0 °C, and (b) -23 °C ambient temperature. In each case, data are plotted for three different thermoelectric currents, with polarity reversed compared to cooling experiments.

Taken together, the data in Figures 2 and 3 demonstrate the dual benefit of thermoelectric elements. When the cell discharges at a high rate and therefore generates a lot of heat, thermoelectric currents may be an effective mechanism for thermal management, resulting in nearly zero temperature rise during discharge, while consuming relative low electrical energy. On the other hand, when the thermal requirement is to rapidly heat up the cell in a cold ambient, the same thermoelectric element, with reversed polarity can drive heat into the cell, thereby rapidly heating up the cell. Switching from one to the other merely requires changing the direction of the

thermoelectric current. Even in fairly adverse ambient conditions, experiments demonstrate a relatively short time to heat up the cell with the thermoelectric element.

7-4-3. Comparison of measurements with simulations

As discussed in Section 3, finite-volume simulations are carried out for comparison against experimental measurements.

Figure 4 compares temperature as a function of time obtained from experiments and simulations for a 5C discharge process at three different thermoelectric currents in the cooling mode. In each case, the cell surface temperature and heat sink temperature on the other face of the thermoelectric element are both plotted and compared. For each thermoelectric current, Figure 4 shows good agreement between experiments and simulations for both cell and heat sink temperatures. Simulations confirm the non-monotonic behavior of cell temperature over time due to the interplay between thermoelectric heat removal and diffusion of heat generated in the cell. As expected, temperature at the heat sink is greater than at the cell surface because the thermoelectric element pumps heat from the cell across and into the heat sink.

While Figure 4 plots the measured data at constant discharge rate for different thermoelectric currents, Figure 5 plots the measured data at constant thermoelectric current for different discharge rates. Cell surface and heat sink temperatures are plotted as functions of time for two different discharge rates in Figures 5(a) and 5(b). In both cases, the current passing through the thermoelectric element is held constant at 1.0 A. Similar to Figure 4, there is good agreement between experimental measurements and finite-volume simulations. For both cell and heat sink temperatures, the nature of the experimentally measured curve is consistent with that predicted by simulations.
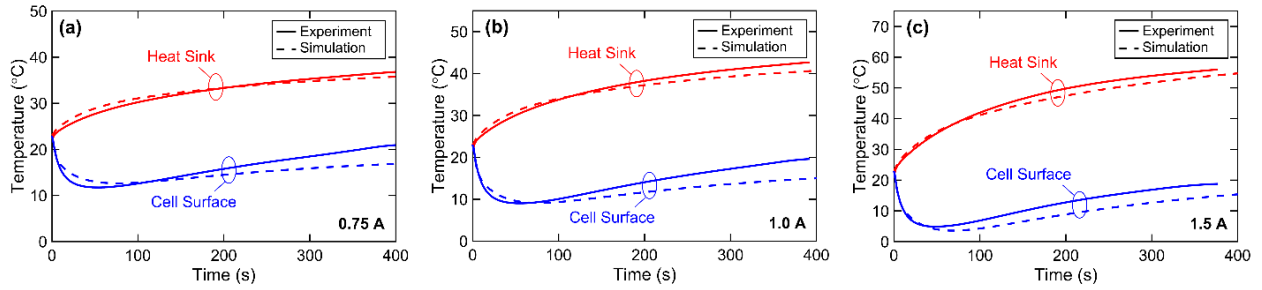
Figure 4. Comparison of experimental measurement and numerical simulation for cell surface and heat sink temperatures during 5C discharge for (a) 0.75 A, (b) 1.0 A, and (c) 1.5 A thermoelectric current.

There may be several reasons behind the relatively minor deviation between measurements and simulations in Figures 4 and 5. In addition to uncertainties in experimental measurement, the constant heat generation rate assumption during the discharge process may also be a source of error. Thermal contact resistance between components may play a small role, even though a thermal paste is used throughout to minimize contact resistance.
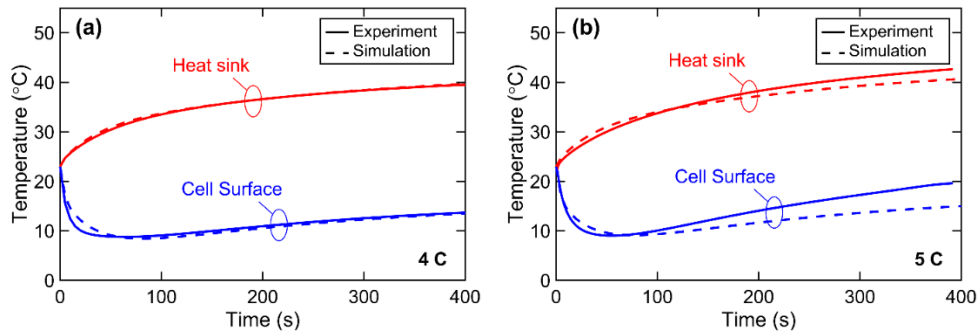
Figure 5. Comparison of experimental measurement and numerical simulation for cell surface and heat sink temperatures with 1.0 A thermoelectric current for (a) 4C, and (b) 5C discharge.

7-4-4. Core temperature estimation

Experimental data presented in Figure 2 show that the cell surface temperature may actually decrease during high rate discharge due to the cooling effect of the thermoelectric element. It is

160

important to recognize that cooling impact of the thermoelectric element may be lesser at the core of the cell than at the cell surface, due to the large thermal resistance within the cell because of low thermal conductivity [7] and large interfacial thermal resistances within the cell [38]. In addition to the reported surface temperature measurements, it is important to quantify the impact of thermoelectric cooling on the core temperature of the cell.

Unfortunately, it is not possible to directly measure the core temperature of the cell since a temperature sensor may not be inserted into the hermetically sealed cell. While some methods for non-invasive core temperature estimation are available [39], these methods may not be directly applicable here. In light of these difficulties, finite-volume simulations are carried out to predict the core temperature. There is high confidence in the simulation methodology due to good agreement with experimental measurements shown in Figures 4 and 5. Simulation results are presented in Figure 6 that plots predicted core and surface temperatures as functions of time for a 5C discharge process with 0.75 A thermoelectric current. Figure 6 shows, as expected, that the cell core temperature is greater than the cell surface temperature. Figure 6 shows that while the cell surface temperature has a sharp drop followed by gradual rise, the core temperature increases for a very small time, followed by a reduction and finally, a gradual increase. This is explained on the basis of the balance between heat generation within the cell during discharge and heat removal by the thermoelectric element. There is a short period of temperature rise at the cell core due to heat generation being dominant until the cooling effect of the thermoelectric element diffuses from the cell surface to the cell core. This short period is consistent with the thermal penetration time calculated by thermal diffusion considerations. As the core begins to be influenced by the thermoelectric element, the core temperature begins to reduce. Eventually, heat generation and thermoelectric cooling balance each other out, and the core temperature rises again in a nearly

linear fashion until the end of the discharge process. While Figure 6 shows greater temperature rise at the core compared to the surface, nevertheless, the net temperature rise during the entire process in the presence of thermoelectric cooling is negative even at the cell core.
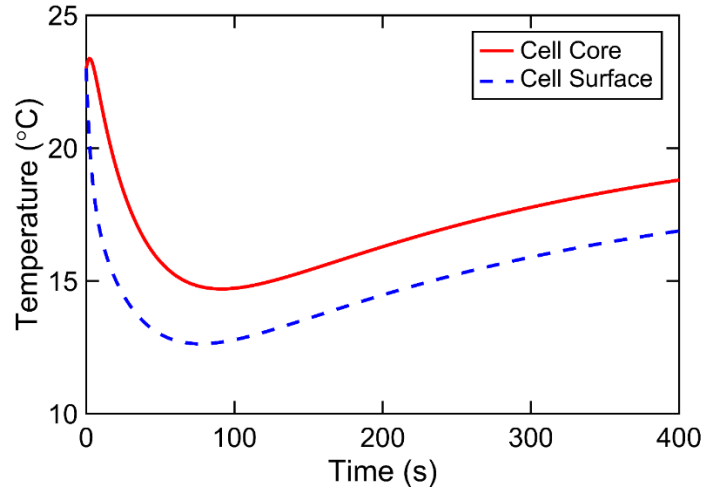
Figure 6. Core and surface cell temperatures predicted by numerical simulation for 5C discharge in the presence of cooling with 0.75 A thermoelectric current.

7-4-5. Effect of partial thermoelectric coverage

While experiments described above show effective thermal management of the Li-ion cell with thermoelectric elements, it is also important to understand the limits of thermoelectric cooling in practical scenarios. Specifically, the extent of cooling possible when the thermoelectric elements are operating partially must be studied. In order to do so, experiments are carried out where two of the three thermoelectric elements on each side of the Li-ion cell are considered to be inoperational by cutting off current supply. This mimics a practical scenario of partial failure of the thermoelectric-based thermal management system. The geometry for this case is shown in Figure 7, which indicates two locations A and B on the cell surface where temperature is measured.

While point A is directly under the single operational thermoelectric element, point B is under one of the failed thermoelectric elements.
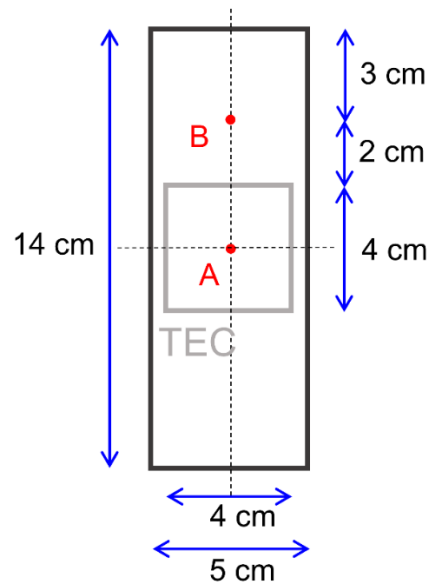
Figure 7. Schematic top view of thermoelectric cooling during partially disabled scenario. Only the middle thermoelectric element shown in this Figure is active.

Figure 8 summarizes temperature measurements at points A and B during discharge at 5C rate for fully covered and partially covered scenarios. Data are presented for three different thermoelectric currents. Figures 8(a)-(c) show that thermal performance at point A in the partially covered case is nearly as good as the fully covered case. This is along expected lines, since point A lies directly underneath the single operating thermoelectric element, and therefore is not dramatically influenced by failure of the other thermoelectric elements. On the other hand, failure of two thermoelectric elements does have a more pronounced effect on temperature at point B, as shown in Figures 8(d)-(f), even though temperature rise at point B is still lower than the baseline case. The behavior described above is consistent for all three thermoelectric currents investigated

163

in these experiments. Figure 8 quantifies the effect of thermoelectric cooling in a scenario of partial operation.
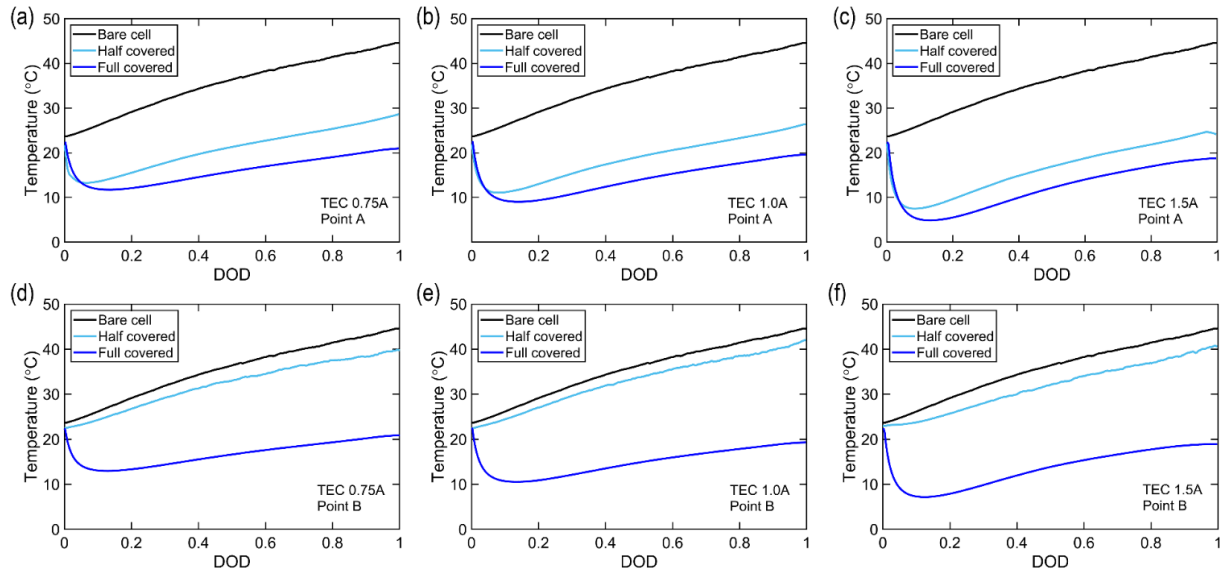
Figure 8. Comparison of cell surface temperatures at two different points for fully enabled and partially disabled scenarios for three different thermoelectric currents. (a)-(c) plot data for point A for 0.75A, 1.0A and 1.5A thermoelectric currents. (d)-(f) present similar data for point B. In each case, the baseline temperature curve without thermoelectric cooling is also plotted for comparison.

7-4. Conclusions

This paper shows that thermoelectric elements may offer an effective approach for meeting both cooling and heating requirements for a Li-ion cell. Both cooling and heating of a Li-ion cell are demonstrated, with good agreement between experimental data and numerical simulation results. The seamless switching between cooling and heating modes by simply changing polarity of thermoelectric current makes this approach particularly attractive.

It is important to note that there may be significant energy consumption in the thermoelectric elements for thermal management of the Li-ion cell. At 0.75A thermoelectric current, the power

consumption in the thermoelectric element is estimated to be 2.6 W. Even though the thermoelectric element is able to dissipate the energy it consumes to its hot side, and from there to the ambient by the heat sink and fan, nevertheless, the high power consumption of the thermoelectric element may be a concern for several applications. The trade-off between thermal management and power consumption is likely to be application-specific and needs to be carefully considered and optimized. Techniques for minimizing thermoelectric power consumption, such as those discussed briefly in section 4.1, need to be investigated further. Despite the high power consumption and cost, thermoelectric elements may be suitable for thermal management of Li-ion cells in specific applications.

7-6. References

[1] S. Hasnain, Review on sustainable thermal energy storage technologies, Part I: heat storage materials and techniques, *Energy Conversion and Management*. **39** (1998) 1127–1138. doi:10.1016/s0196-8904(98)00025-9.

[2] J. Cot-Gores, A. Castell, L.F. Cabeza, Thermochemical energy storage and conversion: A-state-of-the-art review of the experimental research under practical conditions, *Renewable and Sustainable Energy Reviews*. **16** (2012) 5207–5224. doi:10.1016/j.rser.2012.04.007.

[3] K. Shah, N. Balsara, S. Banerjee, M. Chintapalli, A.P. Cocco, W.K.S. Chiu, et al., State of the Art and Future Research Needs for Multiscale Analysis of Li-Ion Cells, *Journal of Electrochemical Energy Conversion and Storage*. **14** (2017). doi:10.1115/1.4036456.

[4] B. Scrosati, J. Garche, Lithium batteries: Status, prospects and future, *Journal of Power Sources*. **195** (2010) 2419–2430. doi:10.1016/j.jpowsour.2009.11.048.

[5] K. Shah, V. Vishwakarma, A. Jain, Measurement of Multiscale Thermal Transport Phenomena in Li-Ion Cells: A Review, *Journal of Electrochemical Energy Conversion and Storage*. **13** (2016). doi:10.1115/1.4034413.

[6] T.M. Bandhauer, S. Garimella, T.F. Fuller, A Critical Review of Thermal Issues in Lithium-Ion Batteries, *Journal of The Electrochemical Society*. **158** (2011). doi:10.1149/1.3515880.

[7] S. Drake, D. Wetz, J. Ostanek, S. Miller, J. Heinzel, A. Jain, Measurement of anisotropic thermophysical properties of cylindrical Li-ion cells, *Journal of Power Sources*. **252** (2014) 298–304. doi:10.1016/j.jpowsour.2013.11.107.

[8] K. Shah, A. Jain, Prediction of thermal runaway and thermal management requirements in cylindrical Li-ion cells in realistic scenarios, *International Journal of Energy Research*. **43** (2019) 1827–1838. doi:10.1002/er.4411.

[9] S. Zhang, K. Xu, T. Jow, The low temperature performance of Li-ion batteries, *Journal of Power Sources*. **115** (2003) 137–140. doi:10.1016/s0378-7753(02)00618-3.

[10] D. Chen, J. Jiang, G.-H. Kim, C. Yang, A. Pesaran, Comparison of different cooling methods for lithium ion battery cells, *Applied Thermal Engineering*. **94** (2016) 846–854. doi:10.1016/j.applthermaleng.2015.10.015.

[11] D. Anthony, D. Wong, D. Wetz, A. Jain, Improved Thermal Performance of a Li-Ion Cell through Heat Pipe Insertion, *Journal of The Electrochemical Society*. **164** (2017). doi:10.1149/2.0191706jes.

[12] M. Parhizi, A. Jain, Analytical modeling and optimization of phase change thermal management of a Li-ion battery pack, *Applied Thermal Engineering*. **148** (2019) 229–237. doi:10.1016/j.applthermaleng.2018.11.017.

[13] A.R.M. Siddique, S. Mahmud, B.V. Heyst, A comprehensive review on a passive (phase change materials) and an active (thermoelectric cooler) battery thermal management system and their limitations, *Journal of Power Sources*. **401** (2018) 224–237. doi:10.1016/j.jpowsour.2018.08.094.

[14] Z. Lu, X. Yu, L. Wei, Y. Qiu, L. Zhang, X. Meng, et al., Parametric study of forced air cooling strategy for lithium-ion battery pack with staggered arrangement, Applied Thermal Engineering. 136 (2018) 28–40. doi:10.1016/j.applthermaleng.2018.02.080.

[15] S. Wang, K. Li, Y. Tian, J. Wang, Y. Wu, S. Ji, Improved thermal performance of a large laminated lithium-ion power battery by reciprocating air flow, Applied Thermal Engineering. 152 (2019) 445–454. doi:10.1016/j.applthermaleng.2019.02.061.

[16] M. Malik, I. Dincer, M.A. Rosen, M. Mathew, M. Fowler, Thermal and electrical performance evaluations of series connected Li-ion batteries in a pack with liquid cooling, Applied Thermal Engineering. 129 (2018) 472–481. doi:10.1016/j.applthermaleng.2017.10.029.

[17] C. Wang, G. Zhang, X. Li, J. Huang, Z. Wang, Y. Lv, et al., Experimental examination of large capacity liFePO$_4$ battery pack at high temperature and rapid discharge using novel liquid cooling strategy, International Journal of Energy Research. 42 (2017) 1172–1182. doi:10.1002/er.3916.

[18] X. Du, Z. Qian, Z. Chen, Z. Rao, Experimental investigation on mini-channel cooling-based thermal management for Li-ion battery module under different cooling schemes, International Journal of Energy Research. 42 (2018) 2781–2788. doi:10.1002/er.4067.

[19] X. Li, D. Zhou, G. Zhang, C. Wang, R. Lin, Z. Zhong, Experimental investigation of the thermal performance of silicon cold plate for battery thermal management system, Applied Thermal Engineering. 155 (2019) 331–340. doi:10.1016/j.applthermaleng.2019.04.007.

[20] J. Jaguemont, J.V. Mierlo, A comprehensive review of future thermal management systems for battery-electrified vehicles, Journal of Energy Storage. 31 (2020) 101551. doi:10.1016/j.est.2020.101551.

[21] X.-G. Yang, T. Liu, C.-Y. Wang, Innovative heating of large-size automotive Li-ion cells, *Journal of Power Sources*. **342** (2017) 598–604. doi:10.1016/j.jpowsour.2016.12.102.

[22] J. Zhang, H. Ge, Z. Li, Z. Ding, Internal heating of lithium-ion batteries using alternating current based on the heat generation model in frequency domain, *Journal of Power Sources*. **273** (2015) 1030-1037. doi: 10.1016/j.jpowsour.2014.09.181

[23] B. Huang, C. Chin, C. Duang, A design method of thermoelectric cooler, *International Journal of Refrigeration*. **23** (2000) 208–218. doi:10.1016/s0140-7007(99)00046-8.

[24] D. Enescu, E.O. Virjoghe, A review on thermoelectric cooling parameters and performance, *Renewable and Sustainable Energy Reviews*. **38** (2014) 903–916. doi:10.1016/j.rser.2014.07.045.

[25] D. Champier, Thermoelectric generators: A review of applications, *Energy Conversion and Management*. **140** (2017) 167–181. doi:10.1016/j.enconman.2017.02.070.

[26] M.H. Elsheikh, D.A. Shnawah, M.F.M. Sabri, S.B.M. Said, M.H. Hassan, M.B.A. Bashir, et al., A review on thermoelectric renewable energy: Principle parameters that affect their performance, *Renewable and Sustainable Energy Reviews*. **30** (2014) 337–355. doi:10.1016/j.rser.2013.10.027.

[27] C. Alaoui, Solid-State Thermal Management for Lithium-Ion EV Batteries, *IEEE Transactions on Vehicular Technology*. **62** (2013) 98–107. doi:10.1109/tvt.2012.2214246.

[28] Z. Salameh, C. Alaoui, Modeling and simulation of a Thermal Management System for Electric Vehicles,' 29th Annual Conference of the IEEE Industrial Electronics Society (IEEE Cat. No.03CH37468). (n.d.). doi:10.1109/iecon.2003.1280100.

[29] Y. Liu, S. Yang, B. Guo, C. Deng, Numerical Analysis and Design of Thermal Management System for Lithium Ion Battery Pack Using Thermoelectric Coolers, *Advances in Mechanical Engineering*. **6** (2014) 852712. doi:10.1155/2014/852712.

[30] C. Zhang, Study on a Battery Thermal Management System Based on a Thermoelectric Effect, *Energies*. **11** (2018) 279. doi:10.3390/en11020279.

[31] Y. Lyu, A. Siddique, S. Majid, M. Biglarbegian, S. Gadsden, S. Mahmud, Electric vehicle battery thermal management system with thermoelectric cooling, *Energy Reports*. **5** (2019) 822–827. doi:10.1016/j.egyr.2019.06.016.

[32] N. Nieto, 'A model-based design of a thermal management system for a high power Li-ion battery pack,' Ph.D. Dissertation, University of Navarra, San Sabastián, 2014.

[33] N. Nieto, L. Díaz, J. Gastelurrutia, I. Alava, F. Blanco, J.C. Ramos, A. Rivas, Thermal modeling of large format Lithium-ion cells, *J. Electrochem. Soc.* **160** (2013) A212-A217. doi: 10.1149/2.042302jes

[34] S.A. Hallaj, H. Maleki, J. Hong, J. Selman, Thermal modeling and design considerations of lithium-ion batteries, *Journal of Power Sources*. **83** (1999) 1–8. doi:10.1016/s0378-7753(99)00178-0.

[35] K. Dhinsa, C. Bailey, K. Pericleous, Turbulence Modelling for Electronic Cooling: A Review, 2005 International Symposium on Electronics Materials and Packaging. (n.d.). doi:10.1109/emap.2005.1598275.

[36] V. Vishwakarma, C. Waghela, Z. Wei, R. Prasher, S.C. Nagpure, J. Li, et al., Heat transfer enhancement in a lithium-ion cell through improved material-level thermal transport, *Journal of Power Sources*. **300** (2015) 123–131. doi:10.1016/j.jpowsour.2015.09.028.

[37] D. Anthony, D. Wong, D. Wetz, A. Jain, Non-invasive measurement of internal temperature of a cylindrical Li-ion cell during high-rate discharge, *International Journal of Heat and Mass Transfer*. **111** (2017) 223–231. doi:10.1016/j.ijheatmasstransfer.2017.03.095.

Chapter 8

Conclusion

10-1. Conclusion

In chapter 2, theoretical modeling of transient and nonlinear heat transfer in a Cartesian fin-PCM based storage systems is presented. Governing equations for the temperature distribution are derived which account for sensible heat storage and temperature gradient in the melted region. These phenomena were not considered in past works. The results establish the existence of an optimal fin size that maximizes the benefit of the fin on heat transfer into the PCM. The optimal fin size resulting in maximum heat stored into the PCM, and the dependence of this optimal fin size on thermal properties may offer guidelines for the design of engineering phase change energy storage systems.

Chapter 3 presents s semi-analytical method to solve transient and non-linear heat transfer in cylindrical phase change storage systems for transverse and longitudinal fin configurations. Results show key similarities and differences cylindrical fins and Cartesian fins investigated in

chapter 2. Similar to Cartesian fins, it is shown that fin insertion increases thermal energy stored in the PCM significantly for both transverse and longitudinal fins for a given time. However, in contrast with Cartesian fins, the amount of heat stored is not a strong function of fin size. The insights that even a small-sized fin results in considerable benefit and that further increasing the fin size results in very little incremental benefit are both helpful for practical design of such systems.

Chapter 4 investigates the nature of convective heat transfer on a flat plate in response to a plate heat flux that varies in both space and time. The general solution for transient temperature distribution over the plate is developed based on integral method and use of fourth-order Karman-Pohlhausen polynomials. The results improve understanding of external laminar convective heat transfer which is applicable to several engineering problems.

Chapter 5 presents an analytical approach to determine convective heat transfer variation in the plate due to the plate temperature varying with both time and space. The generalized developed solution shows reasonable accuracy where the results are compared with previous works for special cases. It is expected that this approach may help in understanding the heat transfer in flat bed PCM storage systems.

Chapter 6 investigates a conjugate problem of heat transfer within the PCM and convective heat transfer in the fluid flow which improves understanding the nature of convective heat transfer in a flat bed PCM systems. This work accounts for transient space varying heat transfer coefficient at the at the plate which was not accounted in the past. Dependence of total heat stored in the system on thermal conductivity of the fluid and PCM is discussed. The results show that total heat stored is a much stronger function of thermal conductivity of the fluid rather than of the PCM. The results may offer guidelines for design optimization of such systems for engineering applications.

170

Chapter 7 shows experimental results of both cooling and heating of a Li-ion cell. The simple switch between cooling and heating modes by simply changing polarity of thermoelectric current makes thermoelectric element an effective approach to meet both cooling and heating requirements for a Li-ion cell. Despite the high power consumption and cost, thermoelectric elements may be suitable for thermal management of Li-ion cells in specific applications. The trade-off between thermal management and power consumption is likely to be application based and needs to be carefully considered and optimized.

BIOGRAPHICAL INFORMATION

Amirhossein Mostafavi received his M.S. and B.S. degrees in Mechanical Engineering from Iran University of Science and Technology and Ferdowsi University of Mashhad respectively. He started his Ph.D. in Mechanical Engineering in Spring 2016. His research area includes heat transfer, phase change, energy storage and Li-ion batteries. He worked as an Intern at Tesla, Inc. in Summer 2020. He plans to continue his research as a postdoctoral fellow in near future.

Email: mostafavi.amirhossein@gmail.com